ABSTRACT

Title of Dissertation:	EXPLORING REGIONAL EMISSIONS AND TROPOSPHERIC OZONE IN THE EASTERN UNITED STATES USING AIR QUALITY MODELS AND DATA PRODUCTS
	Allison Marie Ring, Doctor of Philosophy, 2019
Dissertation directed by:	Associate Research Professor, Timothy P. Canty, Department of Atmospheric & Oceanic Science

Tropospheric ozone (O_3) is a harmful pollutant regulated by the US Environmental Protection Agency (EPA) through the use of designated air quality standards. Within the United States, approximately 110 million people live within counties designated as in non-attainment of the O_3 standard. In this work, analysis is performed to examine the influence of anthropogenic emissions on tropospheric O_3 production within the framework of the CMAQ regulatory air quality model. Adjustments are recommended to improve emission representation from the largest (class 3) commercial marine vessels (c3 Marine). Model results with the implemented corrections show improved comparison to surface O_3 observations from AQS sites. Characterization of the photochemical O_3 production regime (VOC or NO_x sensitive)

is performed using the ratio of formaldehyde (HCHO) and nitrogen dioxide (NO_2) tropospheric column observations from the satellite borne Ozone Monitoring Instrument (OMI), and whole air sampling canisters in the Long Island Sound (LIS) collected on May 17th and 18th, 2017. Evidence for the importance of anthropogenic VOCs in the New York City pollution plume and their role in tropospheric O_3 production is presented. Aircraft O_3 observations are used to evaluate model performance of the National Oceanic Atmospheric Administration (NOAA) National Air Quality Forecast Capability system CMAQ model for the O_3 event in the LIS. Finally, a series of CMAQ simulations are performed to suggest the likely inventory sector (non-road mobile) most responsible for the significant O_3 production downwind of coastal urban centers like New York and Chicago. Important air quality policy implications of these findings are discussed.

EXPLORING THE IMPACT OF REGIONAL EMISSIONS SOURCES ON TROPOSPHERIC OZONE IN THE EASTERN UNITED STATES USING AIR QUALITY MODELS AND DATA PRODUCTS

by

Allison Marie Ring

Dissertation submitted to the Faculty of the Graduate School of the
University of Maryland, College Park, in partial fulfillment
of the requirements for the degree of
Doctor of Philosophy
2019

Advisory Committee:
Associate Research Professor Dr. Timothy P. Canty, Chair
Professor Dr. Russell R. Dickerson
Professor Dr. Ross J. Salawitch
Research Scientist Dr. Xinrong Ren
Associate Professor Dr. Amir Sapkota, Dean's Representative

Dedication

This thesis is dedicated to Gary and Carolyn Ring, my loving and supportive parents. All my life they stimulated my curiosity about the world, fostered my inquisitive mind, and provided me the tools to succeed. Without them, I would not have found the courage within myself to pursue this degree. I am forever grateful for their unyielding love and encouragement. I love you.

To my husband, Stefan Doboszczak, thank you. You have empathized with my struggles, provided valuable insight and supported me every step of the way. Without graduate school, I would never have met you, and without you, my life wouldn't be nearly as interesting. Thank you for coming into my life when I needed you most. I love you!

To the village of people who have helped me get here today, thank you. You all have kept me sane, happy, and proud to pursue my dreams. I am so fortunate to have such wonderful people in my life.

Acknowledgements

I would like to acknowledge all those who helped make this thesis possible. Research is a collaborative effort and without the assistance from MANY others, this work would not be possible.

First, I would like to thank Tim Canty. I am here because of you. Throughout my time in AOSC, you have been a friend, a teacher, a mentor, and a colleague. Thank you for always making time to help me with my questions, providing me with valuable connections, affording me the opportunity to pursue my research interests, and treating me as an equal. You believed in me when I didn't believe in myself and offered me the chance to work with you when I needed it most. You have helped shape my life and my future more than you will ever know. Thank you.

I would also like to thank Russ Dickerson and Ross Salawitch. You both have helped make AOSC feel like a family. Your guidance, suggestions, helpful criticism and valuable insights have made me, and all of us in AOSC, better scientists. Thank you for always having my best interest at heart, supporting my studies, and caring about my happiness and well-being. Graduate school is stressful, and you both have helped make it better by treating us as more than "cheap labor". Thank you.

I would like to thank all graduate students I have met at UMD. Without you, my 7+ years at the University of Maryland wouldn't have been the same. I will always have fond memories of my years in graduate school because of the lifelong friendships I have made and the support you all have given me. Thank you.

Finally, I would like to thank all those at the Maryland Department of the Environment who have given me the chance to prove my research abilities and contribute to the greater good. Working with you, I have felt useful, I have felt like my research mattered. Thank you for your support.

The research in this thesis was funded by the NASA ACMAP program. Thank you for your support.

Table of Contents

List of Tables

List of Figures

List of Abbreviations

AIS	Automated Identification System
$AM8O_3$	Average Maximum 8-hour Ozone
AMF	Air Mass Factor
AQS	Air Quality System
BEIS	Biogenic Emissions Inventory System
BW	Baltimore-Washington
c3 Marine	Class 3 Commercial Marine Vessel
CAA	Clean Air Act
CAMx	Comprehensive Air Quality Model with Extensions
CB05	Carbon Bond mechanism (2005)
CB6	Carbon Bond mechanism (version 6)
CCTM	CMAQ Chemical Transport Model
CEMS	Continuous Emission Monitoring System
CMAQ	Community Multiscale Air Quality model
CMV	Commercial Marine Vessel
CONUS	Continental United States
CRF	Cloud Radiance Fraction
CTM	Chemical Transport Model
DECSO	Daily Emissions estimates Constrained from Satellite Observations model
DISCOVER-AQ	Deriving Information on Surface Conditions from COlumn and VERtically resolved observations relevant to Air Quality
DOAS	Differential Optical Absorption Spectroscopy
DOMINO	Dutch Ozone Monitoring Instrument NO_2 retrieval
DV	Design Value
ECA	Emission Control Area
EEZ	Exclusive Economic Zone
EGU	Electrical Generating Unit
EPA	Environmental Protection Agency
ESA	European Space Agency
GEOS-Chem	Goddard Earth Observing System – Chemical transport model
GMI	Global Modeling Initiative
GSFC	Goddard Space Flight Center
HAP	Hazardous Air Pollutant
HRRR	High Resolution Rapid Refresh model
HYSPLIT	HYbrid Single-Particle Lagrangian Integrated Trajectory model
IMO	International Maritime Organization
IUPAC	International Union of Pure and Applied Chemistry
JJA	June, July, August
LIS	Long Island Sound, NY

MARAMA	Mid-Atlantic Regional Air Management Association
MARPOL	International Convention for the Prevention of Pollution from Ships
MCIP	Meteorology-Chemistry Interface Processor
MDA8	Maximum Daily Average 8-hour Ozone
MDE	Maryland Department of the Environment
MEGAN	Model of Emissions of Gases and Aerosols from Nature
MIR	Maximum Incremental Reactivity
MODIS	Moderate Resolution Imaging Spectroradiometer
NAAQS	National Ambient Air Quality Standards
NAM	North American Mesoscale model
NAQFC	National Air Quality Forecast Capability
NASA	National Aeronautics and Space Administration
NEI	National Emissions Inventory
NOAA	National Oceanic and Atmospheric Administration
NYC	New York City
PARANOX	PARAmetrization of emitted NOX model
PBL	Planetary Boundary Layer
PM	Particulate Matter
POCP	Photochemical Ozone Creation Potential
OAQPS	Office of Air Quality Planning and Standards
OTC	Ozone Transport Commission
RAMMPP	Regional Atmospheric Measurement Modeling and Prediction Program
RF	Research Flight
RRF	Relative Response Factor
SAO	Harvard-Smithsonian Astrophysical Observatory
SAPRC	Statewide Air Pollution Research Center
SCD	Slant Column Density
SCIAMACHY	Scanning Imaging Absorption spectrometer for Atmospheric CHartographY
SIP	State Implementation Plan
SPC	Storm Prediction Center
SLT	State, Local, Tribal agencies
SMOKE	Sparse Matrix Operator Kernel Emissions model
STS	Stratosphere-Troposphere Separation
TROPOMI	TROPospheric Ozone Monitoring Instrument
UN	United Nations
UV	Ultraviolet radiation
VCD	Vertical Column Density
VOC	Volatile Organic Compound
WRF	Weather Research Forecasting model

Chapter 1: Introduction

1.1: Ozone in the Troposphere

In the atmosphere, ozone (O_3) is required to create a habitable environment for life on Earth [*Finlayson-Pitts and Pitts*, 2000; *Seinfeld and Pandis*, 2006] and yet it is also responsible for causing health problems including premature death [*Bell et al.*, 2006; *Cohen et al.*, 2017; *Guarnieri and Balmes*, 2014; *Kampa and Castanas*, 2007]. Stratospheric O_3, known as "good ozone," acts as a shield by protecting life on Earth from harmful ultraviolet radiation, making the existence of life possible [*Finlayson-Pitts and Pitts*, 2000; *Seinfeld and Pandis*, 2006]. Tropospheric O_3, known as "bad ozone," is produced in the atmosphere from precursor species emitted as byproducts of anthropogenic and biogenic activity.

In the early 1950s, Arie Haagen-Smit from the California Institute of Technology discovered that the pollution plaguing Los Angeles, CA (LA) at the time, contained O_3 [*Jacobson*, 2002; *Seinfeld and Pandis*, 2006]. He exposed plants and other materials to O_3 in a series of chamber experiments and found they all experienced the same detrimental effects as when exposed to the LA pollution. Further experiments confirmed O_3 was produced from a combination of nitrogen oxides, reactive organic gases, and sunlight, commonly found in the summertime troposphere [*Haagen-Smit et al.*, 1953]. Based on his research, LA and other regions in the United States (US) began imposing air regulations on local businesses in an attempt to alleviate pollution episodes. By the mid-1960s, congress started passing air quality control legislation, however it lacked enforcement capability [*Jacobson*, 2002]. In 1970, Congress passed

the Clean Air Act (CAA) and established the Environmental Protection Agency (EPA) as the enforcing entity [*EPA*, 1970; 2017c; *Jacobson*, 2002; *OAQPS*, 2007]. Major revisions to the CAA were passed in 1977 and 1990. The amendments of 1977 focused primarily on regions that were not achieving national air quality objectives and provided further guidance for the prevention of significant deterioration of air quality [*EPA*, 2017c]. The amendments of 1990 were passed to provide expanded control of acid rain, urban air, and toxic air pollution [*EPA*, 2017c]. More discussion about environmental regulation in the United States (US) will follow in Section 1.1.2.

It is important to remember that air pollution is a global problem. Exposure to ambient concentrations of O_3 and particulate matter (PM) served as the leading source of global disease in 2015, disproportionally impacting underdeveloped countries [*Cohen et al.*, 2017; *Lelieveld et al.*, 2015]. Chronic exposure to O_3 causes impairment to lung function, eye irritation, and is linked to increased risk of mortality [*Bell et al.*, 2006; *Kampa and Castanas*, 2007; *Lippmann*, 1989]. As a secondary pollutant, O_3 is formed from precursors emitted into the atmosphere like carbon monoxide (CO), nitrogen oxides ($NO_x = NO + NO_2$), and volatile organic compounds (VOCs). The mechanisms describing O_3 production from these precursor species are detailed in Sections 1.1.1 and 1.1.2. Understanding the complex mechanisms and the emission sources of the precursors involved in producing tropospheric O_3 is vital to developing strategies to mitigate O_3 formation.

1.1.1: Ozone Production from CO and NO_x

Emissions of CO and NO_x are predominantly from combustion sources associated with anthropogenic activity and biomass burning [*EPA*, 2017b; e].

Emissions of CO result from the incomplete combustion of hydrocarbons from industrial processes, vehicle emissions, wood and fuel burning, and wildfires. Vehicle emissions alone can contribute up to 95% of the total CO measured in cities [*EPA*, 2017b]. Emissions of NO_x are from fossil fuel combustion, power generation, industrial sources, soil microbes, and lightning [*EPA*, 2017e].

Earth has an oxidizing atmosphere which means it is rich in oxygen (O_2), but the primary oxidant in the troposphere, and therefore the most important species for tropospheric chemistry, is the hydroxyl radical (OH) [*Levy*, 1971]. Formation of the OH radical begins with the reaction sequence below [*Seinfeld and Pandis*, 2006]:

$$O_3 + h\nu \rightarrow O_2 + O(^1D) \quad \text{(R1)}$$
$$O(^1D) + H_2O \rightarrow 2OH \quad \text{(R2)}$$

Photolysis of O_3 that leads to formation of the excited state oxygen atom $O(^1D)$ occurs at wavelengths $(\lambda) < 320$ nm (reaction R1). This $O(^1D)$ is critical for the formation of OH via reaction R2. Atmospheric concentrations of OH are sustained at $\sim 10^6$ molecules/cm^3, maintained via reaction with OH and other compounds [*Perner et al.*, 1987].

While some O_3 is transported from the stratosphere into the tropsophere, most is produced directly in the troposphere [*Fishman and Crutzen*, 1978; *Jacob*, 1999; *Seinfeld and Pandis*, 2006]. The mechanism for tropospheric O_3 production involving CO and NO_x is described below:

$$CO + OH \xrightarrow{O_2} CO_2 + HO_2 \quad \text{(R3)}$$
$$H + O_2 + M \rightarrow HO_2 + M \quad \text{(R4)}$$
$$\boldsymbol{HO_2 + NO \rightarrow OH + NO_2} \quad \textbf{(R5)}$$
$$NO_2 + h\nu \rightarrow NO + O \quad \text{(R6)}$$

$$O + O_2 + M \rightarrow O_3 + M \quad \text{(R7)}$$

Net: $CO + 2O_2 \rightarrow CO_2 + \boldsymbol{O_3}$

If NO reacts with O_3 rather than HO_2 (R10), the net reaction would consume tropsopheric O_3:

$$CO + OH \overset{O_2}{\rightarrow} CO_2 + HO_2 \quad \text{(R8)}$$
$$H + O_2 + M \rightarrow HO_2 + M \quad \text{(R9)}$$
$$\boldsymbol{O_3 + NO \rightarrow O_2 + NO_2} \quad \textbf{(R10)}$$
$$NO_2 + h\nu \rightarrow NO + O \quad \text{(R11)}$$
$$O + O_2 + M \rightarrow O_3 + M \quad \text{(R12)}$$
$$HO_2 + O_3 \rightarrow OH + 2O_2 \quad \text{(R13)}$$

Net: $CO + \boldsymbol{O_3} \rightarrow CO_2 + O_2$

Therefore, the process by which NO oxidizes is critical for tropospheric O_3 production. In this mechanism, the important rate-limiting reaction (R5) determines the production of tropsopheric O_3. It is represented as the equation below:

$$P_{O_3} = k[HO_2][NO] \quad (14)$$

Concerning reactions R6 and R11, NO_2 will photodissociate at $\lambda < 420$ nm; high energy radiation with some wavelengths just outside the ultraviolet (UV) range. *Dickerson et al.* [1997] used the Variable-grid Urban Airshed Model (UAM-V) model to show that the rate of NO_2 photolysis was amplified by the aerosol scattering of solar radiation; particularly impactful in the planetary boundary layer. This process accelerates the rate of tropospheric photochemical production of O_3 in polluted regions.

1.1.2: Ozone Production from VOCs and NO_x

Tropospheric O_3 is also produced through atmospheric reactions of Volatile Organic Compounds (VOCs). These organics oxidize with OH, beginning the reaction sequence that produces O_3. VOCs have biogenic sources (mainly trees) and anthropogenic sources such as industrial activity, paints and solvents, evaporative emissions from gasoline, and engine exhaust [*EPA*, 2017f]. Figure 1 shows the relative contribution of anthropogenic and biogenic VOC emissions in 2011 for the US (a), and the relative contribution of four source sectors to the total anthropogenic VOC emissions in 2011 (b).

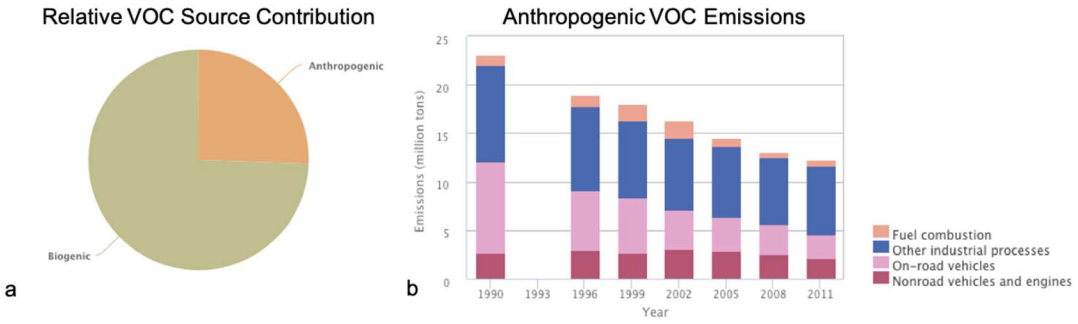

Figure 1: VOCs in the US: (a) relative source contribution from 2011 of anthropogenic and biogenic VOCs in the US (b) VOC emissions from four source sectors between 1990 and 2011. The on-road sector consists of cars, trucks, buses, and motorcycles. For this plot, the non-road sector consists of farming equipment, lawn equipment, ships, aircraft, etc. This figure is from *EPA* [2017f].

A representative mechanism for VOC oxidation is provided below. The example shown is for methane (CH_4) [*Jacob*, 1999]:

$$CH_4 + OH \rightarrow CH_3 + H_2O \quad \text{(R15)}$$

$$CH_3 + O_2 + M \rightarrow CH_3O_2 + M \quad \text{(R16)}$$

$$CH_3O_2 + NO \rightarrow CH_3O + NO_2 \quad \text{(R17)}$$

or $$CH_3O_2 + HO_2 \rightarrow CH_4O_2 + O_2 \quad \text{(R18)}$$

$$CH_3OOH + OH \rightarrow CH_2O + OH + H_2O \quad \text{(R19)}$$

or $$\rightarrow CH_3O_2 + H_2O \quad \text{(R20)}$$

$$CH_3OOH + h\nu \rightarrow CH_3O + OH \quad \text{(R21)}$$

$$CH_3O + O_2 \rightarrow CH_2O + HO_2 \quad \text{(R22)}$$

$$CH_2O + OH \rightarrow CHO + H_2O \quad \text{(R23)}$$

or

$$CH_2O + h\nu \xrightarrow{O_2} CHO + HO_2 \quad \text{(R24)}$$

$$\rightarrow CO + H_2 \quad \text{(R25)}$$

$$CHO + O_2 \rightarrow CO + H_2O \quad \text{(R26)}$$

Begin CO oxidation described in Section 1.1.1

Net: $$CH_4 + 10O_2 \rightarrow CO_2 + H_2O + \mathbf{5O_3} + 2OH \quad \text{(R27)}$$

Based on the meaningful net reaction (R27), in the presence of NO_x, five O_3 molecules are produced during the oxidation process of CH_4 to CO_2. Termination of these production mechanisms requires radical reaction to produce a nonradical:

$$HO_2 + HO_2 \rightarrow H_2O_2 + O_2 \quad \text{(R28)}$$

$$OH + NO_2 + M \rightarrow HNO_3 + M \quad \text{(R29)}$$

In relatively clean environments, or regions with low NO_x concentrations, radical termination occurs through R28. In regions of high NO_x, radical termination occurs through R29.

1.1.3: The NO_x-O_3-VOC Relationship

Tropospheric O_3 production relies upon the non-linear relationship between NO_x and VOCs [*Jacob*, 1999; *Jacobson*, 2002; *Lippmann*, 1989; *Sillman*, 1990]. Effective emission control strategies are developed according to the local photochemical O_3 production regime: either NO_x-sensitive or VOC-sensitive. The NO_x-sensitive regime refers to atmospheric conditions where concentrations of NO_x are relatively low compared to VOCs. In this regime, a reduction of NO_x leads to a reduction of O_3. The VOC-sensitive regime describes atmospheric conditions where

concentrations of VOCs are relatively low compared to NO_x. In this regime, a reduction of NO_x leads to an *increase* of O_3.

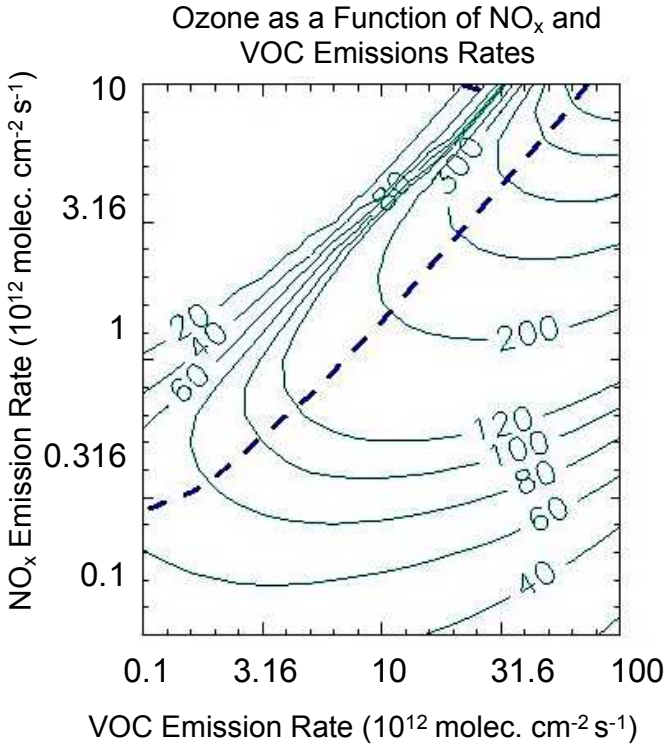

Figure 2: Isopleths of O_3 (ppb) as a function of NO_x and VOC emissions simulated by a photochemical box model. The blue dotted line represents NO_x and VOC emission rates that correspond to a ridge of peak O_3 production. NO_x-sensitive conditions are represented below the ridge line, VOC-sensitive conditions are represented above. (Figure from http://www-personal.umich.edu/~sillman/ozone.htm#OZO1.2)

Figure 2 shows isopleths of O_3 calculated by a photochemical box model as a function of VOC and NO_x emission rates. The blue dotted line represents the ridge of maximum O_3 production. Regions below the ridge line are considered NO_x-sensitive. Regions above the ridge line are considered VOC-sensitive. In this regime, reductions in NO_x alone could have the *local* adverse effect of increasing O_3. It is never advisable to increase NO_x emissions, therefore controlling VOCs and NO_x emissions together are necessary to achieve the desired O_3 reduction.

Development of effective air quality policy depends heavily on the regulated region's [VOC]/[NO_x] ratio. Creation of controls targeting the appropriate pollutants (NO_x and/or VOC) is necessary to effectively reduce surface O_3. Determination of the photochemical production regime, however, can be challenging. A variety of factors including meteorology, biogenic emissions, temporal and spatial variation of local anthropogenic activity, and transported pollution from upwind sources all contribute to the [VOC]/[NO_x] ratio, and therefore the instantaneous rate of O_3 production for a given region. In an effort to develop effective air quality strategies, state agencies often rely on air quality modeling simulations. Therefore, considerable effort is made to create model frameworks that represent the actual atmosphere.

1.2: Air Quality Regulation and Health

Consequential amendments to the original CAA passed in 1970 were passed in 1977 and 1990, which gave the EPA more authority to enforce air pollution regulation [*EPA*, 1970; 1990; 2017c; *OAQPS*, 2007]. Passage of the CAA established the National Ambient Air Quality Standards (NAAQS), which sets atmospheric abundance limits for six criteria pollutants [*EPA*, 1970; 1990; 2015c; 2017c; 2018d]. Current standards are described in Table 1.

The criteria pollutants were chosen based on their known health risks and environmental degradation capability [*EPA*, 1990; 2018d]. Each pollutant has a primary and secondary standard. The primary standard is set to protect the US population from health risks, especially for sensitive populations like the elderly, children, and asthmatics. The secondary standard is set to protect the environment

(ecosystems, crops, visibility, climate, etc.) from adverse effects of the pollutant [*EPA*, 1990; 2018d].

Table 1: Current NAAQS standards for criteria pollutants [*EPA*, 2016b]

Pollutant	Primary or Secondary Designation	Time Frame	Standard	Meeting the Standard
Particulate Matter $PM_{2.5}$	Primary	1 year	12 $\mu g/m^3$	Annual mean (3-year average)
	Secondary	1 year	15 $\mu g/m^3$	Annual mean (3-year average)
	Primary and Secondary	1 day	35 $\mu g/m^3$	98th percentile (3-year average)
Particulate Matter PM_{10}	Primary and Secondary	1 day	150 $\mu g/m^3$	No more than 1 exceedance/year on average for 3 years
Ozone (O_3)	Primary and Secondary	8 hours	70 ppb	Annual 4th-highest max. daily avg. 8-hr O_3 (MDA8) averaged for 3 years
Sulfur Dioxide (SO_2)	Primary	1 hour	75 ppb	99th percentile of daily 1-hour max. conc. average for 3 years
	Secondary	3 hours	0.5 ppm	No more than 1 exceedance/year
Nitrogen Dioxide (NO_2)	Primary	1 hour	100 ppb	99th percentile of daily 1-hour max. conc. average for 3 years
	Secondary	1 year	53 ppb	Annual mean
Carbon Monoxide (CO)	Primary	8 hours 1 hour	9 ppm 35 ppm	No more than 1 exceedance/year
Lead (Pb)	Primary and Secondary	running 3-month average	0.15 $\mu g/m^3$	No exceedances

Air quality has improved since inception of the CAA in 1970, with significant advancements since establishment of the NAAQS in 1990 [*EPA*, 2018b; *He et al.*, 2013b; *Lamsal et al.*, 2015; *Tong et al.*, 2015]. Northeast regional (from Maryland to Maine) average concentrations of the six criteria pollutants have declined over the past two decades (Figure 3), such that all are now below the national standard, except for O_3 (as of 2017) [*EPA*, 2018b]. In the Northeast, tropospheric O_3 is produced in the atmosphere from local emissions of VOCs as well as NO_x, and O_3 is also transported into the region from upwind out-of-state sources due to the prevailing westerly winds

[*Endlich et al.*, 1984; *He et al.*, 2016a; *Loughner et al.*, 2011; *Moghani et al.*, 2018; *Ryan et al.*, 1998; *Sillman et al.*, 1993; *Wolff et al.*, 1977].

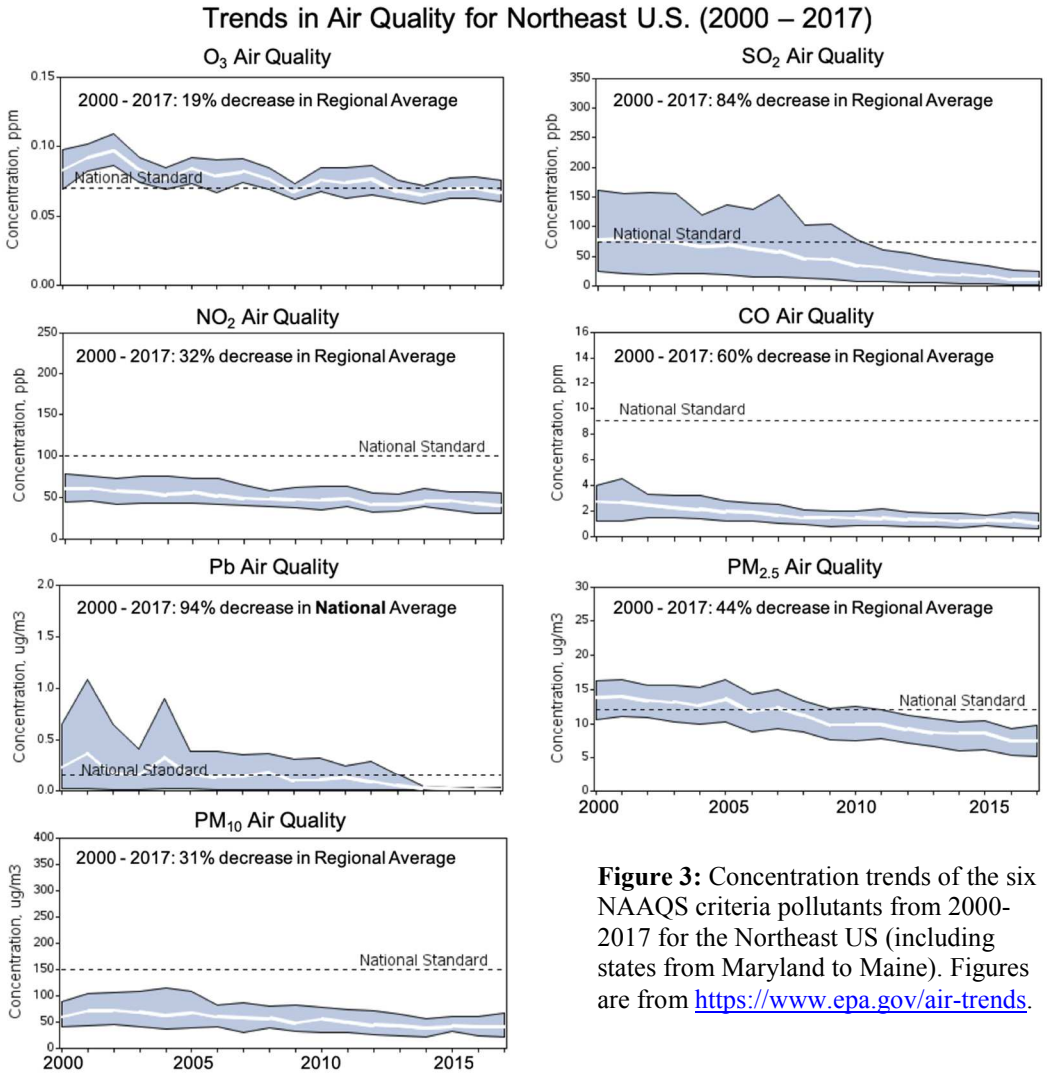

Figure 3: Concentration trends of the six NAAQS criteria pollutants from 2000-2017 for the Northeast US (including states from Maryland to Maine). Figures are from https://www.epa.gov/air-trends.

Emissions from large populations coupled with typical synoptic meteorology contribute to the continued challenges in meeting the O_3 NAAQS faced by the Northeast US. Figure 4a shows the national map of 8-hour O_3 non-attainment areas and Figure 4b shows the population living within these non-attainment areas (as of 2017). With about one third of the total US population subjected to unhealthy levels of

pollution, emission control of the criteria pollutants and specifically O_3 precursors are essential to improving air quality. As shown in Figure 4, 8-hour O_3 non-attainment areas are mostly concentrated in or downwind of heavily populated urban areas. In other words, people living in urban centers are subjected to poor air quality and related health problems, more than those in rural areas. Studies have shown that incidences of hospital visits coincide with poor air quality episodes [*Bell et al.*, 2007; *Fann et al.*, 2018; *Fauroux et al.*, 2000]. Symptoms of impaired health related to air quality include episodic respiratory distress, aggravation of conditions like asthma, heart complications, and in some cases death [*Bell et al.*, 2007; *Fann et al.*, 2018; *Fann et al.*, 2015; *Fauroux et al.*, 2000; *Pope and Dockery*, 2006; *Schnell and Prather*, 2017; *Thompson et al.*, 2014; *Watts et al.*, 2015]. Additionally, particulate matter ($PM_{2.5}$) can move into the blood once inhaled into the lungs, causing problems throughout the body [*Fann et al.*, 2018; *Pope and Dockery*, 2006; *Watts et al.*, 2015].

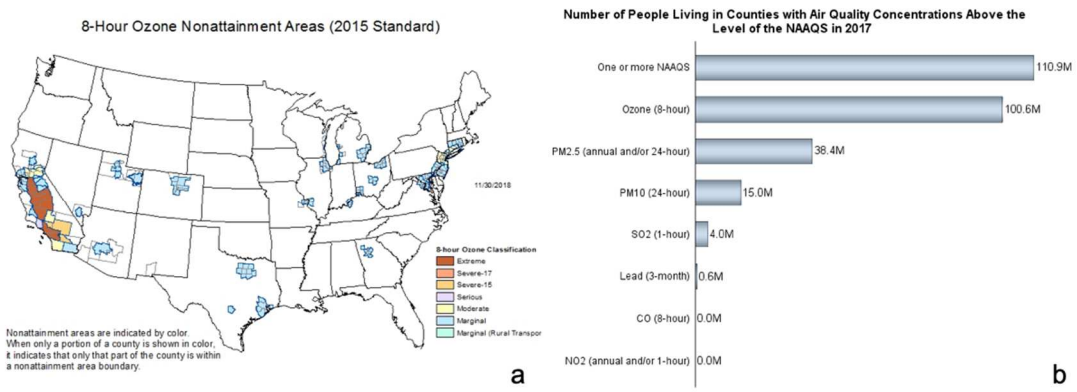

Figure 4: EPA designated (a) non-attainment areas for the 2015 8-hour O_3 standard and (b) the number of people living in counties with concentrations of pollutants above the NAAQS standard, designated as non-attainment. Image (a) is from https://www.epa.gov/air-trends/air-quality-national-summary. Image (b) is from https://www.epa.gov/air-trends/air-quality-national-summary.

In a warming climate, air quality related health issues are expected to rise [*Bell et al.*, 2007; *Fann et al.*, 2015; *Watts et al.*, 2015]. A study by *Bell et al.* [2007] found

the average number of days per summer that will exceed the 8-hour O_3 standard (75 ppb at the time of this study) will increase 68% when using the Intergovernmental Panel on Climate Change (IPCC) A2 climate scenario. This scenario holds anthropogenic emissions constant while allowing fluctuation for the temperature induced changes to chemical reaction rates and biogenic emissions [*Bell et al.*, 2007]. In summary, in order to mitigate health issues for the growing human population, pollution regulations to limit poor air quality episodes will continue to be necessary.

1.3: Overview of Regulatory Air Quality Modeling

As required by the CAA, state and local governments must develop strategies to ensure air quality monitoring sites within the State meet the various standards [*EPA*, 1990; 2015c; 2018d; *OAQPS*, 2007]. These State Implementation Plans (SIPs) outline proposed emission reduction strategies to meet the federal regulations. States with areas that do not meet the air quality standards (non-attainment areas) must submit specific SIPs for each area designated as non-attainment to the EPA for approval [*EPA*, 2017a]. The SIP should include the control strategies to be implemented and the costs and benefits of enforcing the control measures to attain the national standard. It should also explain all monitoring procedures, methods for addressing any violations, and designate the enforcing agency for the proposed control measures [*EPA*, 1990; 2018d]. States must submit detailed summaries including:

1. the methods used to determine necessary emissions reductions;
2. all tools used to analyze the proposed controls including data, emissions and air quality models;

3. the expected attainment results to demonstrate adequacy of the proposed SIPs [*EPA*, 1990; 2018d].

1.3.1: Modeling in the Mid-Atlantic Region

Maryland is a member of the Ozone Transport Commission (OTC), a multi-state organization that assists in the development and implementation of strategies to improve air quality with respect to surface O_3 (https://otcair.org/about.asp). The OTC includes states from Virginia to Maine, encouraging collaborative efforts from all the member state environmental departments to resolve issues related to surface O_3.

For the modeling centers in the Eastern US, a baseline model platform for the year 2011 was developed by the EPA to assist states with the creation of SIP quality attainment strategies [*EPA*, 2014; 2015a]. Creation of a model platform requires generation of anthropogenic and biogenic emissions, model domain initial and boundary conditions, and meteorology representative of the base year. The EPA released the first version of the 2011 model platform in early 2014 called "CAP_BAFM 2011-Based Platform, version 6" (2011v6) [*EPA*, 2014]. This platform models Criteria Air pollutants and Precursors (CAPs) and Benzene, Acetaldehyde, Formaldehyde (HCHO), and Methanol (BAFM). Known hazardous air pollutants for the model year 2011 version 6 are improved from the previous base year of 2007 or "version 5" [*EPA*, 2014]. The 2011v6 platform includes three improvements that warranted new version numbers. The most recent release in 2016 is called 2011v6.3 [*EPA*, 2016c], however most modeling performed in the following analyses uses the 2011v6.2 model platform [*EPA*, 2016c].

To create the model-ready emissions, the EPA used the Sparse Matrix Operator Kernel Emissions (SMOKE) Modeling System [*CMAS*, 2014b]. The primary use of SMOKE is to create gridded, speciated, hourly emissions files to be used in air quality modeling. National Emissions Inventories (NEIs) are developed every 3 years and consist of total emissions estimates gathered from the EPA and State, Local, and Tribal (SLT) agencies for a wide variety of chemical species for the CONtinental US (CONUS) [*EPA*, 2015a]. SMOKE temporalizes and assigns source locations (and heights) for the emissions based on the surrogate location files provided by the EPA (gridded at 12km) [*EPA*, 2014; 2015a; d]. A schematic describing the major components of the SMOKE model is shown in Figure 5.

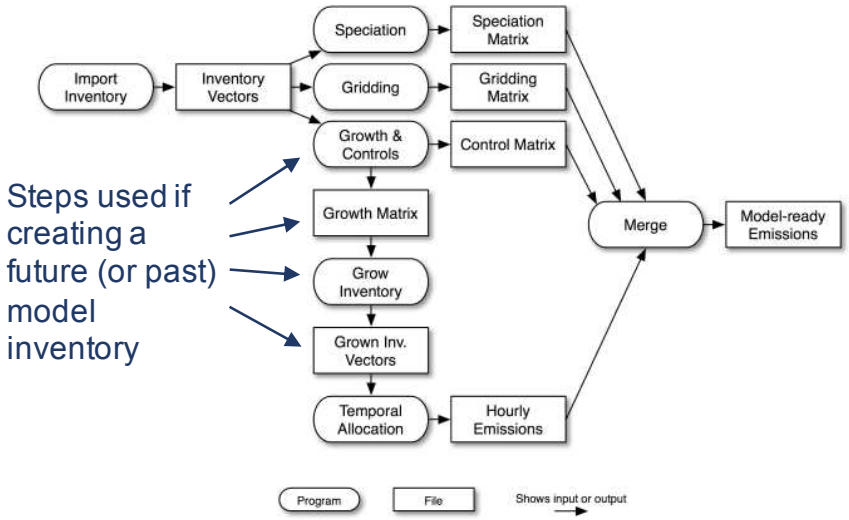

Figure 5: Major components of the SMOKE model. (Figure 2.4 from [*CMAS*, 2014b])

SMOKE uses a parallel approach (Figure 5) to emissions processing improving the computational efficiency of producing model-ready emissions [*CMAS*, 2014b]. Highlighted below are the major SMOKE steps to producing the model-ready emissions used for the 2011 base case modeling described in Chapters 3 and 4 [*CMAS*, 2014b]:

1. Import the NEIv2 files
2. Speciate the inventory into appropriate species for the air quality model chemical mechanism
3. Apply emissions controls (if necessary)
4. Temporally distribute emissions (including meteorology)
5. Spatially distribute emissions
6. Merge emissions into sector files with common characteristics (model-ready)

Applying the general steps outlined above, SMOKE is also used to drive the Biogenic Emissions Inventory System version 3.61 (BEISv3.61) model which produces biogenic emissions used in this air quality modeling [*CMAS*, 2014b]. This version of BEIS incorporates improved land use inputs from Moderate Resolution Imaging Spectroradiometer (MODIS) and the 2006 National Land Cover Database. Improved vegetation speciation inputs from the US Forest Service Forest Inventory Analysis and the US Dept. of Agriculture Biogenic Emissions Land-use Database version 4 (BELD4) are also used [*Bash et al.*, 2016]. BEIS produces emissions estimates for 33 species, but is re-speciated to 18 for compatibility with the air quality chemical mechanism used in regulatory modeling (described in Section 1.5.1) [*Bash et al.*, 2016].

Boundary conditions for the model domain were generated from the Goddard Earth Observing System (GEOS) Chemical (GEOS-Chem) transport model for the year 2011 [*EPA*, 2014]. Gridded meteorology for 2011 was generated from the Weather Research and Forecasting (WRF) model version 3.4 [*Skamarock et al.*, 2008] using high resolution sea surface temperature data from the Group for High Resolution Sea Surface Temperature (https://www.ghrsst.org/) [*EPA*, 2014]. To produce model-ready meteorology inputs, WRF output is processed through the Meteorology-Chemistry Interface Processor version 4.3 (MCIPv4.3) to convert the WRF coordinates into

CMAQ compatible horizontal and vertical coordinates [*CMAS*, 2015; *Otte and Pleim*, 2010]. This processing is a critical step to ensure mass consistency within CMAQ [*Otte and Pleim*, 2010].

The modeling platform for the base year 2011 described above, and used for the model analysis throughout this thesis, is used by all modeling centers in the OTC to preserve modeling result consistency. Until recently, attainment strategies for the various states within the OTC have been developed based on this modeling platform. Faculty in the Department of Atmospheric and Oceanic Science at the University of Maryland are intimately involved with the air quality modeling performed for the State of Maryland. The work in this thesis has contributed to those efforts.

1.4: Overview of Data Products

1.4.1: Air Quality System (AQS)

The Air Quality System (AQS) is an EPA and Office of Air Quality Planning and Standards (OAQPS) network of more than 4,000 surface monitoring stations throughout the US that measure ambient air pollution. The principal goal of the network is to examine the exposure of the US population to a variety of pollutants. AQS data are available from 1980 to the present for approximately 500 species, must pass several quality control checks before distribution, and are publicly available at https://www.epa.gov/outdoor-air-quality-data [*EPA*, 2016a]. These data are used in the Commercial Marine Vessel analysis discussed in Chapter 3.

1.4.2: Ozone Monitoring Instrument (OMI)

The Ozone Monitoring Instrument (OMI) is a space-borne instrument supported by three countries. The instrument was developed by a team of scientists from the Netherlands and Finland and is deployed aboard the National Aeronautics and Space Administration (NASA) Aura satellite (launched July 15, 2004), which orbits with a suite of other satellites in the NASA A-train. Aura has a polar, sun synchronous orbit providing daily global coverage with an overpass time of approximately 13:30 local solar time (LST) at the equator [*Levelt et al.*, 2006a; *Levelt et al.*, 2006b]. The OMI instrument measures solar radiation backscattered from the atmosphere and Earth's surface within the UV/Visible wavelength range of 270-500 nm, with a spatial resolution of 13 × 24 km^2 at nadir and total swath coverage of 2600 km. The OMI science team retrieves column O_3, NO_2, and SO_2, three of the six criteria pollutants named by the EPA, as well as column BrO, OClO, and HCHO [*Levelt et al.*, 2006a; *Levelt et al.*, 2006b].

A detector row anomaly appeared in the data on June 25, 2007 and impacted approximately 50% of OMI pixels in 2011, significantly reducing data density [*Bucsela et al.*, 2013]. All pixels affected by the row anomaly in the OMI products described below are filtered out for this analysis [*Boersma et al.*, 2011; *Bucsela et al.*, 2013]. We use a total of two OMI data products: daily tropospheric column NO_2 and column HCHO and three retrieval methods (two for NO_2 and one for HCHO).

For the analysis in Chapter 2, we use the Dutch Ozone Monitoring Instrument NO_2 (DOMINO) near real-time tropospheric column NO_2 retrieval [*Boersma et al.*, 2007]. As OMI passes overhead, the instrument detects a slant column of the

atmosphere using a Differential Optical Absorption Spectroscopy (DOAS) approach [*Boersma et al.*, 2004; *Boersma et al.*, 2007; *Bucsela et al.*, 2006]. Stratospheric NO_2 is estimated by a stratospheric Chemical Transport Model (CTM) called TM4 and then removed from the total slant column to produce a residual tropospheric NO_2 slant column [*Boersma et al.*, 2007]. The tropospheric slant column is converted to a vertical column using an Air Mass Factor (AMF) calculated by the TM4 global tropospheric CTM. This model simulates the expected profile of NO_2 in the troposphere, producing the necessary AMFs for the algorithm [*Boersma et al.*, 2007; *Eskes and Boersma*, 2003]. Data from the DOMINO retrieval, along with data for other species and satellites, can be found at http://www.temis.nl/airpollution/no2.html.

For the analysis in Chapter 3 we use the NASA Goddard Space Flight Center (GSFC) version 3 level 2 tropospheric NO_2 column product [*Bucsela et al.*, 2013; *Krotkov et al.*, 2017; *Krotkov and Veefkind*, 2016] gridded to 0.25° latitude × 0.25° longitude resolution. The GSFC retrieval uses the Stratosphere-Troposphere Separation (STS) algorithm to calculate the tropospheric column NO_2 by removing the stratosphere component [*Bucsela et al.*, 2013]. This method assumes that over much of the world, the vast majority of detected NO_2 is in the stratosphere. Therefore, the stratospheric Vertical Column Density (VCD) from these clean or cloud obscured pixels is used to interpolate the stratospheric component of neighboring polluted or cloud free pixels [*Bucsela et al.*, 2013]. To calculate the stratospheric and tropospheric AMFs, monthly NO_2 profile climatology are derived from Global Modeling Initiative (GMI) CTM [*Strahan et al.*, 2007] simulations for 2005-2007 [*Bucsela et al.*, 2013]. For the clean pixels, an initial total VCD is calculated by dividing the total Slant

Column Density (SCD) by the stratospheric AMF. A small model estimated tropospheric NO_2 column representing the tropospheric component of the VCD for the clean region is subtracted from the total VCD. Pixels are masked for highly polluted areas where the modeled tropospheric component is larger than the stratospheric VCD [*Bucsela et al.*, 2013]. Masked pixels are removed from the initial stratospheric VCD calculation. The stratospheric component over polluted tropospheric regions is interpolated from its neighboring clean (or cloudy) pixels. Smoothing of any "hot spots" in the stratospheric VCD are done by replacing the values with the mean if the "hot spot" exceeds the mean by more than 1.5 standard deviations [*Bucsela et al.*, 2013]. Finally, the stratospheric component is removed from the total column SCD. The remaining tropospheric SCD is divided by the tropospheric AMF to yield the tropospheric VCD. This STS method is a very different approach to calculating the stratosphere NO_2 contribution than the DOMINO retrieval described earlier, yet the two retrievals produce similar results [*Bucsela et al.*, 2013].

We also use the HCHO version 3 level 2 reference sector corrected swath product from the Harvard-Smithsonian Astrophysical Observatory (SAO) retrieval [*González Abad et al.*, 2015] on a 0.25° latitude × 0.25° longitude grid. For both the GSFC OMI products (i.e., NO_2 retrieval and the SAO HCHO retrieval,), we only use pixels that satisfy quality and row anomaly flags, have a cloud fraction less than 30%, and a solar zenith angle less than 70°. Additionally, data from the two outer-most pixels are removed due to their large footprint (28 × 150 km^2) compared to the nadir view. The GSFC NO_2 and SAO HCHO retrievals are publicly available at http://mirador.gsfc.nasa.gov. Since HCHO concentrations in the stratosphere are

negligible [*Millet et al.*, 2006], the HCHO retrieval does not incorporate a stratosphere-troposphere separation algorithm. Instead, *a priori* HCHO profiles are generated using GEOS-Chem simulations. These vertical profiles are used to develop the air mass factor (AMF) calculations at various latitudes. This profile extends up to 100hPa where the concentrations of HCHO have dropped to near 0 ppb [*González Abad et al.*, 2015].

1.4.3: RAMMPP – Long Island Sound 2017

For the past two decades the University of Maryland has conducted a multi-faceted effort to understand air quality in the Eastern US called the Regional Atmospheric Measurement Modeling and Prediction Program (RAMMPP) (http://www.atmos.umd.edu/~rammpp). RAMMPP consists of four major components: ozone forecasting, *in situ* measurements, mesoscale modeling, and chemical transport modeling. Valuable *in situ* measurements have been collected each year (except 2006) during the O_3 season (April – October) since 1997 providing information about long-term trends in the Mid-Atlantic and Eastern U.S. [*He et al.*, 2013b; *Taubman et al.*, 2004]. For the work in this thesis, a small portion of the RAMMPP data are used to analyze VOCs in the Long Island Sound (LIS) region of New York on May 17 and 18, 2017. These data were collected during a total of three research flights.

Trace gas and aerosol measurements were collected aboard the University of Maryland's Cessna 402B research aircraft. A detailed description of the aircraft instrumentation can be found in *Ren et al.* [2018]. During this campaign, O_3 was measured with a modified UV absorption Thermal Electron Model 49C analyzer; NO_2 was measured with a Los Gatos Research Model RMT-200 Cavity Enhanced Absorption Spectroscopy (CEAS) analyzer; SO_2 was measured with a modified pulsed

fluorescence Thermal Electron Model 43C analyzer; CO, CH_4, CO_2, and H_2O were measured with a Picarro Cavity Ring-Down Spectrometer (CRDS) Model G2401-m [*Ren et al.*, 2018]. Additional aerosol optical properties were measured, and grab cans were used to sample atmospheric air at various intervals throughout the research flights. All VOCs were analyzed by the Maine Department of Environmental Protection using a Gas Chromatography – Mass Spectrometer (GC-MS) [*Ren et al.*, 2018]. A map of the three research flights is shown in Figure 6. Research Flight (RF) 1 was from 14:50 to 18:10 LST on May 17, RF2 was from 7:40 to 10:25 LST on May 18, and RF3 was from 13:10 to 16:40 LST on May 18, 2017.

A total of 35 canisters sampling ambient air were collected, and 50 VOC species were reported during the RAMMPP LIS 2017 field campaign. The list of species can be found in Appendix A. These data are used in the VOC analysis over Long Island Sound discussed in Chapter 4.

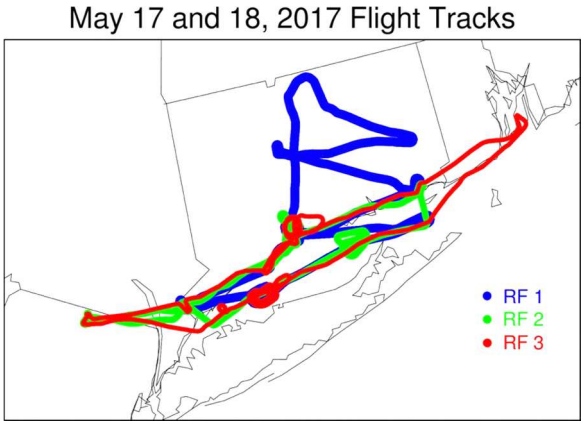

Figure 6: Flight tracks for the 3 research flights over the Long Island Sound during May 17th and 18th, 2017. RF1 (blue) was in the afternoon on May 17th, RF2 (green) was in the morning on May 18th, and RF3 (red) was in the afternoon on May 18th.

1.5: Modeling and Emissions Inventories

1.5.1: CMAQ version 5.0.2 – UMD

For the analysis in Chapters 3 and 4 we use the EPA Community Multiscale Air Quality (CMAQ) model version 5.0.2 [*Byun and Schere*, 2006; *CMAS*, 2014a]. CMAQ is a 3-dimensional Eulerian chemical transport model simulating chemical processes in the troposphere [*EPA*, 2017d]. Mathematical calculations describing transport across grid cells and the chemical reactions that occur within them are based upon conservation of mass for the given time step [*EPA*, 2017d]. A basic schematic of the various components of CMAQ is described in Figure 7. Generation of the required inputs to the CMAQ Chemical Transport Model (CCTM) was detailed previously in Section 1.3.1.

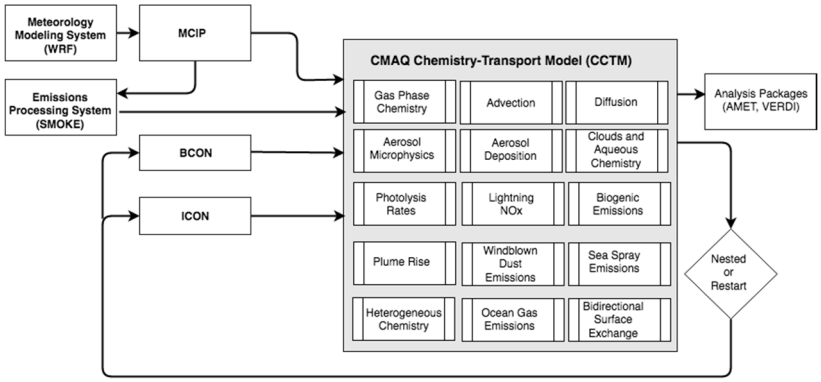

Figure 7: The CMAQ modeling system detailing the necessary emission and the various modules of the CMAQ Chemistry-Transport Model (CCTM). (Figure 4-6 from *EPA* [2017d])

The core 2005 Carbon Bond (CB05) chemical mechanism consists of 156 gas-phase reactions with 51 species representing the photochemistry of the troposphere [*Yarwood et al.*, 2005]. The CMAQ platform used in this analysis incorporates a modified version of CB05 consisting of 172 gas phase reactions and ~70 species called

CB05cltx_AE5_aq. This chemical mechanism includes the CB05 extended toxics reactions, updates to all rate reactions as of 2008, and the addition chlorine reactions for certain VOCs. All reactions and species for chemical mechanism used in this CMAQ model platform are detailed in Appendix B. It is important to note that this is the regulatory-approved CMAQ platform used by state and local agencies to develop attainment strategies. The modifications to the base CB05 mechanism were made by the developers and approved by the regulatory agencies.

CB05 is a simplified chemical mechanism designed to model the oxidative chemistry of the atmosphere for important pollutants like O_3, NO_x and particulate matter [*Yarwood et al.*, 2005]. The Carbon Bond chemical mechanisms are representative of the numerous reactions that occur in the atmosphere yet simple enough to be computationally feasible for use in air quality models [*Yarwood et al.*, 2005]. A much more expansive mechanism called the Master Chemical Mechanism is available (http://mcm.leeds.ac.uk/MCM/) but is best used in 0-dimensional box modeling analyses.

An updated version of CB05 called the Carbon Bond Mechanism version 6 (CB6) was released in 2010 [*Yarwood et al.*, 2010]. This mechanism consists of 218 gas-phase reactions with 77 species [*Yarwood et al.*, 2010]. The additional reactions and species improve secondary organic aerosol and oxidant formation from long-lived VOC species in the model [*Yarwood et al.*, 2010]. Further improvements were released in 2013 as the Carbon Bond version 6 revision 2 (CB6r2) mechanism [*Hildebrandt Ruiz and Yarwood*, 2013; *Yarwood et al.*, 2014]. This mechanism has 80 distinct species, the same gas-phase reactions as CB6, all reactions are updated to incorporate

the 2013 International Union of Pure and Applied Chemistry (IUPAC) reaction rates, and partitioned organic nitrates more appropriately which improved O_3 simulations [*Hildebrandt Ruiz and Yarwood*, 2013; *Yarwood et al.*, 2014]. In 2014 an optional halogen mechanism suite consisting of 88 reactions and 41 species called CB6r2h was released [*Yarwood et al.*, 2014]. Halogens such as iodine, chlorine, and bromine are important to tropospheric O_3, especially in coastal regions influenced by sea-salt. Under some conditions, halogens produce tropospheric O_3; under others, they destroy it [*Chang et al.*, 2002]. This detailed mechanism aims to represent this important halogen chemistry, however it is computationally expensive and therefore remains an optional addition to CB6r2 [*Yarwood et al.*, 2014]. A mechanism update to improve representation of wintertime O_3 formation due to snow cover was released in 2015 (CB6r3) [*Emery et al.*, 2015]. A new version called CB6r4 was released in 2016, incorporating the wintertime O_3 improvements from CB6r3 and the 16 most important halogen reactions for O_3 from CB6r2h [*Emery et al.*, 2016]. These reactions are from the iodine mechanism in CB6r2h and are the most important for ozone depletion by iodine [*Emery et al.*, 2016]. Improvements to reaction product yields and IUPAC reaction rates were also performed for the CB6r4 update [*Emery et al.*, 2016].

These updated chemical mechanisms were not incorporated into the modeling performed in this thesis; however, discussion of their benefits is given in Section 5.3 and references the relationship between halogens and tropospheric O_3. A new version of CMAQ (v5.2) was released in 2017 and is capable of implementing the CB6r3 mechanism (https://www.cmascenter.org/) [*EPA*, 2017d]. At the time of analysis, CMAQv5.0.2 was the only appropriate model platform available.

1.5.2: CMAQ version 5.0.2 – ARL

For the analysis in Chapter 4, the National Oceanic and Atmospheric Administration (NOAA) National Air Quality Forecast Capability (NAQFC) system was used to forecast an air quality O_3 event in the Long Island Sound, NY (LIS) region [*Lee et al.*, 2017; *Tong et al.*, 2015; *Tong et al.*, 2016]. The NAQFC system includes three major components: chemistry, meteorology, and emissions. The NAQFC uses the CMAQv5.0.2 and CB05 to predict O_3, $PM_{2.5}$, and their precursors concentrations over the CONtiguous US (CONUS) states, northern Mexico and southern Canada. Hourly meteorological data from the NOAA National Center for Environmental Prediction's North American Mesoscale (NAM) forecast model are used in the CMAQ simulations. The NAM relies on the meteorology dynamic core of WRF-NMM (Non-hydrostatic Mesoscale Model) on the B grid (WRF-NMMB) with upgraded tracer advection scheme [*Janjic*, 2003]. Boundary conditions used in the simulation are monthly averaged profiles extracted from the 2006 simulation with Harvard University's GEOS-Chem model [*Zhang et al.*, 2011]. The NAQFC emission dataset includes gaseous and particulate emissions from anthropogenic sources (area, mobile, and point) and natural sources (biogenic, soil, and sea salt). For sources outside the US, the Mexico NEI from 2012 and the Environment Canada and Climate Change Emission Inventory from 2010 are used to represent emissions Mexico and Canada. Inside the US, area and mobile sources are generated from a mixture of the EPA 2011 NEI and projected 2012 NEI using the Cross-State Air Pollution Rule (CSAPR) projection data [*Pan et al.*, 2014]. Point sources, including both Electrical Generating Units (EGUs) and non-EGUs, are generated using the 2011 NEI as baseline, with the EGU sources

further updated to 2016 with the Continuous Emission Monitoring System (CEMS) data. The performance of this modeling system to predict O_3 and $PM_{2.5}$, and their key precursors has been extensively evaluated with ground and field campaign data [*Lee et al.*, 2017; *Tong et al.*, 2016].

1.5.3: Alpha2 Emissions Inventory

As mentioned in Section 1.3, modeling is essential for developing and testing strategies to improve compliance with air quality regulation. Reliable emissions are required to effectively model various attainment strategies. For modeling efforts in the OTC, the Mid-Atlantic Regional Air Management Association (MARAMA) develops emissions based on the EPA NEIs [*EPA*, 2015a; *McDill et al.*, 2015]. For the analysis in Chapter 3, we use the MARAMA Alpha2 version of emissions, released in November 2015 and based primarily on the 2011 NEI version 2 (2011 NEIv2). The non-road inventory is the only emissions sector to use input from the 2011 NEI version 1 data [*McDill et al.*, 2015]. Emissions inventories are also projected to future years to aid in the development of effective air quality policy (SIPs). In the Alpha2 inventory, emissions for all sectors (excluding biogenic emissions) are projected from the base year (2011) to the future year (2018). For most sectors, emissions inventories for model year 2018 are generated by applying growth factors based on input from State, Local, and Tribal (SLT) agencies to the 2011 base case emissions. Projected emissions for the non-road and on-road mobile sectors are created using input from version 1 of the 2018 EPA's National Emissions Inventory [*McDill et al.*, 2015]. The Alpha2 inventory also projects emissions to 2028 using growth factors, however these emissions were not used in the analysis in Chapter 3.

All emissions are categorized into seven major source sectors [*McDill et al.*, 2015]:

1. **Point sources**: emission sources that have a specific latitude and longitude location, emitting at a single source, like a smoke stack.
2. **Aircraft, GSE, APU**: emissions sources from aircraft engines, airport ground support equipment (GSE), and auxiliary power units (APUs).
3. **Non-point sources**: emissions sources that are too small or too numerous to model as individual point sources. Emissions are calculated at the county level.
4. **Non-road mobile sources**: generated by the NONROAD model in the EPA National Mobile Inventory Model (NMIM). Represents emissions from a variety of combustion sources using four different fuel types.
5. **Rail/CMV sources**: locomotive and commercial marine vessel emissions.
6. **Fire sources**: emissions related to biomass burning.
7. **Biogenic sources**: emissions from vegetation and soils, computed using the Biogenic Emissions Inventory System (BEIS) model.

Further partitioning of these seven main categories into sub-categories is implemented to facilitate comparison to the EPA NEI and provide more detailed sector-specific analysis [*McDill et al.*, 2015]. Daily Alpha2 emissions files for 48 sub-categories are created using the SMOKE model described in Section 1.3.1. These files allow specific emissions adjustments to be made to reflect targeted controls on individual sectors. Adjustments we implement for the Alpha2 inventory files are discussed in Chapter 3. Additional analysis with the Alpha2 inventory is performed in Chapter 4. Further information about the inventory can be found at http://www.marama.org/technical-center/emissions-inventory/2011-inventory-and-projections.

1.5.4: Beta2 Emissions Inventory

An update to the Alpha2 inventory called the Beta2 inventory was released in July 2017 [*McDill et al.*, 2017]. This inventory is structurally organized in the same manner as the Alpha2 inventory, but includes updated emissions information based on the EPA version 6.2 modeling platform [*OAQPS*, 2015], and the version 6.3 modeling platform [*OAQPS*, 2016] for on-road mobile emissions [*McDill et al.*, 2017]. The most relevant improvement for the analysis in Chapter 4 reflected in the Beta2 inventory are to the mobile inventory sector and include [*McDill et al.*, 2017]:

- Non-road mobile: Emissions from the 2011 NEIv2 with additional corrections from Delaware.
- On-road mobile: using a new version of the MOtor Vehicle Emission Simulator (MOVES) model (version 2014a) to generate emission factors using CB05 chemistry. Corrections were applied for 15 counties in New Jersey.

More information about the Beta2 inventory and its specific improvements can be found at: http://www.marama.org/technical-center/emissions-inventory/2011-2017-beta-regional-emissions-inventory.

We worked closely with Eric Zalewsky from the New York Department of Environmental Conservation to generate the merged Beta2 emissions file for use in CMAQ. Throughout this process, we found an error in the Private Fuel Containers (PFC) emissions files and developed a series of merge scripts (used in SMOKE) to create the final merged emissions file. The error in the PFC files was announced to the modeling community and the corrected files were provided to the various modeling centers in the winter of 2018.

While most sector files were updated from the Alpha2 inventory for 2011, a total of 17 files remained un-adjusted for the Beta2 inventory [*McDill et al.*, 2017]. Merging files from the Alpha2 and Beta2 inventories resulted in inconsistent units for two variables, requiring a convoluted process of batch merging compatible individual sector files, renaming the problem variables, and finally merging the partly-merged files. Complete merged files for modeling years 2011 and 2017 were created. Analysis using these files is discussed in Chapter 4.

1.6: Research Objectives

The goal of this research is to answer four overarching questions, and provide this information to the air quality community:

1. Does the regulatory CMAQ modeling platform accurately represent the atmosphere? If not, what modifications can be made to improve this representation? How does this impact modeled O_3?
2. Can we use CMAQ and relevant data sources to determine photochemical O_3 production regimes across the model domain?
3. How does the photochemistry in the New York City pollution plume impact levels of O_3 in heavily populated areas downwind?
4. What are the important emissions sectors contributing to O_3 production in heavily populated, near-coastal, urban centers within the model domain?

The research presented in this thesis will provide the air quality modeling community answers to these questions, and contribute important insight into CMAQ model performance, a necessary tool for attainment strategy development.

Chapter 2: Developing a Top-Down Emissions Inventory

2.1: Findings from previous studies

As discussed in the introduction, emissions inventories used in regulatory air quality modeling are developed based on the EPA NEI. For some sectors, inventory estimates use *in situ* data collected at frequent intervals to derive values. For others, the estimates are based upon data that were collected years (sometimes decades) earlier and grown to more recent years [*EPA*, 2015a]. Development of emissions inventories is time consuming, requiring extensive inter-agency cooperation, making it difficult to quickly produce accurate and reliable inventories. Creating a robust method to generate inventories based on recent, reliable satellite data would allow inventories to reflect current emissions more accurately, and significantly reduce the time required to gather the necessary data. Additionally, inventories would be based on observed data for the year, rather than grown from earlier years.

In the US, the Commercial Marine Vessel (CMV) inventory is based on data collected in 2002 which is grown to the inventory year [*EPA*, 2002; 2009b]. The CMV sector is unique because most ship emissions are released in the open ocean, in regions that are relatively pristine along well traveled trading routes. This is indicated as elevated NO_2 along distinct ship tracks relative to the background when viewed from space. A few studies have explored the possibility of developing a top-down emissions inventory in various parts of the world specifically for the CMV sector. Their work will be discussed in the next few sections.

2.1.1: NO_2 Measurements from SCIAMACHY

In 2004, a study by *Richter et al.* discussed the uncertainty in emissions estimates from available inventories. *Corbett and Koehler* [2003] published an inventory based on total fuel burn for internationally registered ships that carry goods weighing greater than 100 tons, and found a total annual fuel burn of 289 Mt [*Richter et al.*, 2004]. This was nearly twice that of the fuel consumption estimate published by the international marine bunker industry [*Richter et al.*, 2004], underlining the difficulty of producing an accurate and reliable bottom-up inventory.

The coarse resolution of satellite imagery can make developing a reliable top-down emissions inventory difficult. For their study, *Richter et al.* [2004] used tropospheric column NO_2 observations from the SCanning Imaging Absorption spectrometer for Atmospheric CHartographY (SCIAMACHY) instrument to characterize commercial shipping emissions. This instrument is a nadir viewing instrument that uses the DOAS technique to measure NO_2 [*Bovensmann et al.*, 1999; *Eichmann et al.*, 2004]. Backscattered light from the Earth's surface and atmosphere between wavelengths of 425 and 450nm is used to measure the total SCD for NO_2 [*Burrows et al.*, 1999]. First, the stratosphere is measured in limb mode which requires observing the atmosphere tangentially to the Earth's surface forward along the flight path, then the SCD is measured in nadir mode by observing the atmosphere perpendicular to the Earth's surface [*Bovensmann et al.*, 1999; *Eichmann et al.*, 2004; *Noel et al.*, 2002; *Richter and Burrows*, 2002] The stratospheric component measured in limb is then subtracted from the total column measured in the nadir mode to return a tropospheric SCD [*Bovensmann et al.*, 1999; *Eichmann et al.*, 2004; *Noel et al.*,

2002]. For SCIAMACHY, a radiative transfer program called the SCIAMACHY Radiative TRANsfer Model (SCIATRAN) is used to calculate tropospheric AMFs. These are quantities that relate the tropospheric profile of absorption of NO_2 to the measured SCD and are necessary to calculate the tropospheric VCD, the desired satellite measurement [*Bovensmann et al.*, 1999; *Burrows et al.*, 1999; *Rozanov et al.*, 2002].

SCIAMACHY has a ground resolution of 30×60 km^2 and a total swath length of 960 km [*Bovensmann et al.*, 1999; *Noel et al.*, 2002]. Over the course of the last decade, satellite technology has improved immensely, and current retrievals have much higher resolution. The recent launch of the Copernicus Sentinel-5 Precursor satellite by the European Space Agency (ESA) in October of 2017 has a ground resolution of 7×7 km^2 at nadir [*Veefkind et al.*, 2012], significantly improving spatial detail from space.

This study by *Richter et al.* [2004] found a commercial shipping signal in the SCIAMACHY tropospheric column NO_2 in the Red Sea, Indian Ocean, and South China Sea regions. These areas were chosen due to their large volume of ship traffic and localization along narrow shipping lanes [*Franke et al.*, 2009; *Richter et al.*, 2004]. Comparison of the satellite data to an available commercial shipping inventory at the time of the study shows good spatial agreement (Figure 8a and b respectively).

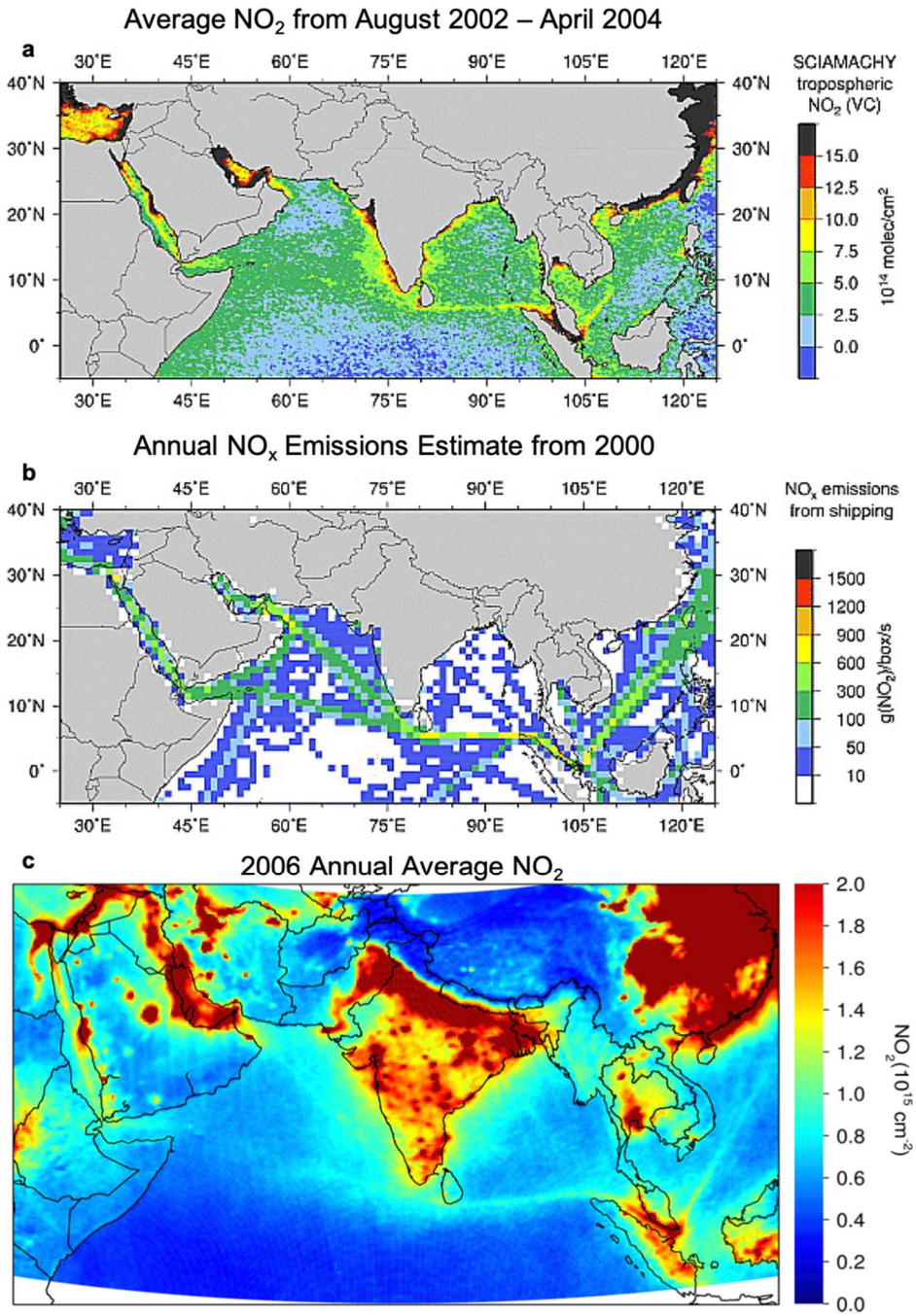

Figure 8: NO_2 from commercial shipping activity from the Red Sea through the Indian Ocean and South China Sea. (a) Tropospheric NO_2 columns derived from SCIAMACHY data from August 2002 to April 2004 (Figure 1a from *Richter et al.* [2004]), (b) NO_x emissions estimated for the year 2000 from the *Corbett and Koehler* [2003] inventory and AMVER vessel distribution data from *Endresen et al.* [2003] (Figure 1b from *Richter et al.* [2004]) (c) Annual average tropospheric NO_2 from OMI for the year 2006.

Using simple assumptions about NO_2 loss processes in the troposphere, *Richter et al.* [2004] were able to calculate lower bound estimates of annual shipping emissions for the various regions. In some locations, satellite-derived emissions were over a factor of 2 lower than inventory estimates [*Richter et al.*, 2004]. While this method is crude, it does provide evidence for creating a lower-bound estimate for commercial shipping emissions, especially in heavily trafficked areas. This is further supported by Figure 8c, which shows elevated levels of NO_2 compared to the background in the same locations shown by *Richter et al.* [2004]. We use the DOMINO level 2 data (described in Section 1.4.2) from the TEMIS website (www.temis.nl/airpollution/no2.html), create daily 0.25° latitude × 0.25° longitude level 3 gridded files, and averaged over the year 2006. All level 2 data were filtered for quality flags provided with the retrieval and require each unflagged pixel to have a Cloud Radiance Fraction (CRF) $< 30\%$ and a surface albedo $< 30\%$. The outer 15 pixels on each side of the OMI swath are removed so only the highest resolution near-nadir pixels are used (Figure 9). Clearly defined shipping lanes through the Red Sea into the Arabian Sea, Indian Ocean, and up into the South China Sea are evident.

Figure 8a and c show that satellites can detect shipping emissions in the NO_2 retrievals on a large scale, especially in clean environments with few other anthropogenic sources of NO_x. Additionally, global emissions inventories seem to accurately represent the locations of heavily traveled shipping lanes in the Indian Ocean and Red Sea regions of the world. However, generating a top-down emissions inventory from satellites that is usable for modeling purposes was not possible in 2004.

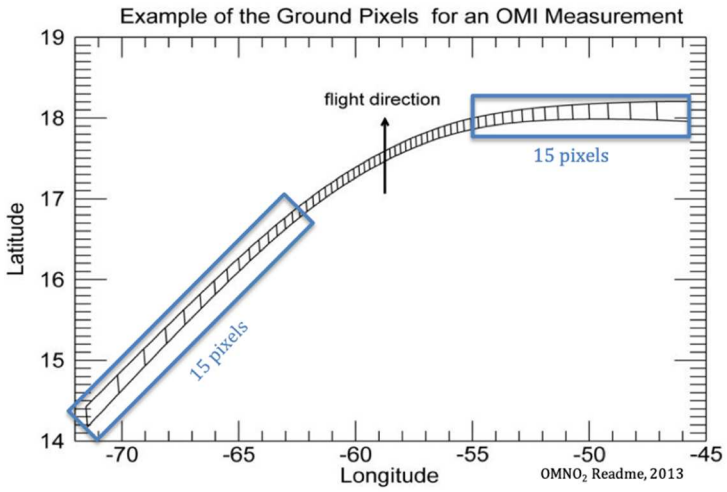

Figure 9: Description of the OMI swath (figure from *Krotkov* [2013]). The boxed OMI pixels are removed, to ensure only the highest resolution near-nadir pixels are used.

2.1.2: A Different Approach to the Top-Down Inventory using SCIAMACHY data

Development of bottom-up emissions inventories is time-intensive and results in delayed release, often years past the relevant model year. The goal of the *Lamsal et al.* [2011] study is to provide near-real time constraints on bottom-up inventories using GEOS-Chem, a global atmospheric chemistry model, and SCIAMACHY satellite data [*Lamsal et al.*, 2011; *Walker et al.*, 2010]. First, the relationship between changes in surface emissions of NO_x and column NO_2 values must be established. To do this, [2011] performs two model simulations using GEOS-Chem version 8-01-04 at a 1° latitude × 1.25° longitude resolution, driven by GEOS-4 assimilated meteorology. The first simulation uses a global NO_x emissions inventory for 2006 (created by [2011] from a variety of sources), and the second uses emissions where the global NO_x inventory for 2006 is perturbed by an arbitrarily chosen amount of 15%. Results from the two model simulations are then used in the equation from *Lamsal et al.* [2011]:

$$\frac{\Delta E}{E} = \beta \times \frac{\Delta \Omega}{\Omega}. \quad (30)$$

Equation (30) relates changes in surface NO_x emissions to simulated column NO_2 values. In Equation (30), E is the 2006 global NO_x emissions, ΔE is the imposed perturbation to the NO_x emissions, Ω is the simulated NO_2 column from GEOS-Chem based on the 2006 NO_x emissions, and $\Delta\Omega$ is the change in simulated NO_2 column based on the perturbed NO_x emissions. The β is a constant calculated for each model grid cell that describes how the change in the NO_x surface emissions affects the NO_2 column [*Lamsal et al.*, 2011]. In order to apply Equation (30) to generate a top-down NO_x emissions inventory, one must make some (likely unrealistic) assumptions:

(1) GEOS-Chem realistically simulates the global atmosphere.

(2) A modification of 15% to the global NO_x emissions is representative of how NO_x emissions are adjusted from the base year (2006) to the projected year.

(3) Changes in the NO_2 column in response to the adjustments of surface NO_x emissions detected in the GEOS-Chem model and represented by the β term in Equation (30), are representative of the differences in the tropospheric column NO_2 measured by satellites for the reference and future inventory years.

Lamsal et al. [2011] then applied this relationship to average tropospheric column NO_2 from SCIAMACHY. To do this, Equation (30) is modified to solve for the adjusted NO_x emissions inventory rather than the β term. This equation is found in *Lamsal et al.* [2011]:

$$E_j = \left(1 + \beta \frac{(\Omega_j - \Omega_i)}{\Omega_i}\right) E_i. \quad (31)$$

In Equation (31), E_j represents the monthly NO_x emissions inventory for future year j, E_i represents the corresponding monthly 2006 NO_x emissions inventory, Ω_i represents the corresponding monthly average tropospheric NO_2 column from SCIAMACHY for 2006, Ω_j represents the SCIAMACHY corresponding monthly average tropospheric NO_2 column for future year j, and β is carried over from Equation (30). To minimize error, only grid boxes where anthropogenic emissions dominate and large tropospheric NO_2 columns are detected are used. This limits the grid boxes used in this analysis to heavily populated cities, which account for approximately 80% of the global anthropogenic NO_x emissions [*Lamsal et al.*, 2011]. In this analysis, Equation (31) is applied to calculate a global NO_x inventory for 2009.

While this study outlines a fairly simple method to calculate a near-real time NO_x emissions inventory, it requires many assumptions and is best used to calculate annual anthropogenic emissions across all sectors. Since the goal is to develop a top-down emissions inventory for the commercial marine vessel inventory sector, an expanded and more specific version of this method is necessary.

2.1.3: Providing Constraints for Commercial Marine Vessel Emissions in Europe

The previously discussed studies show that satellite NO_2 data can provide detailed geographic information about commercial shipping lanes and can provide constraints to annually temporalized anthropogenic NO_x emissions estimates, however

neither study provides a robust reliable method for creating a top-down emissions inventory for the CMV sector.

Two studies published by *Vinken et al.* [2011] and [2014] use the DOMINO data, along with GEOS-Chem and a Gaussian plume dispersion model called the PARAmetrization of emitted NOX (PARANOX) [*Vinken et al.*, 2011] to provide constraints to the commercial shipping inventory in Europe [*Vinken et al.*, 2014]. An "instant dilution" approach is widely used to represent the complicated chemistry from ship emissions within a model grid cell [*Vinken et al.*, 2011; *Vinken et al.*, 2014]. This approach assumes localized emissions are immediately diluted to the entire grid cell and results in lifetimes for NO_x emissions from ships that are up to a factor of 2.5-10 too long. This simplification produces unrealistically high concentrations of NO_x and O_3 within the model [*Chen et al.*, 2005; *Davis et al.*, 2001; *Vinken*, 2010; *Vinken et al.*, 2011; *von Glasow et al.*, 2003].

The "instant dilution" method or something similar used by CMAQ may be a contributing factor to the very high values of O_3 produced over large bodies of water in model simulations [*Canty et al.*, 2015; *Loughner et al.*, 2014; *Trail et al.*, 2014; *Travis et al.*, 2016; *Vinciguerra et al.*, 2017]. With a typical CMAQ grid cell of 12 km, the "instant dilution" method immediately distributes very localized NO_x emissions from ships over the entire grid cell, diluting important localized chemical and dynamical impacts of high NO_x emissions near the source. This method is an unrealistic representation of how CMV emissions (and all point-source emissions) are dispersed in the actual atmosphere. Enhanced representation of the important chemistry on smaller spatial scales that occurs near the emission source, and in the few hours

immediately after emission will improve model production of atmospheric pollutants and surface O_3.

To address the limitations of the "instant dilution" method, *Vinken et al.* [2011] suggests a plume-in-grid approach to represent chemical aging of ship emissions in the 3 hours after emission. This method simulates production of the secondary pollutants that result from ship emissions [*Vinken et al.*, 2011]. Briefly, the PARANOX model assumes dispersion represented by 10 concentric rings extending from the pollution source. Chemical reactions and species aging are carried out within each ring in response to meteorologically driven dispersion. This method simulates the rapid chemical conditions that occur within the model grid cell immediately after emission from the shipping vessel [*Vinken*, 2010; *Vinken et al.*, 2011].

Figure 10 shows how the PARANOX model compares to measurements from the NOAA 2002 Intercontinental Transport and Chemical Transformation (ITCT) field campaign conducted ~100 km off the coast of California [*Chen et al.*, 2005]. At time of emission and extending to ~40 min after emission, NO_x concentrations are very high as they represent the initial emissions from commercial marine vessels (Figure 10a), translating to initially low O_3 concentrations due to NO titration (Figure 10b). As OH is created by reaction of NO + HO_2, concentrations increase (Figure 10c) and eventually contribute to a shorter modeled lifetime of NO_x using the plume-in-grid approach than is modeled using the "instant dilution" method. This reaction also produces NO_2 which leads to the net photochemical production of O_3 as shown in Figure 10b [*Vinken et al.*, 2011]. Figure 10d shows that the instantaneous lifetime of NO_x using this plume-in-grid approach is actually on the order of 2-4 hours rather than

~1 day as assumed by models using the "instant dilution" method [*Vinken et al.*, 2011]. This metric is calculated by dividing the NO_x concentration by the HNO_3 production rate for a given time because the dominant sink for NO_2 during the day is the production of HNO_3 via reaction with OH [*Vinken et al.*, 2011].

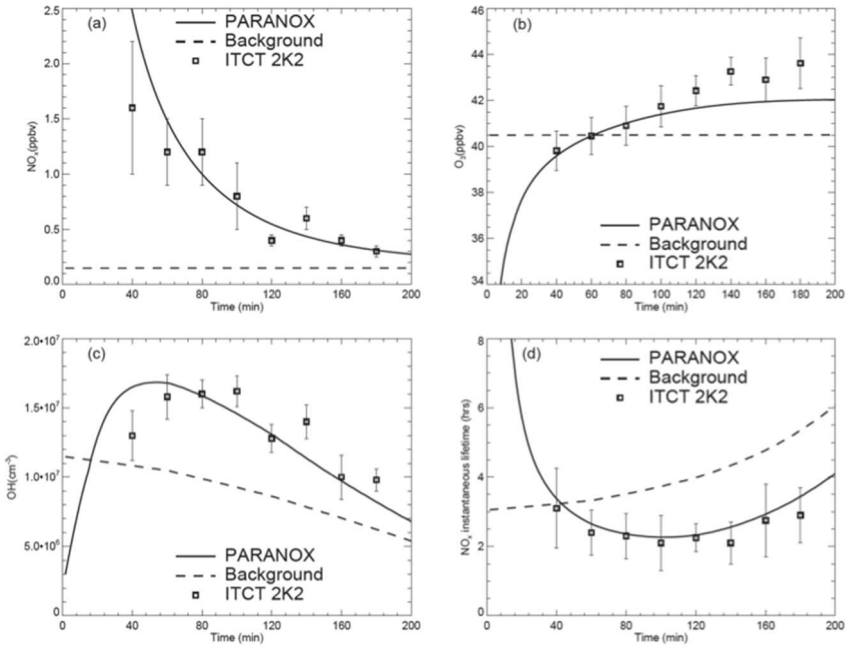

Figure 10: Comparison of observations from the 2002 ITCT field campaign [*Chen et al.*, 2005] and simulated concentrations of (a) NO_x (b) O_3 (c) OH and (d) NO_x instantaneous lifetime, from the PARANOX model. Concentrations are cross-sectional averages of ship plumes, released at 12:00 LT and depict how the species age in the 3 hours after emission. The dotted line represents background concentrations for each species plotted. This is Figure 1 from [*Vinken et al.,* 2011].

When compared to the 2002 ITCT data, PARANOX is able to accurately reproduce the concentrations of chemically important species. To reduce computational expense, *Vinken et al.* [2011] produce look up tables used in GEOS-Chem modeling to represent the small-scale complex non-linear chemistry that takes place in the 5 hours after initial emission, and within the GEOS-Chem grid cell.

Utilizing the plume-in-grid method detailed in *Vinken et al.* [2011] to correctly represent modeled ship emissions, *Vinken et al.* [2014] apply this tool to develop

constraints on NO_x emissions from ships in Europe using satellite observations and the GEOS-Chem model. Modeled and observed tropospheric NO_2 columns from GEOS-Chem and the DOMINO retrieval are compared. The OMI NO_2 retrievals are adjusted to use GEOS-Chem *a priori* column profiles rather than the TM4 profiles provided with the DOMINO retrieval to preserve consistency when comparing modeled and observed tropospheric NO_2 columns. *Vinken et al.* [2014] apply the general principals outlined by *Lamsal et al.* [2011] and add terms to account for the sensitivity of OMI NO_2 columns to the model a priori profile represented by the equation from *Vinken et al.* [2014]:

$$\gamma = \frac{\Delta\Omega_{OMI}/\Omega_{OMI}}{\Delta\Omega_{GC}/\Omega_{GC}}. \quad (32)$$

In Equation (32), Ω_{OMI} is the retrieved tropospheric NO_2 column, Ω_{GC} is the simulated tropospheric column using the same *a priori* profile as the OMI retrieval, $\Delta\Omega_{OMI}$ represents the change in the OMI retrieval due to changing the model *a priori* profile, and $\Delta\Omega_{GC}$ represents the change in simulated column NO_2 due to perturbed CMV emissions (same method for calculating β) [*Vinken et al.*, 2014]. Values of γ equal to 0 indicate no model sensitivity, and values of 1 indicate the retrieved column is entirely dependent upon the model *a priori* profile [*Vinken et al.*, 2014]. Incorporating the γ term into Equation (31) results in the following equation from *Vinken et al.* [2014]:

$$E_{top-down} = E_{a\ priori} + \left(\left(\frac{\Omega_{OMI} - \Omega_{GC}}{\Omega_{GC}}\right) \times \beta \times E_{a\ priori}\right) + \left(\left(\frac{\Omega_{OMI} - \Omega_{GC}}{\Omega_{GC}}\right) \times \gamma \times \beta \times E_{a\ priori}\right). \quad (33)$$

In Equation (33), the first term on the right side is the *a priori* bottom-up emissions used in GEOS-Chem modeling, the second term represents the scaling of the *a priori*

emissions to match the retrieved and modeled tropospheric NO_2 columns, and the third term describes the influence of the *a priori* model profile on the necessary *a priori* emissions adjustment [*Vinken et al.*, 2014]. This method produces GEOS-Chem modeled NO_2 columns that correlate well with OMI observed NO_2 columns in the Baltic Sea, Bay of Biscay, Mediterranean Sea, and North Sea study regions [*Vinken et al.*, 2014].

The major findings from *Vinken et al.* [2014] include:

(1) Tropospheric NO_2 columns observed from satellites are sensitive to induced changes in shipping emissions over shipping lanes, therefore correct representation of this emissions sector is vital to accurately simulate chemistry and pollution transport.

(2) Satellite observed columns are influenced by the choice of model *a priori*. Use of consistent emissions, dynamical schemes, etc. between the model used to calculate the satellite *a priori* profiles (TM4 for DOMINO) and the comparison model (GEOS-Chem in this case) is necessary to reduce error.

(3) A calculated top-down annual emissions inventory for the CMV inventory sector is possible. Top-down estimated emissions closely match bottom-up annual emissions estimates for shipping lanes in waters around Europe, especially emissions from the AMVER-ICOADS inventory [*Wang et al.*, 2008].

Based on these findings, it is evident that *Vinken et al.* [2014] have developed a sound method to calculate an annual estimate of commercial marine vessel emissions using satellite observations. This method can ensure the annual EPA NEI values are

within a reasonable uncertainty of satellite observations, but it cannot produce constraints for daily emissions values that are used to conduct air quality modeling. The goal is to apply this method to estimate a data-derived top-down emissions inventory value for the CMV sector for the near-coastal US region comparable to the EPA 2011NEI for the O_3 season (April – October).

2.2: Creating a Commercial Marine Vessel Inventory for the East Coast US

2.2.1: Signal from OMI

We establish that shipping lanes are visible in the tropospheric column NO_2 (DOMINO) retrieval and are coincident with the shipping lanes found in *Vinken et al.* [2014] (Figure 11). The white boxes in panels a and b of Figure 11 highlight the consistent signal in the tropospheric column NO_2 from OMI, an annually persistent feature. While it is established that a shipping signal can be found in European waters and the Indian Ocean [*Richter et al.*, 2004], is there evidence of a signal from commercial shipping emissions in the satellite data off the coast of the Eastern US?

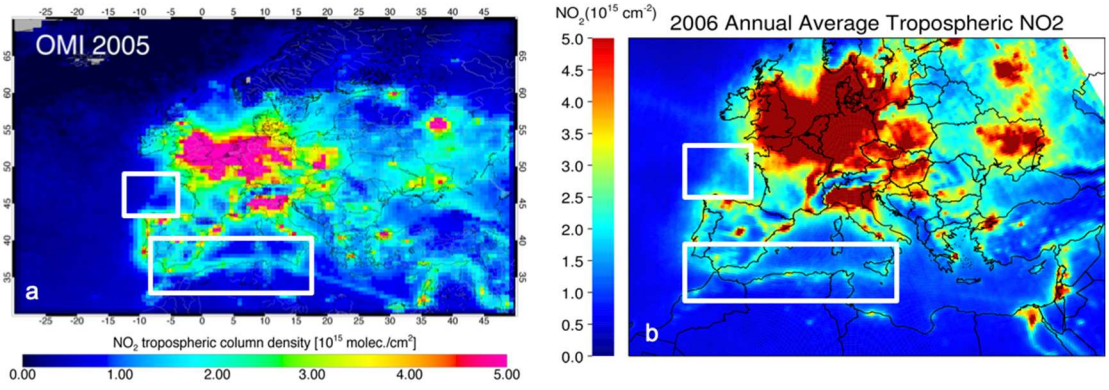

Figure 11: Annually averaged DOMINO tropospheric column NO_2 for 2005 gridded on 0.5° × 0.66° grid (a). Pixels used have a Cloud Radiance Fraction (CRF) < 50% and an albedo of < 20%. The figure comes from Figure 3 of [*Vinken et al.*, 2014]. Annually averaged DOMINO tropospheric column NO_2 for 2006 gridded on a 0.25° × 0.25° grid (b). Pixels are filtered the same way as *Vinken et al.* [2014].

Figure 12a shows what we perceive to be a signal from shipping activity across the Atlantic Ocean. Elevated NO_2 emissions are shown in areas across the Atlantic that are known to be heavily trafficked shipping lanes (Figure 12b). Unfortunately, the continental outflow from the US (dark red color in Figure 12a) extends well into the Atlantic Ocean, obscuring any NO_2 signal from CMV emissions in the satellite data.

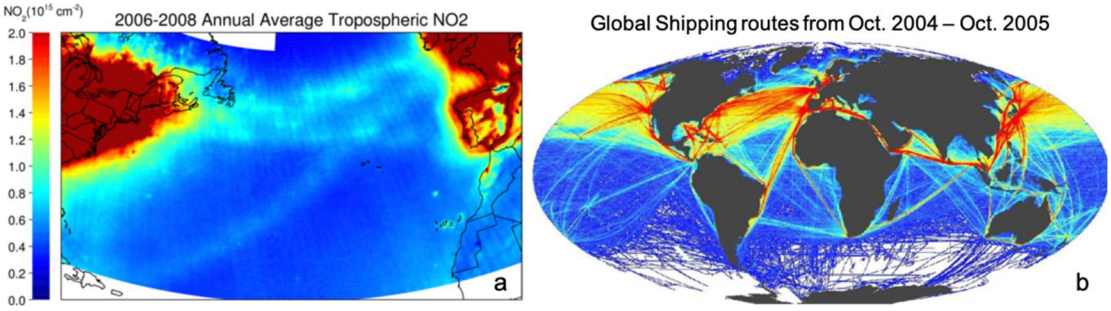

Figure 12: (a) Annually averaged tropospheric NO_2 from the DOMINO retrieval for 2006-2008. OMI pixels are filtered the same as in *Vinken et al.* [2014] (b) Ship traffic estimated from Voluntary Observing Ships Scheme data collected from October 2004 – October 2005. This figure is found in the supplementary material of [*Halpern et al.*, 2008].

Further analysis of the OMI retrieval reveals the features attributed to shipping lanes in Figure 12a may actually be artifacts in the data as a result of the model used in the retrieval. Based on personal correspondence with K. Folkert Boersma from the Royal Netherlands Meteorological Institute (KNMI) at the 2017 OMI Science Team Meeting in Greenbelt, MD, we learned the elevated NO_2 in the satellite observations across the Atlantic is due to the ship emissions used in the TM4 model to derive the *a priori* NO_2 profiles. The TM4 model is a 2° latitude × 3° longitude global Chemistry-Transport Model (CTM) with 35 vertical levels that calculates the *a priori* NO_2 profiles used in the DOMINO retrieval algorithm [*Boersma et al.*, 2007]. Anthropogenic and biogenic NO_x emissions are based on values from the Precursors of Ozone and their Effect on the Troposphere (POET) European Union project for the year 1997 [*Boersma*

et al., 2007; *Olivier et al.*, 2003]. The erroneous signal across the Atlantic Ocean is likely due to this dated emissions inventory and coarse resolution of the TM4 model.

For the TROPOspheric Monitoring Instrument (TROPOMI) (http://www.tropomi.nl/) the update to OMI launched on October 13, 2017, the retrieval algorithm is based on the updated TM5-MP model which has a resolution of 1° latitude × 1° longitude and uses the Monitoring Atmospheric Composition and Climate (MACC) emissions inventory to calculate the NO_2 *a priori* profiles [*Granier et al.*, 2011; *van Geffen et al.*, 2018; *Williams et al.*, 2017]. Analysis with TROPOMI NO_2 data will likely show a more realistic NO_2 signature across the Atlantic assuming the updated emissions inventory and TM5-MP model resolve modeling artifacts in the data. Analysis has not been completed to examine this possibility.

A recent study by *Ding et al.* [2018] used an inverse modeling algorithm called the Daily Emissions estimates Constrained from Satellite Observations (DECSO) [*Ding et al.*, 2017] and OMI observations between 2007 and 2016 to derive monthly shipping emissions estimates off the China coast. DECSO has a spatial resolution of $0.25° \times 0.25°$ and calculates the β term in Equation (30) (the sensitivity of column NO_2 to shipping emissions) [*Ding et al.*, 2017]. The transport of NO_2 across the model domain is calculated from an ensemble of 150 isotropic 2-D trajectories using the European Center for Medium-Range Weather Forecasts (ECMWF) forecasts. Trajectory calculations are performed for each model grid cell [*Ding et al.*, 2017]. DECSO assumes forecasted NO_2 emissions to be equal to emissions from the previous day, therefore updates to the emissions from satellite tropospheric column NO_2 measurements that vary from the mean by more than 3σ are considered incorrect and

a total adjustment of 3σ is used for the model grid cell [*Ding et al.*, 2017]. The trajectory analysis coupled with the Automated Identification System (AIS) data to monitor ship tracks of individual ships along the eastern China coast allow the DECSO algorithm to filter out transported NO_2 and reveal shipping lanes [*Ding et al.*, 2018]. In the future, application of the DECSO algorithm along with TROPOMI satellite data to the eastern US Coast is likely to improve monthly CMV inventory estimates, yielding similar results to *Ding et al.* [2018].

2.2.2: Using HYSPLIT

Our goal is to develop a top-down CMV inventory to compare with the EPA NEI inventory. This requires a discernable NO_2 signature in the 200 nautical miles off the US coast, known as the Exclusive Economic Zone (EEZ) [*EPA*, 2015a], and use of satellite data from the year 2011. Based on Figure 12a, contamination of the NO_2 column due to continental outflow must be addressed for the East Coast of the US due to the prevailing westerly winds. We use the HYbrid Single-Particle Lagrangian Integrated Trajectory (HYSPLIT) model [*Stein et al.*, 2015] developed by the Air Resources Laboratory at NOAA to find days during the O_3 season in 2011 that indicate Easterly wind flow. These days are assumed to have reduced anthropogenic pollution in the atmospheric column over the coastal Atlantic Ocean, allowing the NO_2 from shipping activity to be detected.

The ensemble back-trajectories end at 13:30 LST, approximately coincident with the local OMI overpass time, providing information about the origin of the air in the atmospheric column observed by OMI. All trajectories are run for three days using the NAM 12 km composite forecasts aggregated to 1-hour daily files for the CONUS

meteorology and terminate when rain is detected in the individual trajectory. Additionally, all trajectories are set to end at 50% of the model's mixed layer depth so ending trajectory heights vary from day to day. Figure 13 shows examples of the typical westerly flow (a and b), and the desired easterly flow (c and d) over the course of the O_3 season.

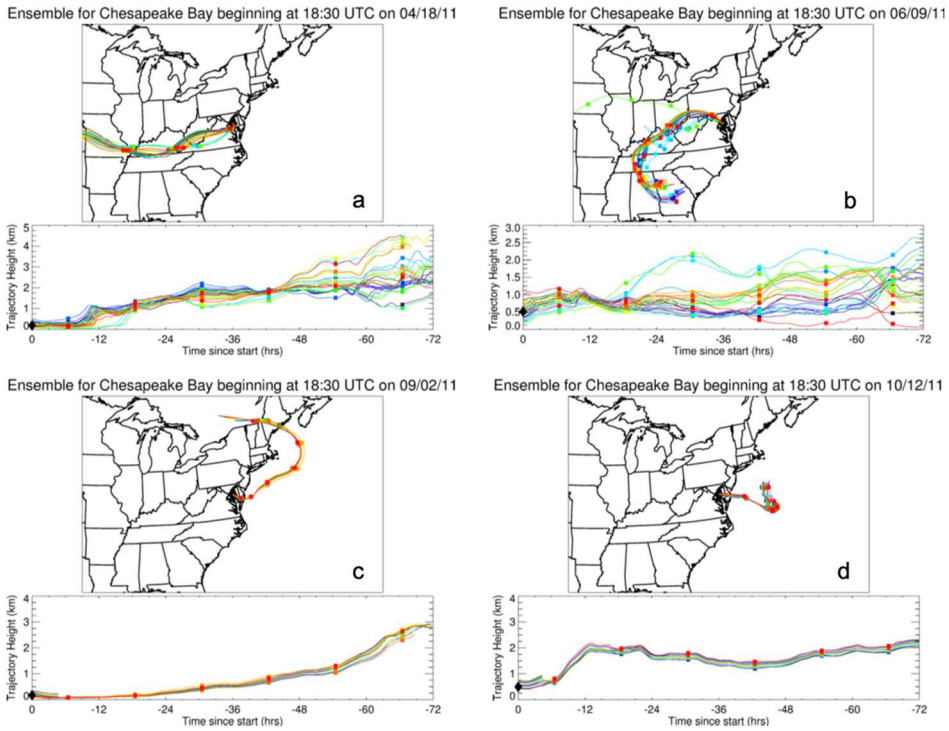

Figure 13: Ensemble 3-day back-trajectories performed from the Chesapeake Bay using meteorology from the North American Model. All trajectories terminate if rain is encountered. All trajectories begin at 13:30 LT, which coincides with OMI-overpass time. Panels (a) and (b) are examples of typical westerly atmospheric flow for the region. Panels (c) and (d) are examples of Easterly flow.

Using this filtering method, we isolate eleven days in the 2011 O_3 season that satisfy the criteria of having easterly flow and minimal influence from the US continent. In Figure 14, panel a shows the tropospheric column NO_2 averaged for the O_3 season, and panel b shows the average of the identified easterly flow days only. The striping feature in both panels results from the row anomaly in the OMI data discussed

previously in Section 1.4.2 and due to the removal of the outer most 15 pixels (Figure 9). Continental outflow is again shown off the East Coast of the US (Figure 14a) for the 2011 O_3 season, a persistent feature in the retrieved tropospheric column NO_2. In addition to the imposed filtering criteria of CRF $<$ 30%, albedo $<$ 30%, and no quality flags, we now are using data from just a handful of days in the study period. While the average shown in panel b reduces the continental NO_2 outflow distance from shore, we find this method to be unreliable to derive a top-down shipping emissions inventory for 2011. It is possible that this method could be useful if applied to earlier years, before the OMI row anomaly effected almost half of the pixels, however we are interested in developing a top-down inventory for 2011, and therefore did not pursue this prospect. Methodology suggested by the recent paper by *Ding et al.* [2018] should also be explored for application to the US east coast.

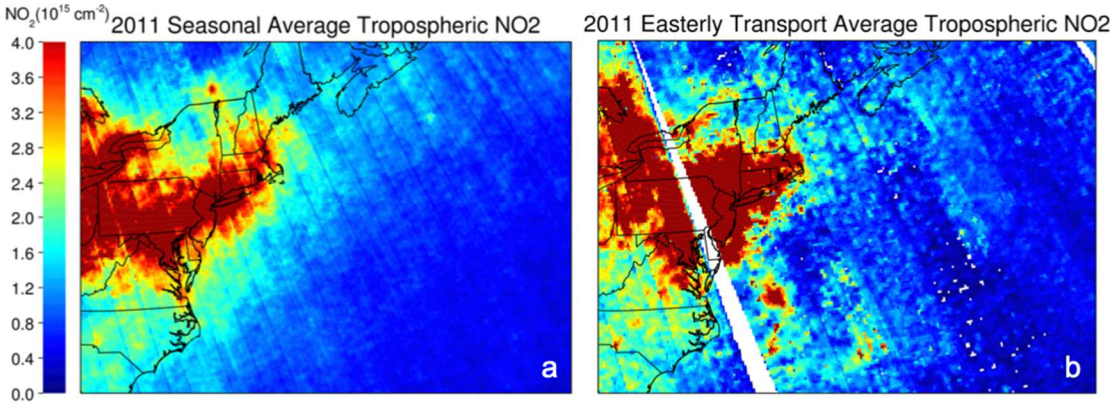

Figure 14: DOMINO tropospheric column NO_2 (a) averaged from April – October 2011 and (b) averaged easterly transport days only. Only pixels without a quality flag, and pixels with a Cloud Radiance Fraction (CRF) < 30% and an albedo < 30% are used in the average.

2.2.3: Issues with the Commercial Marine Vessel Inventory

The method to derive a top-down emissions inventory for the CMV sector described in *Vinken et al.* [2014] requires an atmospheric chemical model to provide

the *a priori* profile used in the adjusted satellite retrieval. This requires the model, and its emissions inputs, to be accurately represented in the model framework. In addition to the difficulties with the satellite data described in Section 2.2.2, we found that the CMV inventory is not represented accurately in the CMAQ model framework. Due to the increasing number of limitations to developing a reliable top-down emissions inventory for CMVs, we decided to suspend this research direction and pursue improving representation of the CMV emissions inventory in the CMAQ model framework. This effort is discussed in the next chapter.

Chapter 3: Emissions from Commercial Marine Vessels and their Role in Air Quality Policy (Published as Ring et al., 2018)

3.1: Introduction

Many studies have shown that elevated levels of pollution exist around heavily trafficked waterways and harbors [*Cooper*, 2003; *Goldberg et al.*, 2014; *Lawrence and Crutzen*, 1999; *Murphy et al.*, 2009; *Pirjola et al.*, 2014; *Williams et al.*, 2009], an important air pollution source for coastal states and states with shipping ports. Additionally, higher levels of criteria pollutants are observed at Air Quality System (AQS) monitoring sites near these coastal regions [*Gégo et al.*, 2007; *Mazzuca et al.*, 2016; *Stauffer et al.*, 2015; *Yu et al.*, 2006] than areas more inland.

In our current globalized society, it is estimated that approximately 90% of all traded goods are transported via CMVs [*Pirjola et al.*, 2014; *UN*, 2017], with emissions from CMVs contributing to approximately 15-30% of the total global anthropogenic NO_x budget [*Corbett et al.*, 2007; *Eyring et al.*, 2005; *Williams et al.*, 2009]. Due to the immense number of ships used to transport goods, and the international identity of CMVs, NO_x regulation and enforcement are difficult, even when ships are operating in near-shore shipping lanes and harbors [*Eyring et al.*, 2005; *Pirjola et al.*, 2014].

To manage the growing global use of CMVs, the United Nations (UN) proposed creation of the Inter-Governmental Maritime Consultative Organization (IMCO) in 1948, which was then officially established almost a decade later. This organization was charged with developing international guidelines to optimize maritime safety,

navigational efficiency, and to ensure all ships regardless of country flag registration can partake in international trade [*IMO*, 1948]. The original charter had no mention of controlling pollution due to shipping activity, but after the Torrey Canyon oil spill of 1967 [*IMO*, 1973; *Wells*, 2017], Article I of the original establishing document was amended to include specific reference to "prevention and control of marine pollution due to ships" [*IMO*, 1973]. Additionally, the name was eventually changed to the International Maritime Organization (IMO), to emphasize the organizations ability to act and enforce its regulations [*IMO*, 1973; 1975]. Beyond marine pollution, the IMO also realized the importance of regulating atmospheric pollution due to the ever-increasing international shipping activity. As a result, the International Convention for the Prevention of Pollution from Ships (MARPOL) was created [*IMO*, 1973]. To regulate marine pollution near land, the IMO has instituted controls for diesel engine vessels in specified Emission Control Areas (ECA); zones that extend 200 nautical miles off the coast of participating countries in their sovereign waters [*EPA*, 2008; *IMO*, 1998]. The US petitioned the IMO to include the North American continent in MARPOL Annex VI, which regulates air pollution from large ocean-going vessels, allowing the US and Canada to regulate CMV emissions within ECAs [*EPA*, 2008; 2009b]. The US was successfully added to the list of IMO participating countries in 2008, requiring all Class 3 Commercial Marine Vessels (c3 Marine) operating within US coastal waters to comply with IMO regulations [*EPA*, 2008].

Vessel age is important when determining emissions regulations. As of 2015, approximately 50% of the c3 Marine global fleet is over 20 years old, approximately 20% is between 10-20 years old, and approximately 30% is less than 10 years old [*UN*,

2015]. This means that ships younger than 20 years old (about half of the global fleet) are required to meet the Tier I IMO emissions regulations which require emission rates to be no larger than 17 g/kWh of NO_x when at idle [*IMO*, 2014]. As more of the global fleet is retired, new vessels must meet the more stringent global Tier II regulations (14.4 g/kWh of NO_X at idle) and Tier III regulations (3.4 g/kWh of NO_X at idle) if operating within ECAs [*IMO*, 2014].

The main engines of most commercial marine vessels are run solely for propulsion while auxiliary engines are run continuously to meet all other energy demands for ship operation. NO_x emissions rates from these two engine types are highly dependent upon fuel composition and engine temperatures. The slower the ships are moving, the longer and hotter these engines are running, resulting in higher NO_x emissions [*Cooper*, 2003]. CMVs are also a significant source of large particles called giant cloud condensation nuclei, contributing to enhanced boundary layer cloud formation [*Sorooshian et al.*, 2015] as well as particulate matter with an aerodynamic diameter less than 2.5 μm ($PM_{2.5}$), a criteria pollutant that contributes to hundreds of thousands of premature deaths globally [*Cohan and Chen*, 2014; *Cohen et al.*, 2005; *Corbett and Koehler*, 2003; *Pope et al.*, 2002].

Elevated levels of tropospheric O_3 over CMV traveled bodies of water have been measured by both in situ and remote techniques [*Cleary et al.*, 2015; *Goldberg et al.*, 2014]. Advection of this polluted air over coastal land and cities may contribute to the elevated pollution over these regions [*Loughner et al.*, 2011; *Loughner et al.*, 2014; *Mazzuca et al.*, 2017; *Stauffer et al.*, 2015] and at coastal AQS monitoring sites. For major metropolitan cities near heavily trafficked CMV areas like Baltimore, MD,

Philadelphia, PA, and New York, NY, the development of attainment strategies addressing CMV emissions will become increasingly important as global shipping activity is projected to increase in the future [*EPA*, 2009b; *McDill et al.*, 2015].

In this Chapter, we discuss the role of CMV emissions on regional air quality, and the representation of this pollution source within the CMAQ model [*Ring et al.*, 2018]. We review the necessary adjustments made to the vertical distribution of emissions from the largest (class 3) CMVs and examine the effect of this adjustment on surface O_3 production for various model simulations conducted for years 2011 and 2018. Comparisons of modeled surface O_3 to AQS data, and modeled column formaldehyde (HCHO) and NO_2 to satellite measurements, are used to evaluate model performance for 2011. Finally, we quantify the effect of an improved model framework for a 2018 SIP attainment strategy developed by the Maryland Department of the Environment (MDE) [*Ring et al.*, 2018].

3.2: Commercial Marine Vessel (CMV) Emissions Adjustment

3.2.1: Using the Community Multiscale Air Quality (CMAQ) Model

For this analysis, we use an EPA approved regulatory air quality model used by state and federal agencies to develop surface O_3 attainment strategies called CMAQ (described in Section 1.5.1). The model domain is represented by the outlining black box in Figure 15.

All anthropogenic emissions used for this study are the MARAMA Alpha 2 version described in Section 1.5.3. Various sector emissions are gridded to CMAQ

resolution and merged into daily 3-D, temporally varying input files using SMOKE version 3.6 [*CMAS*, 2014b] described in Section 1.3.1. Model output from CMAQ is generated for June 1st through August 31st for 2011 and 2018, the three hottest and most important months for photochemical O_3 production during the O_3 season (April-October). We compare CMAQ output from the 2011 base case simulation to observations for the same period. The 2018 CMAQ output is used to examine the effectiveness of future emissions reductions and proposed policies, discussed later in Chapter 3 [*Ring et al.*, 2018].

3.2.2: CMV Emissions Inventory Development

This study focuses on the Class 3 Commercial Marine Vessel (c3 Marine) inventory, which represents emissions for marine diesel engines with fuel displacement of 30 liters/cylinder or larger [*EPA*, 2002; 2009b; 2015a]. This sector mainly consists of cruise ships and international open ocean vessels, used in transporting consumer goods and resources.

The EPA generates the total c3 Marine emissions values for the NEI2011 by applying growth factors to ship emissions data acquired in 2002 [*EPA*, 2002; 2009b]. These growth factors account for a variety of policies and changes in shipping activity that affect the 2011 inventory year, including the ECA regulations described earlier and global NO_x and sulfur dioxide (SO_2) controls [*EPA*, 2015a; *McDill et al.*, 2015]. The spatial distribution of CMV emissions are generated using data from the Research and Innovative Technology Administration's Bureau of Transportation Statistics National Transportation Atlas Database, the US Census Bureau, GIS shapefiles provided by ports, and satellite imagery from sources such as Google Earth [*EPA*, 2009a; *ERG*,

2010]. This method was refined for developing the 2014 NEI, improving county designation and grid point locations within state waters [*EPA*, 2015b]. Similar studies have used data from AIS, which provides detailed information about ship location, speed, ship activities, navigational plans, and many other parameters [*Chen et al.*, 2017a; *Chen et al.*, 2017b; *Chen et al.*, 2016]. Due to the large data volume, computational intensity, complexity and scale of US coastal operations, AIS was not used to develop 2011 or 2014 CMV emissions in the NEIs, however it is recommended by the EPA along with State and Local agencies for future inventory development [*EPA*, 2015b].

For the c3 Marine sector, the emissions inventory is divided between off-shore and near-shore emissions. The EPA is responsible for the development of off-shore c3 Marine emissions, designated as outside state waters but within the country's established Exclusive Economic Zone (EEZ) and therefore the ECA. Conversely, near-shore emissions are designated to be within county (and therefore state) waters extending approximately 3 miles off the coast, and thus the EPA requests that states gather and report this information [*EPA*, 2015a; *McDill et al.*, 2015]. If near-shore emissions from states are incomplete, EPA generated emissions are used to supplement.

Figure 15 shows the spatial extent of near-shore (a) and off-shore (b) emissions within our CMAQ modeling domain. The off-shore emissions are designated as point sources, allowing for the vertical distribution of emissions above the surface, reflecting the stack heights of the ships, along with plume rise and dispersion of the emissions. Near-shore c3 Marine emissions are designated as area sources, so all emissions occur only in the surface layer of the model. This different designation results in inconsistent

modeling of c3 Marine emissions and erroneously places high levels of NO_x and other c3 Marine pollution from the near-shore emissions files at the surface of heavily trafficked, near coastal waterways like the Chesapeake and Delaware Bays, New York Harbor, and Long Island Sound. It also prevents CMAQ from accurately simulating vertical mixing and transport of these emissions because they are emitted too close to the surface.

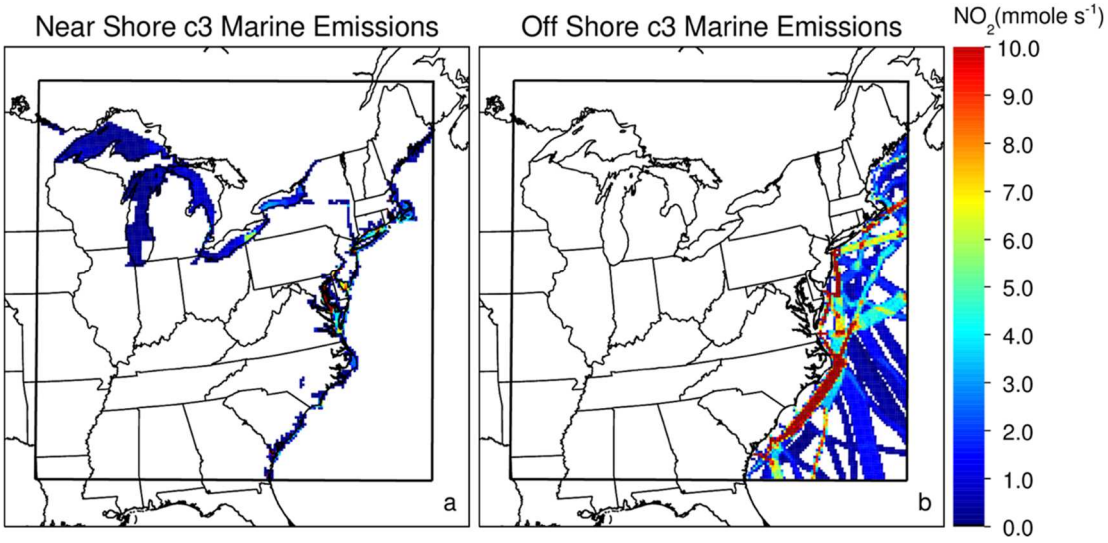

Figure 15: Average class 3 commercial marine vessel (c3 Marine) NO_2 inventory emissions at 2pm LST for June, July, and August 2011 are shown for (a) near-shore and (b) off-shore emissions files. Black boxes in (a) and (b) outline the CMAQ model domain.

Additionally, in the Great Lakes region the near shore emissions are spread out across the surface of the lakes in US waters. This is because the area source designation distributes the emissions out across the county boundaries that extend over water, stopping at the US-Canada border as shown in Figure 16. Comparing the US near-shore and Canadian near-shore c3 Marine emissions, it is evident that shipping lane surrogates were used to develop the Canadian emissions but were not used, or were used incorrectly, to develop the US emissions shown in Figure 16a. After further

research, we found surrogates were developed for commercial marine traffic in the Great Lakes (Figure 16b), however they were not present in the EPA emissions inventory ftp database: ftp://ftp.epa.gov/EmisInventory/2011v6/v2platform/training.

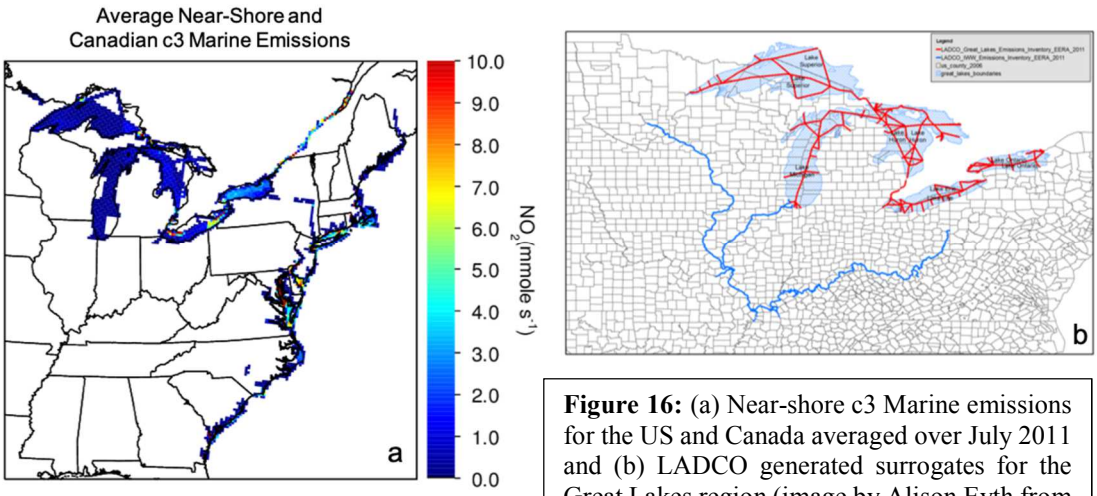

Figure 16: (a) Near-shore c3 Marine emissions for the US and Canada averaged over July 2011 and (b) LADCO generated surrogates for the Great Lakes region (image by Alison Eyth from the EPA, April 14, 2015)

We believe the white geometric areas in Lake Michigan (Figure 16a) representing no near-shore emissions indicate that surrogates did influence inventory development but were not used correctly. As shown in Figure 16b, any county that has a shipping lane extend through it has near-shore area source emissions attributed to the entire county. If the ship tracks do not extend through the county, no emissions are designated in those areas, which explains the strange shape of the missing near-shore emissions. The issues of missing surrogate files in the EPA inventory ftp database and the clear difference between the Canadian and US near-shore c3 Marine emissions distribution were communicated to the appropriate people at the EPA. These should also be rectified in future inventories.

3.2.3: Class 3 Commercial Marine Vessel Emissions Adjustment

As discussed in the previous section, near-shore c3 Marine emissions occur within the surface layer of the model while off-shore c3 Marine emissions are vertically distributed in model layers above the surface. We attempt to rectify this discrepancy by using an appropriate average profile calculated based on nearby, off-shore c3 Marine emissions, and apply this profile to the near-shore c3 Marine emissions.

First, we must determine how the near-shore and off-shore emissions interface with each other in order to adjust the near-shore emissions most accurately. Figure 17 shows how the near-shore and off-shore emissions meet along the entire Eastern US coast. In all 7 panels (a-g) of Figure 17, overlap between the near-shore emissions (blue circles) and off-shore emissions (red squares) are identified and highlighted by yellow circles. This overlap is an oversight in the emissions development process and must be rectified. Further analysis shows that the emissions from the near-shore and off-shore files for the overlapping points are not identical, meaning the sources for the emissions estimates at these grid points are not the same. This supports the notion that this mistake likely results from combining input from SLT agencies with EPA emissions estimates.

Previous modeling performed with unadjusted emissions files therefore used c3 Marine emissions that were too high at these overlapping grid points, allocating a gross overestimation of emissions within the surface layer of the model. To correct this issue, we removed all overlapping grid points from the near-shore c3 Marine inventory file. This might not be the best method, since the EPA generally defers to SLT inputs, however, it is these SLT emissions that are erroneously allocated to the surface layer of the model and need further adjustment. We elected to keep the off-shore emissions

wherever possible because they required no modifications, and therefore match most closely to the government provided emissions [*Ring et al.*, 2018].

In addition to accentuating the overlapping emissions, Figure 17 shows the spatial extent of the near-shore emissions. In all 7 panels, it is evident that the emissions extend well over land, beyond where any large tanker or shipping vessel could travel. It is likely some of these grid points contained emissions that were incorrectly designated as c3 Marine, however further investigation is needed to determine how best to correct this problem. With the resources available, it was not feasible to adjust the horizontal spatial distribution of the near-shore emissions, but this issue was made apparent to the inventory development team at the EPA and modifications should be made for future emissions inventories.

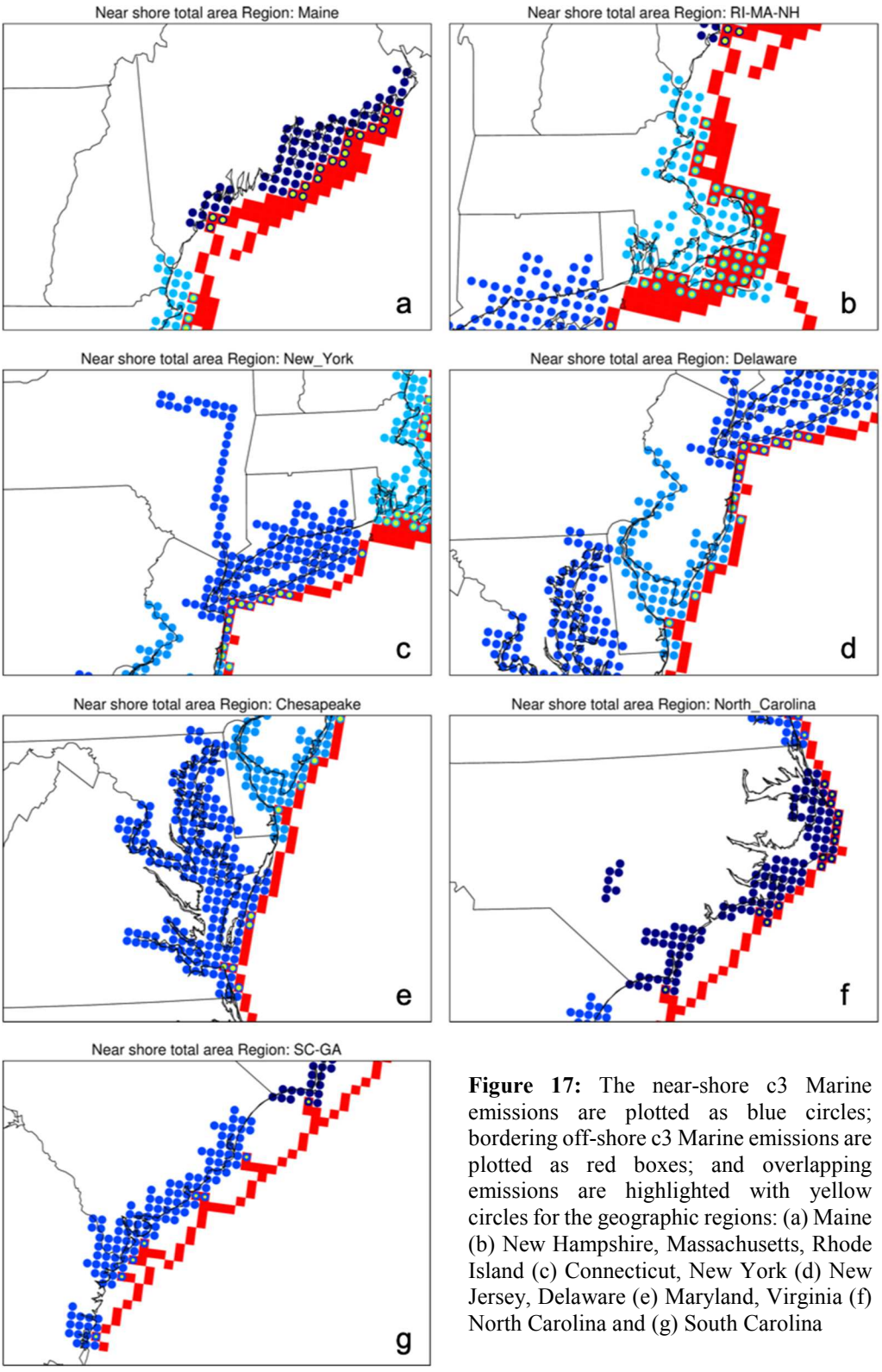

Figure 17: The near-shore c3 Marine emissions are plotted as blue circles; bordering off-shore c3 Marine emissions are plotted as red boxes; and overlapping emissions are highlighted with yellow circles for the geographic regions: (a) Maine (b) New Hampshire, Massachusetts, Rhode Island (c) Connecticut, New York (d) New Jersey, Delaware (e) Maryland, Virginia (f) North Carolina and (g) South Carolina

After removing overlapping emissions, we had to determine how best to adjust the near-shore emissions to reflect the vertical distribution. Since the goal of this work is to represent the entire c3 Marine inventory sector (both off-shore and near-shore emissions) in a consistent manner, determining how the off-shore inventory files vary from day to day, hour by hour, is crucial to creating a sound method for adjusting the near-shore file. To determine if there were temporal and geographic variations in the off-shore emissions vertical distribution, we chose test grid points near large shipping ports to analyze (Figure 18). These test points highlight areas that are highly trafficked by class 3 vessels and represent off-shore emissions that border the near-shore c3 Marine emissions.

To create a formula for adjusting the near-shore inventory file, we needed to determine the percent of the total emissions in each layer for the off-shore c3 Marine inventory file. For example, in Figure 19, we see that for all four test locations, the largest percent of the emissions are placed in layer 3 of the model for all hours (royal blue circles in panels a-d). Throughout the day, anywhere between 60-80% of the emissions are put into layer 3, with varying amounts in the other layers depending on geographic location. Based on this finding, it is evident that preserving geographic and temporal variation found in the off-shore emissions is necessary to adjust the near-shore emissions in a sound manner.

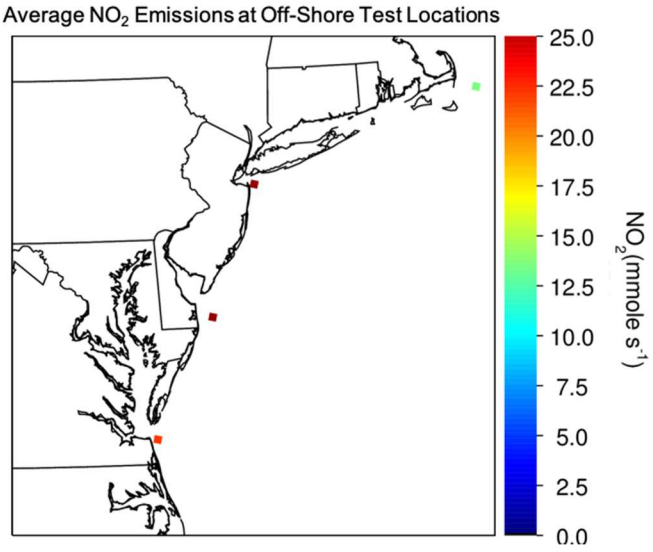

Figure 18: Off-Shore c3 Marine grid points chosen as test locations to determine temporal variation of emissions. The four grid points are colored by the average NO_2 emissions in July 2011.

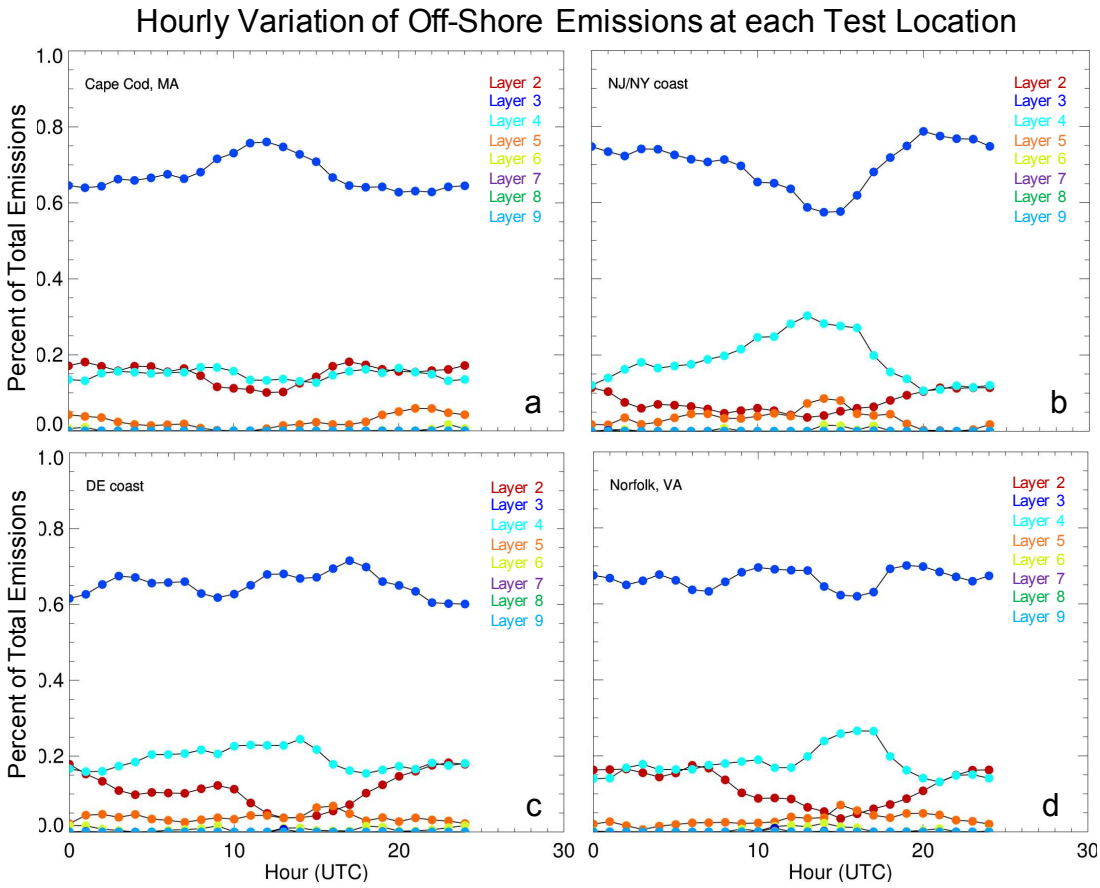

Figure 19: Hourly variation in the percent of total emissions that are present in each model layer for test locations (a) Cape Cod, MA, (b) NJ/NY coast, (c) DE coast, (d) Norfolk, VA. The exact geographic locations of the test grid points are the shown in Figure 18.

After determining geographic variation, it became evident that regional division of the near-shore files is necessary. As shown in Figure 17 (a-g), natural breaks in the near-shore c3 Marine inventory created 7 logical adjustment regions. Figure 20a shows how the near-shore c3 Marine emissions are divided into 7 adjustment regions. Since the majority of the near-shore inventory grid points do not directly border off-shore inventory grid points, we create an average distribution profile for each adjustment region. This average profile is created from all off-shore grid points that border the specified adjustment region. An example is shown as gray boxes in Figure 20b for the MD/VA adjustment region [*Ring et al.*, 2018].

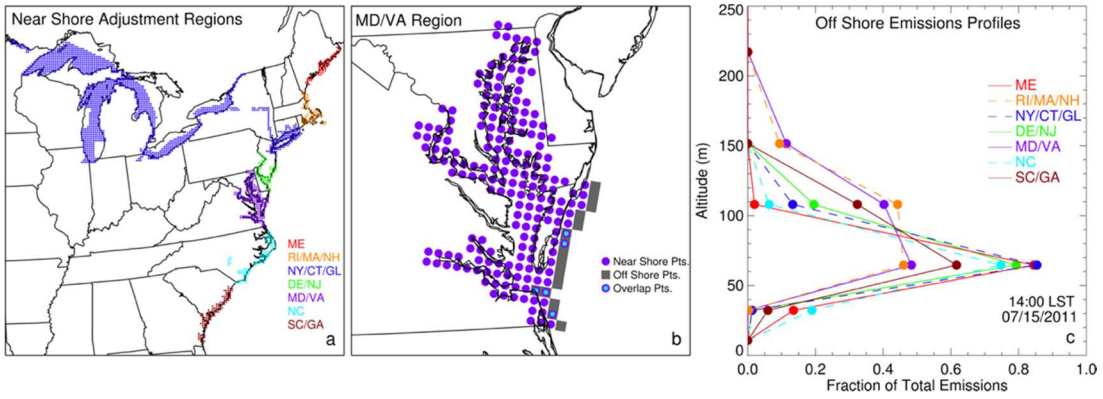

Figure 20: (a) Near-shore c3 Marine emissions geographically divided into 7 adjustment regions. All near-shore c3 Marine emissions grid points are color coded to show regional designation. (b) The MD/VA region near-shore c3 Marine emissions grid points (purple filled circles), off-shore emissions grid points (gray squares), and overlapping grid points (purple and blue circles). (c) Average vertical fractional distribution of off-shore c3 Marine emissions for each region at 14:00 LST on July 15, 2011 plotted at the half-height of the emissions layer.

Importantly, the Great Lakes near-shore emissions do not border any off-shore grid points, therefore, we attribute the profile for the NY/CT region, the adjustment region that most closely connects, to the Great Lakes (Figure 20a).

The calculated average profile for each adjustment region was then used to vertically distribute all near-shore emissions within the corresponding adjustment

region. Due to the temporal variation shown in Figure 19, the average profile was calculated for each hour of each day and applied to the appropriate near-shore region. As an example, average vertical distribution profiles calculated for each adjustment region at 14:00 EST on July 15, 2011 are shown in Figure 20c [*Ring et al.*, 2018].

Finally, all adjusted near-shore c3 Marine emissions were removed from the daily area source near-shore file and added to the corresponding daily point source off-shore file to create a single c3 Marine emissions inventory file. This ensures all c3 Marine emissions data are modeled consistently within CMAQ, as point source emissions, with appropriate vertical distribution [*Ring et al.*, 2018].

3.3: Modeling Impacts for 2011

To analyze the impact of this adjustment to the c3 Marine inventory sector on air quality, CMAQ simulations are performed. In addition to baseline and adjusted c3 Marine model simulations, model runs that incorporate observationally driven adjustments to the on-road mobile emissions inventory [*Anderson et al.*, 2014; *Travis et al.*, 2016], and modifications to the CB05 chemical mechanism [*Canty et al.*, 2015] are completed.

The adjustment to on-road mobile NO_x emissions throughout the modeling domain addresses an overestimation of the NO_x emitted from car tail pipes. Analysis of aircraft observations in the Baltimore-Washington area collected during the Deriving Information on Surface Conditions from Column and Vertically Resolved Observations Relevant to Air Quality (DISCOVER-AQ) 2011 campaign indicate emissions from this sector are high by a factor of two in the EPA inventory [*Anderson*

et al., 2014; *Travis et al.*, 2016]. While this conclusion from *Anderson et al.* [2014] was originally challenged by the EPA, subsequent studies have confirmed the results for other areas across the US, providing further evidence for reducing NO_x emissions from cars. Consequently, we apply a 50% reduction to on-road mobile NO_x emissions throughout the entire domain. The next adjustment corrects the expectation that the alkyl-nitrate radical group (NTR) in CB05, has a lifetime of ~10 days for loss by photolysis. For simplicity, CB05 groups species that react similarly in the atmosphere. This can lead to over simplifications of important chemical reactions, as in this case. The 10-day lifetime for the NTR group is much longer than the actual photolytic lifetime of most of the chemical species comprising the NTR group, so we reduce the lifetime by a factor of 10 to a more realistic ~1-day lifetime [*Canty et al.*, 2015]. It is important to note that CB05 assumes 100% recycling of NO_x, which contributes to more O_3 production within the model than is realistic [*Canty et al.*, 2015]. The final adjustment made to the various modeling simulations is the change to the vertical distribution of c3 Marine emissions explained in section the previous section. Table 2 details the various model and emissions inventory adjustments made for each modeling scenario discussed in this paper.

Table 2: Description of the four CMAQ modeling scenarios and their appropriate inventory and model adjustments.

MODELING SCENARIO	C3 MARINE EMISSIONS ADJUSTMENT	ON-ROAD MOBILE EMISSIONS INVENTORY ADJUSTMENT	ALKYL NITRATE RADICAL (NTR) LIFETIME ADJUSTMENT
BASELINE	No adjustment	No adjustment	No adjustment
C3 ADJUST	Adjusted emissions	No adjustment	No adjustment
SCIENCE	No adjustment	Adjusted emissions decrease NO_x by 50% (Anderson et al. 2014, Travis et al. 2016)	Reduced NTR lifetime from 10 days to 1 day (Canty et al. 2015)
C3 SCIENCE	Adjusted emissions	Adjusted emissions decrease NO_x by 50% (Anderson et al. 2014, Travis et al. 2016)	Reduced NTR lifetime from 10 days to 1 day (Canty et al. 2015)

We use average maximum 8-hr O_3 ($AM8O_3$) as a metric to analyze model output and compare with ground-based observations. We follow the EPA guidelines for calculating maximum daily average 8-hr O_3 (MDA8) [*EPA*, 2015c], which are summarized as follows. A forward running 8-hr mean is calculated for each day at each grid cell within the model. The MDA8 within a 3 × 3 grid is then attributed to the center grid cell. For the June, July, August (JJA) time frame, we average the MDA8 for the top 10 days above 60 ppb at each grid cell. This is known as the $AM8O_3$ value. To calculate $AM8O_3$ for corresponding simulations of future air quality, in this case 2018, the MDA8 assigned to the center grid cell of the 3 × 3 grid in 2018 is co-located with the MDA8 cell used in the 3 × 3 grid in 2011. This method highlights air quality on the worst days in the study period. Air quality policy is created using this metric, therefore, the focus of attainment strategies is to reduce poor air quality on the worst days.

For the rest of this analysis, the geographic area is narrowed from the full model domain to a region encompassing the coastal Mid-Atlantic and Northeast states, highlighting locations with large, highly active commercial ports near heavily populated areas with some of the highest levels of observed surface O_3. The study region is outlined in subsequent figures by a black dashed line.

Figure 21a shows $AM8O_3$ for the baseline model simulation. As shown in Table 2, the 2011 Baseline simulation does not include any model adjustments. The 2011 c3 Adjust scenario (Figure 21b) incorporates the near-shore c3 Marine vertical distribution adjustments. The difference between these two simulations (Figure 21c) reveals the areas within our study domain that show considerable changes in surface $AM8O_3$ due to the improved vertical representation of c3 Marine emissions. The decrease in surface $AM8O_3$ over the Chesapeake Bay and closely surrounding areas is due to the c3 Marine adjustment moving O_3 precursor emissions off the surface and distributing them vertically within the atmosphere. This modification allows some emissions to be vented out of the boundary layer, improving model representation of atmospheric pollution transport, resulting in a significant (~6 ppb) decline of surface $AM8O_3$ over the Chesapeake Bay. The increase of surface $AM8O_3$ shown in the New York and Connecticut region is due to increased pollution transport from upwind c3 Marine sources, and the non-linear chemistry that controls O_3 production. This will be discussed further in the next section.

Comparisons of surface O_3 model output to surface O_3 data from AQS locations are shown for the 2011 Baseline (Figure 21d) and 2011 c3 Adjust (Figure 21e) modeling scenarios. Within our study region, we compare AQS $AM8O_3$ calculated

from observations to modeled $AM8O_3$ from the CMAQ grid point closest to the AQS site. Comparison of Figure 21 panels d and e show the effect of the c3 Marine emissions vertical distribution adjustment. Modeled $AM8O_3$ at some AQS locations increases, by as much as a factor of two, while at others it decreases, however, almost all the modeled $AM8O_3$ is too high compared to observations. For instance, the AQS site at Greenwich Point Park, CT has a measured $AM8O_3$ value of ~80 ppb and a modeled $AM8O_3$ value of ~150 ppb for both scenarios. A high bias in CMAQ model output of surface $AM8O_3$ has been shown in prior studies and determining the reasons for this high bias are areas of active research [*Canty et al.*, 2015; *Loughner et al.*, 2014; *Trail et al.*, 2014; *Travis et al.*, 2016; *Vinciguerra et al.*, 2017]. The comparisons shown in Figure 21d and e highlight the limitations of CMAQ to accurately model surface O_3 on specific days, under certain meteorological conditions, particularly for coastal regions.

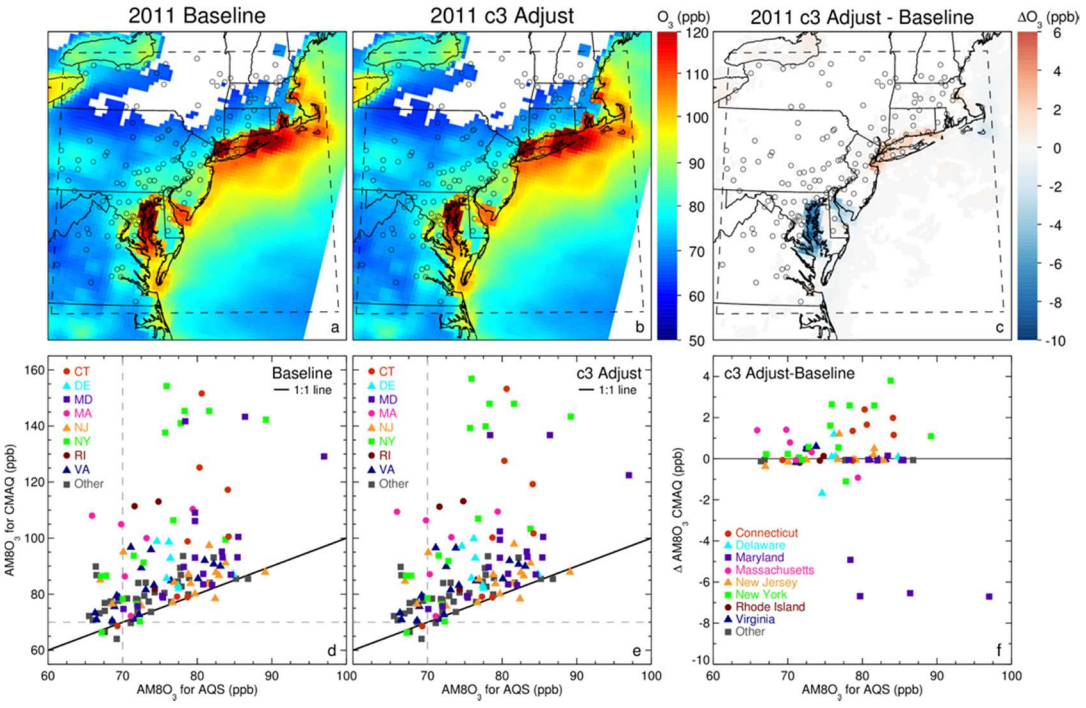

Figure 21: Average maximum 8-hr ozone ($AM8O_3$) for June, July, and August 2011 for (a) Baseline and (b) c3 Adjust model scenarios. If the $AM8O_3$ criteria are not met, model output is not shown (white regions within domain). Black dashed lines in upper plots outline the focus region for this study. Open

black circles represent AQS O_3 monitoring station locations. (c) The $AM8O_3$ difference between Baseline and c3 Adjust. (d) A scatter plot of $AM8O_3$ for Baseline vs. AQS data, with points color coded by state. (e) A scatter plot of $AM8O_3$ for c3 Adjust vs. AQS data. (f) The change in $AM8O_3$ between the c3 Adjust and Baseline model scenarios at AQS locations.

Figure 21f shows the change in modeled surface $AM8O_3$ at each AQS location when the vertical distribution of c3 Marine emissions is improved. Model values at AQS sites with differences less than 0.05 ppb are not included. We find the largest increases of modeled $AM8O_3$ at some AQS sites in New York and Connecticut, discussed in the next section, and we see the largest decreases at some AQS sites in Maryland. At the AQS site in Furley, MD, the model shows an $AM8O_3$ decrease of ~4.9 ppb, while the Edgewood, MD, Essex, MD, Calvert, MD, Blackwater NWR, MD sites all show decreases of over 6 ppb. All five AQS sites border the Chesapeake Bay, with Essex, Edgewood, and Furley located near Baltimore, MD. This reduction of modeled $AM8O_3$ in Maryland is of considerable magnitude, and an important result for state and federal agencies developing air quality policy [*Ring et al.*, 2018].

3.4: Evaluation of CMAQ Output with Satellite Retrievals

The photochemical production of O_3 is non-linearly dependent upon ambient NO_x and volatile organic compound (VOC) concentrations [*Jacob*, 2000; *Kleinman*, 2005; *Kleinman et al.*, 2001; *Sillman*, 1999; 2002]. This dependence leads to an optimal VOC:NO_x ratio that produces the maximum amount of tropospheric O_3 and represents the transition region between two atmospheric states: one where O_3 production is limited by the concentration of VOCs (VOC-sensitive) and the other where O_3 production is NO_x-sensitive. Understanding the state of the actual atmosphere, along

with how O_3 production is represented within regulatory air quality models, is crucial for developing attainment strategies that will properly inform air quality policy decisions.

If the local atmosphere is NO_x-sensitive, reducing NO_x emissions will have the desired policy effect of decreasing tropospheric O_3 concentrations. In a locally VOC-sensitive environment, reducing NO_x will have the undesired effect of increasing local concentrations of tropospheric O_3, until the reductions of NO_x are large enough to place O_3 production in the NO_x-sensitive regime. Generally, VOC-sensitive conditions are present in megacities and major metropolitan areas such as New York, NY, Houston, TX, and Los Angeles, CA [*Duncan et al.*, 2010; *Kleinman*, 1994; *Kleinman et al.*, 2000; *Madronich*, 2014; *Mazzuca et al.*, 2016], making air quality control especially challenging for these areas. In a VOC-sensitive environment, reductions in both VOCs and NO_x are typically necessary to improve surface O_3. Previous studies have shown that the Baltimore-Washington area has successfully transitioned to a NO_x-sensitive regime [*Duncan et al.*, 2010; *Goldberg et al.*, 2016; *He et al.*, 2013a; *Liao et al.*, 2014]. The behavior of surface O_3 in the CMAQ simulations presented in Figure 21c indicate NO_x-sensitive conditions for the Baltimore-Washington region because reductions of surface NO_x emissions, due to the adjustment of vertical profile of c3 Marine emissions, lead to a decrease in modeled surface O_3 (Figure 21c and f). Conversely, the surface O_3 increases shown in the New York City, Connecticut, and Long Island Sound region in Figure 21c are indicative of a region where O_3 production is VOC-sensitive, at least within the model.

Further analysis into the photochemical regime for O_3 production in the New York metropolitan area is performed using OMI satellite observations of column HCHO and NO_2. Daily retrievals of HCHO and NO_2 on a 0.25° latitude × 0.25° longitude grid were used to calculate average HCHO and NO_2 for June, July and August 2011.

We first calculate the standard deviations (σ) of the HCHO and NO_2 data at each grid point. We require there to be at least 10 coincident days of data for both HCHO and NO_2 at each grid point, that fall within two standard deviations (2σ). Finally, we calculate the average HCHO and NO_2 values at each grid point over the period [*Ring et al.*, 2018].

For comparison to CMAQ, we apply the averaging kernel (AK) from the retrievals to the model output for HCHO and NO_2. The AKs were calculated by dividing the Air Mass Factor (AMF) for HCHO and the tropospheric AMF for NO_2 by the scattering weight reported for each retrieval, as described in *Gonzalez Abad et al.* [*2015*]. Model output from 14:00 LST, was log-linearly interpolated to the satellite pressure level at each model grid point, and then multiplied by the corresponding AK from the closest overlapping satellite pixel. The resulting product was then integrated to calculate a column value for both HCHO and NO_2, comparable to the satellite column observations. These CMAQ-based columns were then averaged onto the same 0.25° latitude × 0.25° longitude grid as the satellite data, based on the criteria used to calculate the average satellite HCHO and NO_2 values, detailed above. This method ensures consistency between the satellite data and model output used in the analysis.

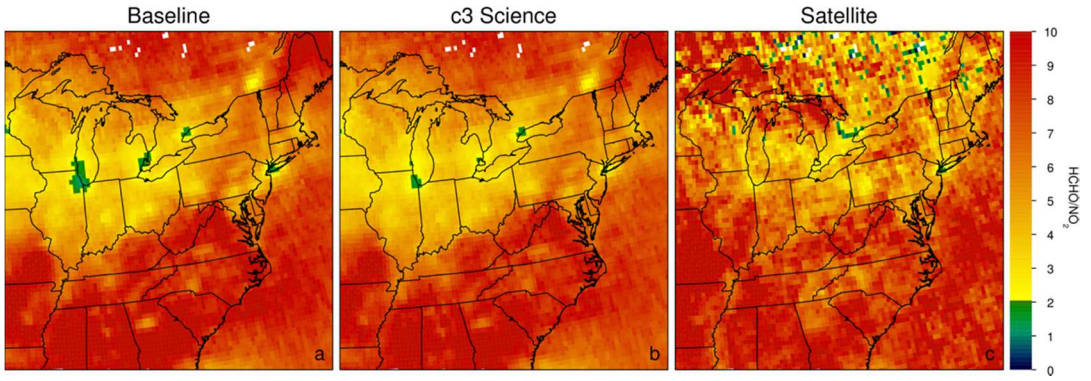

Figure 22: Ratio of average column HCHO to average tropospheric column NO_2 for (a) Baseline model, (b) c3 Science scenario, (c) OMI satellite data, over the model domain for JJA 2011. Only grid points with at least 10 days of satellite data for both HCHO and NO_2 retrievals are used. Model output for the two scenarios are convolved with appropriate OMI SAO (HCHO retrieval) and OMI GSFC (NO_2 retrieval) averaging kernels.

Figure 22 shows the average column HCHO/average tropospheric column NO_2 ratio (hereafter, HCHO/NO_2 ratio) from CMAQ output (Figure 22a and b) and satellite data (Figure 22c) for the modeling domain. According to *Duncan et al.* [2010], a HCHO/NO_2 ratio between 1 and 2 indicates the atmospheric column is transitioning between VOC-sensitive and NO_x-sensitive regimes. When the ratio is below 1, the atmosphere is considered to be VOC-sensitive, and when the ratio is above 2, the atmosphere is considered to be NO_x-sensitive. It is important to note that this analysis is for the *atmospheric column*, not the surface, therefore it may not be indicative of the surface photochemical O_3 production regime. This comparison does however provide insight into lower free troposphere composition, an important factor especially in the afternoon, for addressing air quality issues. Mixing of the Planetary Boundary Layer (PBL) with the free troposphere combines pollution transported from upwind sources with local pollution, changing the local atmospheric conditions. Understanding the upwind sources and composition of pollution are paramount to developing effective air quality regulations.

Figure 23 is the same as Figure 22, except it focuses on the New York metropolitan region. Figure 23a shows that for the baseline CMAQ model scenario, the air above New York City (NYC) and Eastern Long Island has a $HCHO/NO_2$ ratio between 1 and 2 (green boxes), indicating that the atmosphere is transitioning between the VOC and NO_x sensitive regimes [*Duncan et al.*, 2010]. In Figure 23b, the c3 Science model scenario (detailed in Table 2) shows the area downwind of NYC is mostly transitioned to a NO_x-sensitive atmosphere (yellow and orange boxes), leaving a smaller area over NYC within the transition zone. Figure 23c shows the average satellite $HCHO/NO_2$ ratio, indicating that some areas over NYC are within the transition zone while most of the area is within the NO_x-sensitive regime. Figure 23b shows too much of the NYC region as transitioned to NO_x-sensitive conditions, compared to the satellite ratio (Figure 23c). This is likely due to the 50% reduction of mobile NO_X emissions in the c3 Science model scenario. This reduction was applied domain wide, based on an empirical study that was completed for the Baltimore Washington region [*Anderson et al.*, 2014]. While the 50% reduction in mobile NO_X is a good approximation of the necessary emissions inventory adjustment, further modeling studies should adjust the mobile NO_x emissions inventory on a more localized scale, based on observational data throughout the model domain.

Figure 23d and e are scatter plots of the Baseline CMAQ $HCHO/NO_2$ ratio to the satellite $HCHO/NO_2$ ratio, and the c3 Science model $HCHO/NO_2$ ratio to the satellite $HCHO/NO_2$ ratio, respectively. Linear least squares fits to the data points, forced to go through the origin (0-intercept) are also shown. These comparisons

indicate that the c3 Science scenario is more closely representative of the observed atmosphere, as evidenced by the 0-intercept slope of 0.97 compared to the 0-intercept

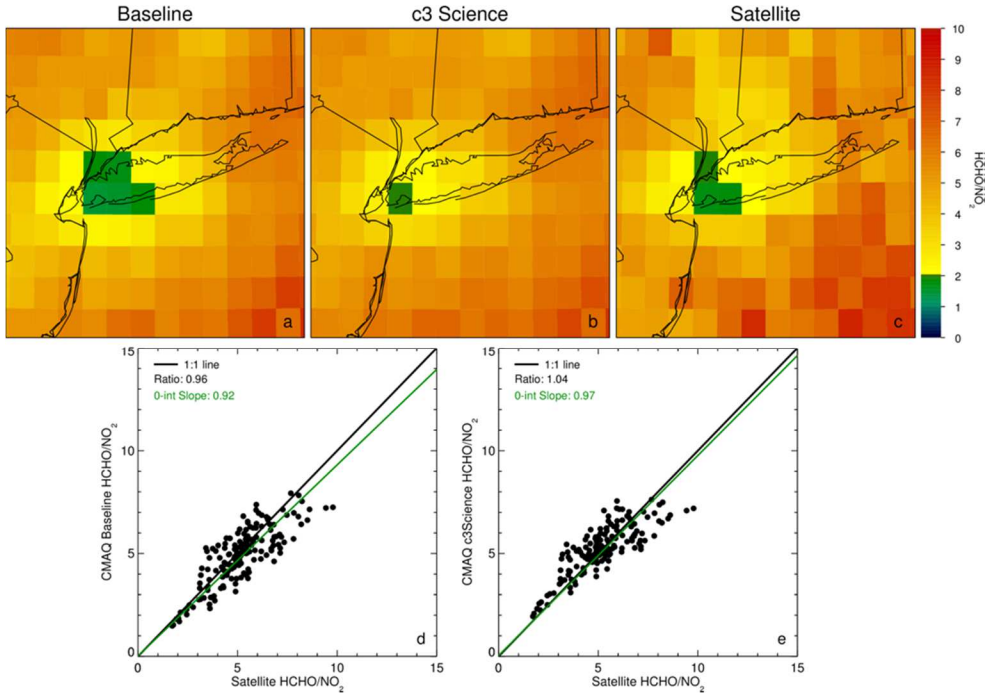

Figure 23: The top row is the same as Figure 22, except focusing on the NY metropolitan region. Scatter plots comparing the satellite derived $HCHO/NO_2$ ratio and the (d) Baseline scenario ratio, and (e) c3 Science scenario ratio are shown.

slope of 0.92 for the Baseline scenario. In Figure 23d and e, points below the 1 to 1 line indicate the model is producing a lower $HCHO/NO_2$ ratio than expected. This could mean there is too little HCHO, or too much NO_2 in the model column compared to the satellite retrieval. When the c3 Science model framework is used (Figure 23e), the number of points below the 1 to 1 line are reduced, especially for ratio values < 5. Since the model improvements mostly affect column NO_x concentrations, this suggests that the adjustments are improving the representation of NO_x within the model. Additionally, for the Chesapeake Bay region, both the baseline and c3 science model

frameworks are representative of observed satellite HCHO/NO_2 ratios (Figure 24), accurately representing the area as completely NO_x-sensitive.

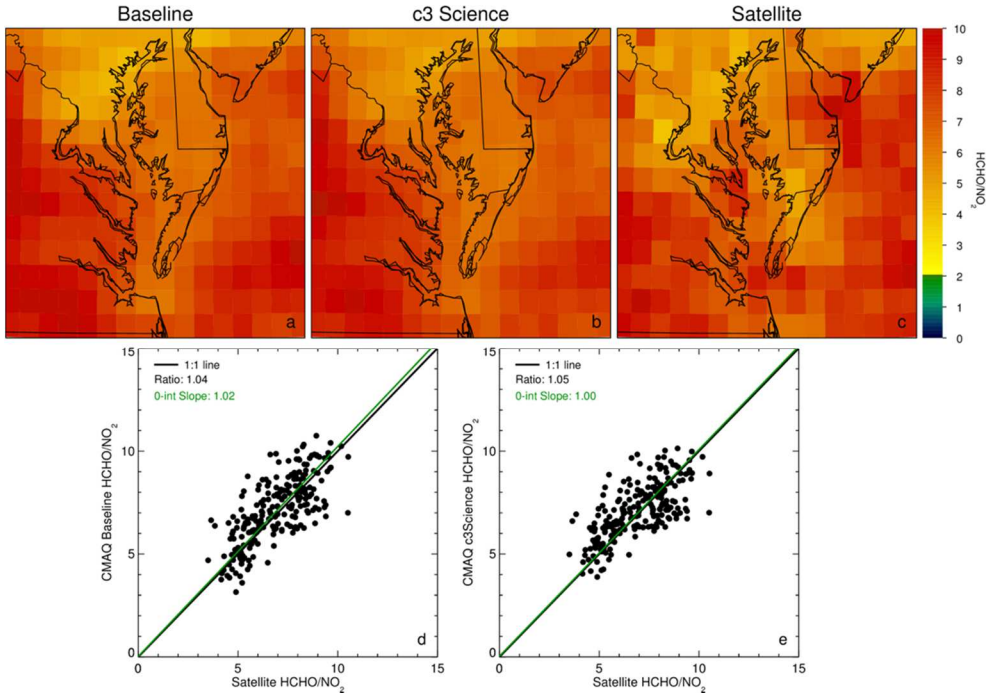

Figure 24: Same as Figure 22 except for the Chesapeake Bay region.

For some regions of the model domain, like the upper mid-west, both model simulations produce HCHO/NO_2 ratios that are lower than observed (see Figure 25 and Figure 26). In more rural regions, we see no improvement in the HCHO/NO_2 ratio between the two model scenarios, which could suggest the low ratios are due to HCHO. This is likely due to the CB05 chemical mechanism used by CMAQ. When the improved chemical mechanism CB6r2 is used [*Ruiz and Yarwood*, 2013], HCHO concentrations increase within the model, and are more consistent with measured values [*Goldberg et al.*, 2016]. Further improvements to the CB6r2 chemical mechanism, will increase HCHO concentrations within the model [*Marvin et al.*, 2017], and should improve model performance when compared to satellite observations. In the Chicago and Detroit metropolitan centers, we see increases in the HCHO/NO_2 ratio

when model improvements are applied (Figure 25 and Figure 26, respectively). This is expected as decreases of NO_x in urban centers would raise the $HCHO/NO_2$ ratio.

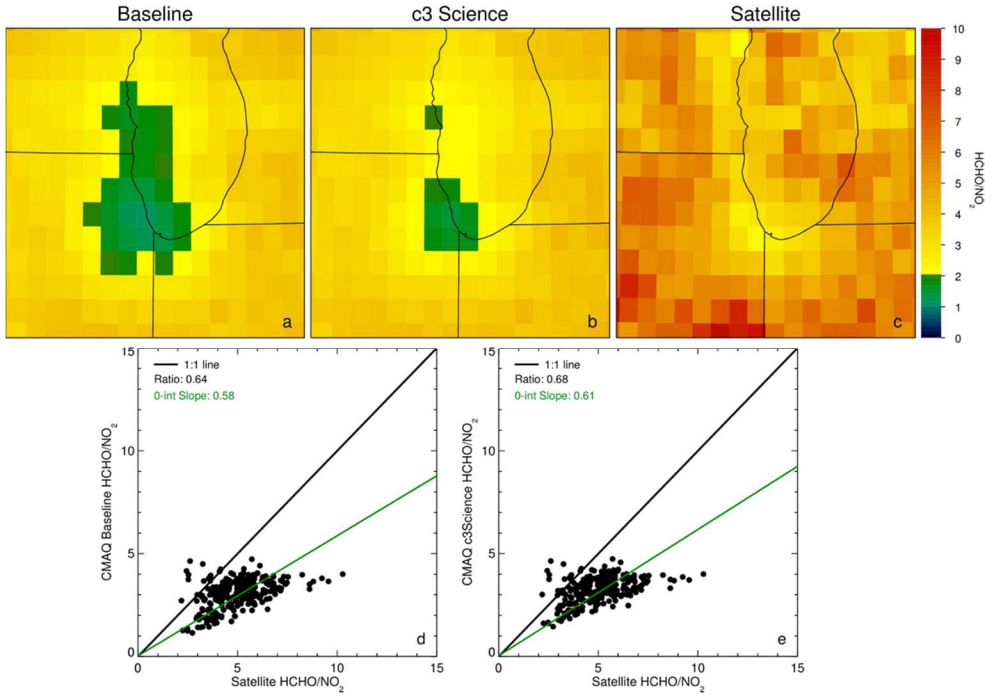

Figure 25: Same as Figure 22 except for the Chicago region.

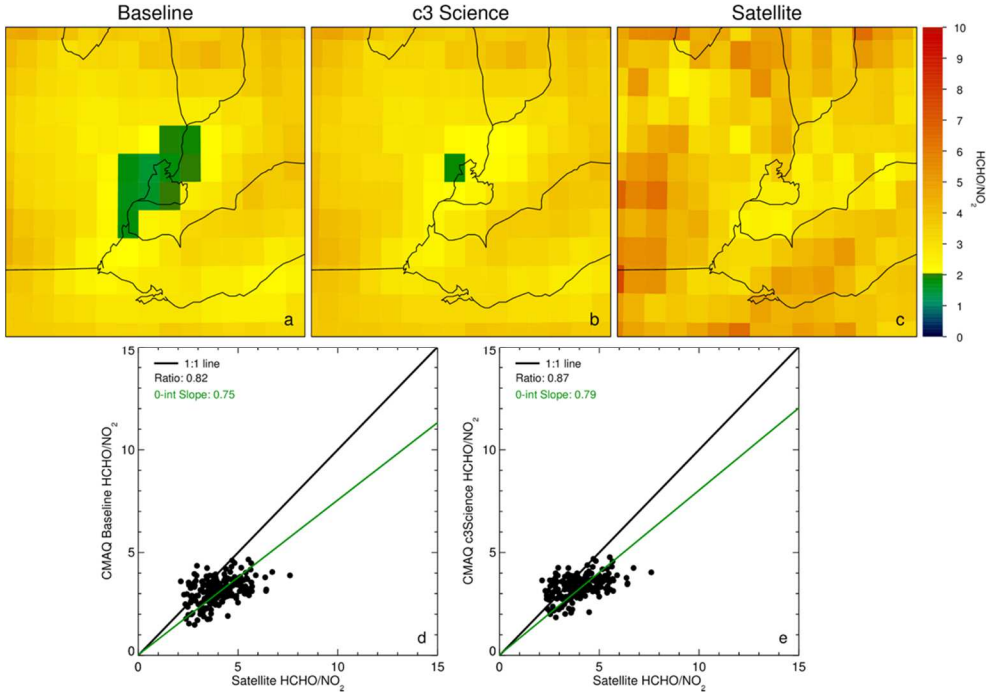

Figure 26: Same as Figure 22 except for the Detroit region.

Based on the satellite comparison, the c3 Science scenario more accurately represents the state of the 2011 atmosphere. While further improvements to HCHO and NO_x representation in rural regions within the model are necessary, the c3 Science scenario improves the representation of O_3 photochemistry in urban centers throughout the modeling domain, creating a more realistic model framework for guiding public policy [*Ring et al.*, 2018].

3.5: Modeling Scenarios for 2018

To assist state agencies in developing air quality attainment strategies, future emissions estimates are generated based on expected economic growth factors, fleet turnover, future air quality regulations, etc. Development of the future emissions inventory aids in providing guidance and justification for emissions standards reductions and proposed government legislation to improve air quality. We use the 2018 projected emissions to examine the efficacy of the c3 Science model scenario in 2018 compared to 2011, and to assess a future attainment strategy developed by the MDE, discussed in the next section.

All 2018 model scenarios discussed in this section use the same meteorology as the 2011 simulations, therefore, all differences in O_3 between 2011 and 2018 are due solely to emissions. $AM8O_3$ for the 2018 baseline simulation is shown in Figure 27a. Modeled surface O_3 in 2018 is notably lower than in 2011 (Figure 27a), indicative of the expected air quality improvements that are projected to occur by 2018. Values of $AM8O_3$ for the 2018 c3 Science simulation are shown in Figure 27b. Fewer model

grid points are plotted for the c3 Science scenario than in the Baseline scenario, because some grid points no longer satisfy the criteria of 10 days with maximum 8-hr O_3 above 60 ppb in the 2011 simulation. Elevated O_3 levels are still present in the Chesapeake Bay and Long Island Sound; however, these regions are smaller and have a reduced magnitude when compared to 2011.

A scatter plot of the $AM8O_3$ at the CMAQ grid points closest to the AQS monitoring sites for the Baseline and c3 Science model scenarios is shown in Figure 27c. Some grid points in NJ, CT, and NY for example, are above the 1 to 1 line, indicating surface $AM8O_3$ increases in the c3 Science model scenario relative to the Baseline simulation. Conversely, all points in MD, and some in NY, as well as CT lie below the 1 to 1 line, indicating a reduction of $AM8O_3$ in the c3 Science scenario relative to the Baseline scenario. Sites with the highest $AM8O_3$ shown in Figure 27c are listed in Table 3. Values in the last column are bolded for sites showing reductions of $AM8O_3$ between the two model scenarios.

Table 3: AQS sites with highest modeled $AM8O_3$ shown in Figure 27c.

AQS SITE	2018 BASELINE ($AM8O_3$ PPB)	2018 C3 SCIENCE ($AM8O_3$ PPB)	$\Delta AM8O_3$ (PPB)
Pfizer Lab, NY	148.0	146.0	**-2.0**
Greenwich Point, CT	144.2	141.4	**-2.8**
Queens College, NY	137.8	136.4	**-1.4**
White Plains, NY	133.8	131.3	**-2.5**
Babylon, NY	131.3	126.2	**-5.1**
Riverhead, NY	128.1	126.5	**-1.6**
Essex, MD	130.1	116.5	**-13.6**
Furley, MD	128.8	116.5	**-12.3**
Sherwood Island, CT	116.2	122.3	6.1
New Haven, CT	114.9	116.8	1.9
Fort Griswold Park, CT	111.9	113.9	2.0
Edgewood, MD	117.7	108.0	**-9.7**

When comparing AM8O_3 for Baseline and c3 Science scenarios, it is important to remember there are three major modeling framework changes that comprise the c3 Science scenario, as described in Table 2. Decreasing the lifetime of NTR contributes to the domain wide increase (red color) shown in the Figure 27d. Since 2018 emissions are scaled based on 2011 emissions, the 50% reduction of on-road mobile NO_x emissions in 2018 is also necessary. This reduction is less effective in 2018 because the on-road mobile emissions are projected to be cleaner due to national regulations, engine turnover, new fuel requirements, and local control programs despite a projected increase in vehicle miles traveled [*McDill et al.*, 2015]. Essentially, further controls of on-road mobile emissions will be less effective because this NO_x source sector has already been significantly reduced. Large reductions of surface O_3 within the Chesapeake Bay and increases in the coastal NY metropolitan area are shown in Figure 27d. These are due to the c3 Marine emissions inventory adjustments.

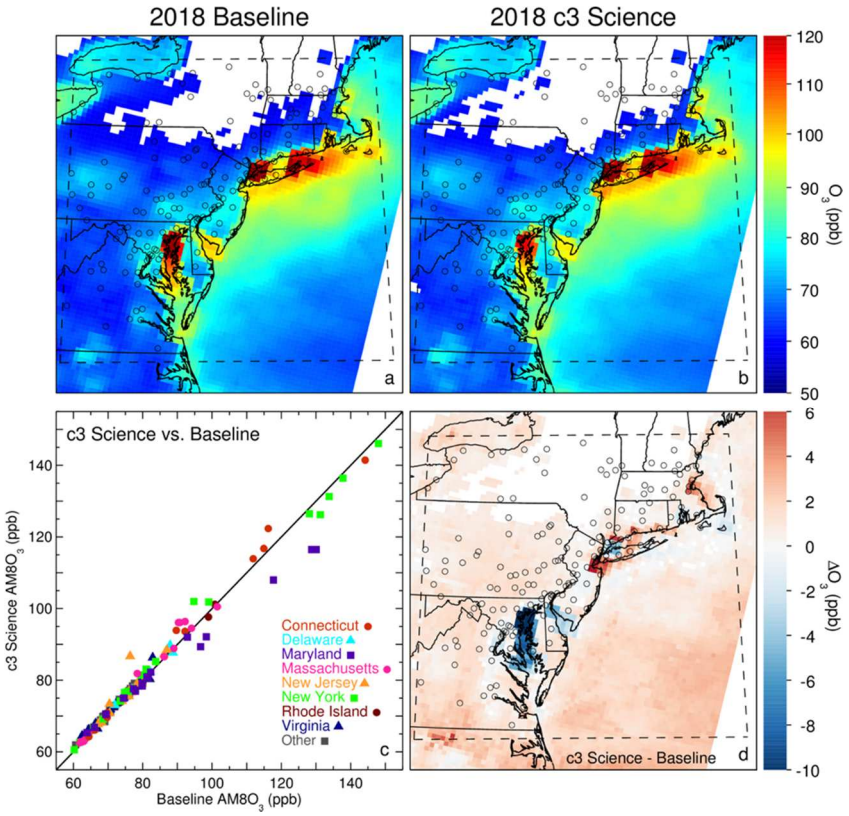

Figure 27: $AM8O_3$ for JJA 2018 for (a) Baseline and (b) c3 Science model scenarios. (c) A scatter plot of $AM8O_3$ for model grid points closest to the AQS sites for the Baseline vs. c3 Science scenarios. (d) A difference plot between c3 Science and Baseline model scenarios, highlighting $AM8O_3$ changes in the Chesapeake Bay and along the NYC metropolitan area coast.

As noted earlier, CMAQ produces extremely high values of modeled $AM8O_3$ (> 140 ppb) for some locations (Figure 27c). These high values are much larger than measured surface O_3 in 2011 and are therefore unrealistic. Nevertheless, model results at the six AQS sites with the highest $AM8O_3$ in 2018 show greater reductions of surface O_3 in the c3 Science scenario. This demonstrates the worst days for modeled surface O_3 in 2018 are more improved in the c3 Science model scenario when compared to the Baseline scenario.

We now return to the impact of c3 Marine emissions on NO_x and VOC limits of the photochemical O_3 production. $AM8O_3$ decreases of ~5-15 ppb are shown in

Figure 27d for grid points in the Chesapeake Bay region. Conversely, increases of ~2-6 ppb are shown for grid points in New York/New Jersey Harbor and Long Island Sound. We see regions of AM8O_3 decrease downwind of New York City, a different result from 2011 (Figure 27c). To further emphasize this point, Figure 28 highlights the impact of ship emissions on surface O_3 production along coastal regions within the 2011 and 2018 Science model framework (Table 2). In both Figure 28a and Figure 28b we see the expected decreases in AM8O_3 within the Chesapeake and Delaware Bay regions. In 2018 (Figure 28b), the AM8O_3 reductions are larger, showing more dramatic effects on surface O_3 production when large precursor sources (c3 Marine emissions) are lifted off the surface.

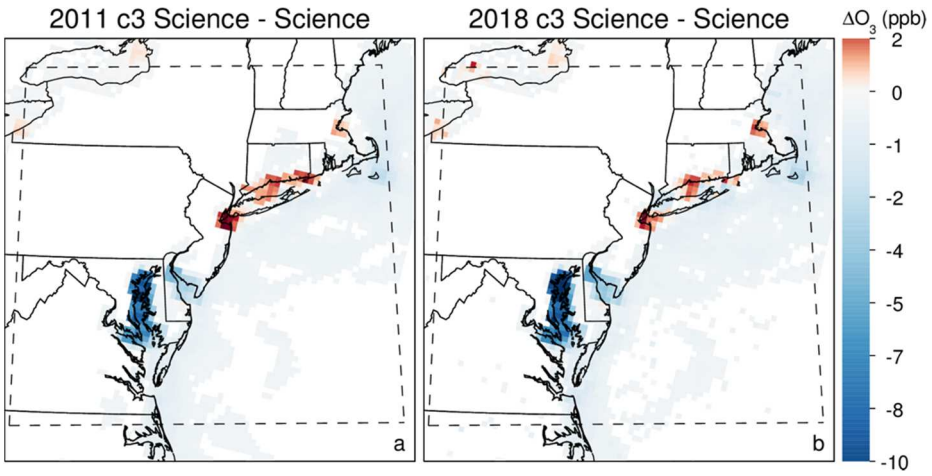

Figure 28: Difference plots of AM8O_3 between the c3 Science and Science modeling scenarios for (a) 2011 and (b) 2018. This highlights the effect of the c3Marine adjustment on surface O_3 production in the Science model framework.

Additionally, Figure 28a and b show smaller increases in AM8O_3 in the NJ/NY/CT area in 2018 than in 2011. Comparing Figure 28a and b highlights the reduction of AM8O_3 in the New York metropolitan area and along the Connecticut coast in 2018, perhaps showing parts of the region are transitioned and others have yet

to transition from a VOC to NO_x-sensitive region for photochemical O_3 production within the model.

3.6: Air Quality Attainment Strategy Analysis

State agencies use air quality models to quantify the effect of proposed legislation on future air quality. Here we examine one attainment strategy developed by MDE called "Scenario 4A". This approach assumes that in 2018, emissions from EGUs will be at the best observed rates between 2005 and 2012 using existing emissions control equipment. To examine the impact of this attainment strategy on reducing surface O_3 production, Figure 29 shows the effect of implementing scenario 4A regulations within the c3 Science model framework. Implementing the scenario 4A attainment strategy reduces $AM8O_3$ domain wide, with the largest reductions occurring in areas significantly affected by power plants.

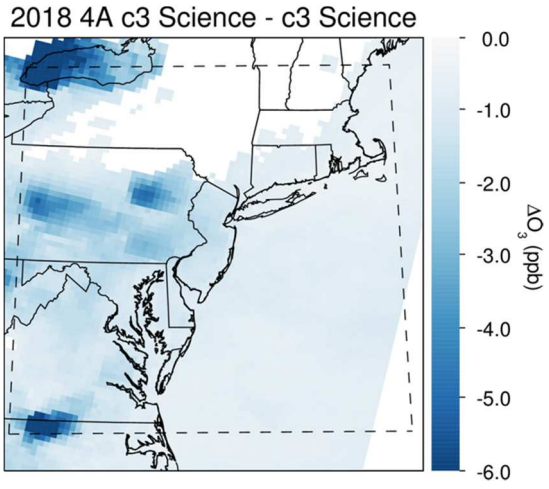

Figure 29: The difference of modeled $AM8O_3$ between c3 Science simulations both with and without the scenario 4A attainment strategy adjustments.

To quantify the $AM8O_3$ reduction in 2018 due to various scenario changes, we use Design Values (DV) as required by the EPA. An observed yearly design value is the 3-year running average of the observed fourth highest daily peak 8-hr average O_3

at an AQS site. The base design value (DVB) is a weighted average of yearly design values over a 5-year period [*Wayland*, 2014]. The second column of Table 4 provides 2011 DVBs for select AQS monitoring sites.

To assess attainment strategies for future years, a surface O_3 Relative Response Factor (RRF) is calculated. This metric represents the fractional change in modeled surface O_3 based on emissions changes between the base and future modeling scenarios [*Wayland*, 2014]. Figure 30 depicts a field of RRFs, showing geographic variation, for two model simulations used to calculate columns 5 (Figure 30a) and 6 (Figure 30b) in Table 4. For this analysis, the RRF is the $AM8O_3$ for 2018 divided by the $AM8O_3$ for 2011. The design value for the future model scenario (DVF) is the RRF multiplied by the DVB at each evaluated monitoring site. This value is compared to the NAAQS standards to determine whether the location of the monitoring site, in the simulated attainment strategy, is in attainment [*Wayland*, 2014].

Table 4: Observed and modeled design values calculated for several modeling scenarios at AQS sites in CT/NY/MD. Bolded values in last two columns show largest ΔDVF.

AIR QUALITY ATTAINMENT STRATEGY (SCENARIO 4A) ANALYSIS							
AQS Site	**DVB**	**DVF Baseline**	**DVF 4A Baseline**	**DVF c3 Science**	**DVF 4A c3 Science**	**ΔDVF 4A Base - Base**	**ΔDVF 4A c3 Science – c3 Science**
Greenwich Point, CT	80.3	76.37	76.12	71.54	71.15	-0.25	**-0.39**
Stratford Point, CT	84.3	77.30	76.76	76.53	75.98	-0.54	**-0.55**
Sherwood Island, CT	83.7	82.95	82.51	78.88	78.43	-0.44	**-0.45**
Hammonasset, CT	85.7	75.69	75.32	76.25	75.88	-0.37	-0.37
Pfizer Lab, NY	74.0	71.02	70.63	66.36	65.93	-0.39	**-0.43**
Queens College, NY	78.0	73.93	73.44	69.97	69.56	**-0.49**	-0.41
Babylon, NY	83.3	76.86	76.59	73.15	72.87	-0.27	**-0.28**
White Plains, NY	75.3	73.20	72.79	67.73	67.25	-0.41	**-0.48**
Davidsonville, MD	83.0	71.10	70.28	73.71	72.78	-0.82	**-0.93**
Padonia, MD	79.0	70.44	69.27	71.98	70.69	-1.17	**-1.29**

Essex, MD	80.7	73.24	72.85	72.24	71.73	-0.39	**-0.51**
Fair Hill, MD	83.0	73.78	72.64	75.97	74.62	-1.14	**-1.35**
Southern Maryland, MD	79.0	70.58	69.40	72.19	70.91	-1.18	**-1.28**
Fredrick Airport, MD	76.3	67.10	65.42	69.18	67.43	-1.68	**-1.75**
Edgewood, MD	90.0	82.02	81.47	82.41	81.67	-0.55	**-0.74**
Aldino, MD	79.3	70.14	69.41	72.22	71.34	-0.73	**-0.88**
Millington, MD	78.7	69.53	68.66	71.62	70.65	-0.87	**-0.97**
Rockville, MD	75.7	65.69	64.91	67.08	65.98	-0.78	**-1.10**
HU-Beltsville, MD	79.0	67.70	66.82	69.46	68.44	-0.88	**-1.02**
PG Equestrian Center, MD	82.3	70.52	69.64	72.85	71.84	-0.88	**-1.01**
Beltsville, MD	80.0	68.59	67.65	71.22	70.14	-0.94	**-1.08**

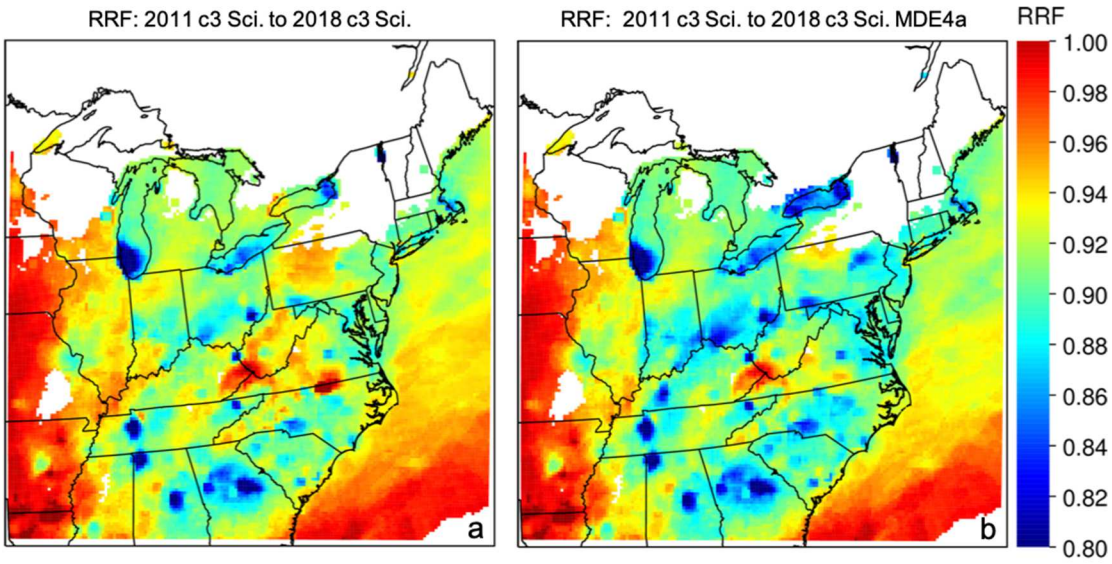

Figure 30: Contours of calculated Relative Response Factors (RRF) showing how surface O_3 is expected to change between 2011 and 2018 in the (a) c3 Science model framework, and (b) in the c3 Science model framework when the MDE4A attainment strategy is implemented for 2018. The blue colors indicate reductions of O_3, while the red indicate very little change, or an increase (dark red).

We have calculated DVs for four modeling scenarios. The scenarios are:

1. 2011 baseline to 2018 baseline
2. 2011 baseline to 2018 baseline with scenario 4A emissions reductions
3. 2011 c3 Science to 2018 c3 Science

4. 2011 c3 Science to 2018 c3 Science with scenario 4A emissions reductions

The DVs at selected AQS sites are shown in columns 3-6 of Table 4. Results shown in Table 4 indicate the effectiveness of the scenario 4A power plant emissions reductions in both the baseline and c3 Science model scenarios (columns 7 and 8). As expected, all DVs are negative in the two columns, meaning the 4A scenario is effective at reducing surface O_3 at all monitoring sites. Focusing on the italicized values in Table 4 columns 7 and 8 that denote the larger of the two differences for each site, we see scenario 4A emissions reductions are more effective at reducing surface O_3 in the c3 Science model scenario than in the Baseline scenario for almost all AQS locations. This result has significant relevance to the people responsible for developing air quality policy to control surface O_3. Improper representation of emissions from c3 Marine vessels in the CMAQ model framework underrepresents the impact of emission control scenarios in almost all near-coastal regions affected by shipping emissions [*Ring et al.*, 2018].

3.7: Conclusions

In this study, we examine the impact of Class 3 Commercial Marine Vessels (c3 Marine) emissions on air quality of coastal regions along the eastern US. Class 3 vessels are the largest within the global shipping fleet and have diesel engines with fuel displacement of at least 30 liters/cylinder. We have adjusted near-shore c3 Marine emissions to reflect a more realistic and consistent vertical distribution of pollutants. Model results that include the adjusted c3 Marine emissions show a decrease of AM8O_3

at Maryland AQS sites near the Chesapeake Bay, such as Essex, MD: ~6.5 ppb, where photochemical O_3 production is NO_x-sensitive. In areas such as Long Island Sound, the vertical distribution adjustment of marine emissions has increased $AM8O_3$ by ~3.5 ppb. This result, driven by a reduction of NO_x near the surface within the model, is due to the primary local production of O_3 being within the VOC-sensitive regime. Additionally, elevation of near-shore c3 Marine emissions off the surface allows the model to more accurately represent pollution dispersion and transportation associated with the c3 Marine emissions. This increases the lifetime of these chemical species within the model because they are no longer remaining near the emission source, over-producing O_3 in most regions and/or being removed from the atmosphere via wet or dry deposition [*Castellanos et al.*, 2011; *Castellanos et al.*, 2009]. Therefore, pollution transport from the Chesapeake Bay to the NY Metropolitan region could also contribute to increased surface O_3 production [*Ring et al.*, 2018].

Column HCHO and NO_2 retrievals from the Ozone Monitoring Instrument (OMI) are used to calculate $HCHO/NO_2$ ratios to determine the O_3 production regime in the atmospheric column above the surface for observations and model simulations. In the Baseline CMAQ model scenario, the $HCHO/NO_2$ ratio shows a larger area over the New York metropolitan area is transitioning from VOC-sensitive to NO_X- sensitive than is observed from the satellite. When empirically based model improvements are incorporated, known as the c3 Science scenario (see Table 2), a greater area over the New York metropolitan is NO_x- sensitive, improving model performance in relation to the observed satellite $HCHO/NO_2$ ratio and more accurately representing tropospheric conditions [*Ring et al.*, 2018].

We also examine the impact of these model improvements on future (2018) modeling scenarios. When comparing the 2018 Baseline to the c3 Science scenario, AM8O_3 reductions are larger for the Chesapeake Bay (Essex, MD: ~13.6 ppb), and smaller increases are shown for the New York metropolitan area than in 2011. Some regions around Long Island Sound show reductions in surface O_3, indicating the area has transitioned to NO_X- sensitive in the 2018 model simulation [*Ring et al.*, 2018].

Analysis of a NAAQS attainment strategy developed by MDE that simulates EGUs operating with optimal emissions rates shows that the strategy is more effective within the c3 Science scenario. Simulations using this improved model framework predict greater decreases in surface O_3, indicating legislation aimed at limiting O_3 precursors should be more effective than is demonstrated by the Baseline CMAQ model simulation [*Ring et al.*, 2018].

Chapter 4: Anthropogenic VOCs in the Long Island Sound, NY Airshed and their Role in Ozone Production (Ring et al. in prep)

4.1: Introduction

Over the past few decades, maximum tropospheric O_3 concentrations in the US have decreased [*Bloomer et al.*, 2009; *Goldberg et al.*, 2015; *Simon et al.*, 2015] coinciding with anthropogenic emissions reductions, however low-level O_3 or background O_3 concentrations have increased [*Cooper et al.*, 2012; *Goldberg et al.*, 2015; *Parrish et al.*, 2009; *Simon et al.*, 2015]. The study by *Simon et al.* [2015] suggests the observed trend of decreasing difference between the lowest and highest O_3 concentrations may be a result of US environmental policy. Regulations targeting anthropogenic NO_x have significantly reduced emissions as reflected in the NEIs. This emission reduction has contributed to the decreasing maximum tropospheric O_3 trend [*Simon et al.*, 2015]. Conversely, reported VOC emissions have remained relatively stagnant or increased in some regions of the US, and may explain the observed rise in background tropospheric O_3 [*Simon et al.*, 2015]. To address the converging trends and reduce background tropospheric O_3 levels, control strategies targeting other O_3 precursors like VOCs may be necessary [*Simon et al.*, 2015].

Many studies have observed high concentrations of tropospheric O_3 over near-coastal bodies of water [*Cleary et al.*, 2015; *Goldberg et al.*, 2014; *Hastie et al.*, 1999]. The small-scale on-shore winds known as bay-breezes or lake-breezes move polluted air over coastal land and cities [*Loughner et al.*, 2011; *Loughner et al.*, 2014; *Mazzuca et al.*, 2017; *Sillman et al.*, 1993; *Stauffer et al.*, 2015] impacting air quality in the coastal regions. Higher resolution modeling of the coastal marine boundary layer would

improve representation of these impactful circulation events [*Angevine et al.*, 2006; *Sillman et al.*, 1993] in air quality models, and better inform air quality policy.

The entire state of Connecticut (CT) is currently designated as non-attainment for the NAAQS O_3 standard (Figure 4) [*EPA*, 2018a; b] and is located downwind from New York City (NYC), a significant source of anthropogenic emissions. Connecticut also receives on-shore atmospheric circulation from the heavily trafficked Long Island Sound (LIS) as shown in Figure 34. In order to develop effective air quality attainment strategies, model and observational studies are needed to identify the meteorological conditions and emission sources directly contributing to the poor air quality in CT. Three research flights discussed in this chapter were conducted over the LIS and CT on May 17 and 18, 2017 and provide measurements of various atmospheric species during an O_3 exceedance event.

The estimated VOC/NO_x ratio derived from data and model comparison provides information about the atmospheric conditions favorable for O_3 production and the emissions adjustments and regulation that are necessary to improve air quality. To analyze the O_3 production VOC/NO_x ratio, *Duncan et al.* [2010] used a photochemical box model to calculate HCHO/NO_2 ratio for the Los Angeles, CA basin from modeled tropospheric columns. The geographic distribution of the model ratio field was compared to the HCHO/NO_2 ratio calculated using corresponding OMI tropospheric column observations. Satellite comparison of the OMI tropospheric column HCHO and NO_2 performed for the CONUS showed HCHO/NO_2 ratio values in major cities (including New York) within the 1-2 range. *Duncan et al.* [2010] cautioned that this

analysis (only based on modeling in the LA basin) may not be representative of regime transitions across the US.

Recently, *Schroeder et al.* [2017] performed box model simulations constrained to DISCOVER-AQ data for the Baltimore-Washington (BW) (2011), Houston (2013) and Colorado (2014) campaigns. They found a chemical transition point calculated with near-surface *in situ* data from the Colorado campaign to be 0.35 and a transition range of 0.9-1.8 when calculated with column profiles of HCHO and NO_2. They believe this discrepancy is due to the vertical distribution of HCHO in the lower free troposphere compared to NO_2 (Figure 31). Partitioning between NO and NO_2 favors NO at lower temperatures, so NO_2 concentrations decrease faster with altitude than HCHO [*Schroeder et al.*, 2017]. Evidence for regional variation in the transition region was found when HCHO/NO_2 calculations were performed using vertical column densities for Houston and BW regions [*Schroeder et al.*, 2017].

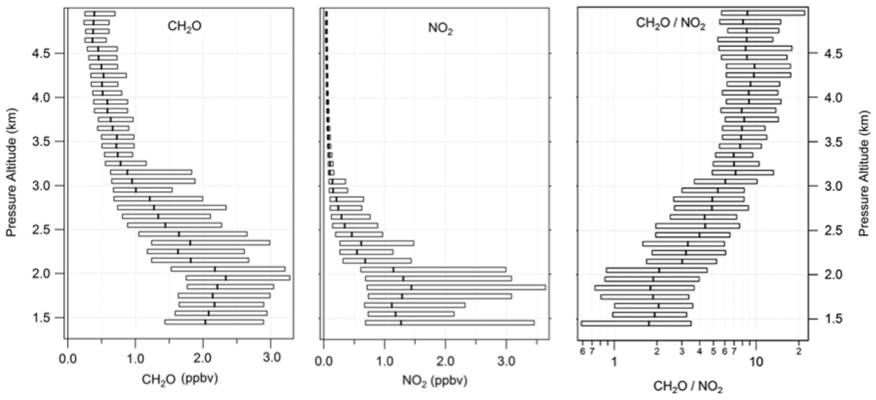

Figure 31: Colorado DISCOVER-AQ (a) HCHO data, (b) NO_2 data and the (c) ratio HCHO/NO_2 binned every 100m. The 25th and 75th percentiles are shown for each bin. (Figure 8 from [*Schroeder et al.*, 2017]).

The binned concentrations of HCHO (CH_2O) and NO_2 as a function of height in Figure 31 depict possible limitations of using a tropospheric column product, like

the OMI satellite retrievals, to calculate the $HCHO/NO_2$ ratio. Tropospheric column satellite products and the global models used to calculate the *a priori* profiles may have difficulty representing the vertical structure of HCHO and NO_2 in the PBL [*Schroeder et al.*, 2017]. Therefore, use of these products to drive surface air quality policy legislation may not be adequate.

To develop effective air quality control policies, it is necessary to examine the relative contribution of individual VOCs to photochemical O_3 production [*Avery*, 2006; *Carter*, 1994; *Jenkin et al.*, 2017; *Kamal et al.*, 2016; *Zaveri et al.*, 2003]. A metric known as the Maximum Incremental Reactivity (MIR) represents the relative importance of individual VOCs to surface O_3 production [*Carter*, 1994; 2010b]. The MIR scale is calculated from photochemical box-modeling scenarios where the VOC/NO_x ratio is VOC-sensitive, meaning VOCs have the maximum impact on O_3 production [*Carter*, 1994]. To calculate MIR, *Carter* [1994] performed two model simulations: the baseline VOC-sensitive simulation, and one with added VOC concentrations that produce an increase of O_3 that follows along a linear trend [*Carter*, 1994]. The difference in produced O_3 between the two simulations, divided by the amount of added VOC, yields the MIR (O_3 produced / g of VOC) [*Carter*, 1994]. This metric is a useful tool to quantify the O_3 produced from specific VOC species and therefore emission sources. The MIR values were developed for use in the Statewide Air Pollution Research Center (SAPRC) chemical mechanism [*Carter*, 1994]. Based on guidance from *Carter* [2010a], the California Air Resources Board instituted controls on VOC emissions according to their associated MIR value, focusing air quality mitigation efforts on the VOCs that produce the most O_3 [*Carter*, 2010b].

A similar metric to the MIR called the Photochemical Ozone Creation Potential (POCP) is used in the Master Chemical Mechanism (MCM) [*Carter*, 2010a; *Jenkin et al.*, 2017]. The POCP equation from *Jenkin et al.* [2017] is as follows:

$$POCP_{VOC} = \frac{(O_{3_{VOC}} - O_{3_{base}})}{(O_{3_{ethene}} - O_{3_{base}})} \times 100. \quad (34)$$

In Equation (34), the change in O_3 due to the addition of the test VOC is divided by the change in O_3 when a reference VOC (ethene in this case) is added. Equal masses of the ethene and test VOC are added to the respective model simulations and the resulting relative change in O_3 is calculated [*Jenkin et al.*, 2017]. Both metrics are quite useful for describing the test VOC's capability of producing O_3.

In this chapter we use the RAMMPP aircraft data and CMAQ model simulations to examine the importance of VOCs in the LIS region to O_3 production. Analysis of *in situ* VOC data provides policy-relevant information about VOC concentration and potential contribution to O_3 production for a LIS case study. Evaluation of RAMMPP with DISCOVER-AQ 2011 data from the Baltimore-Washington region shows general agreement concerning concentration and atmospheric profile of isoprene, NO_2 and O_3, but important differences are found. Evidence for long range transport of SO_2 and O_3 into the LIS is presented. Forecast CMAQ simulations for the LIS O_3 episode are compared to measured data to highlight model successes and limitations and provide possible reasons for missed O_3 forecasts. Finally, analysis of the largest contributing model inventory sector to the modeled surface O_3 in the LIS are performed. This study focuses on those emissions sources and VOC species most important to the photochemical production of O_3 in the LIS.

4.2: DISCOVER-AQ 2011: Baltimore-Washington Campaign

For this analysis we compare O_3, NO_2, and isoprene collected in 2017 over the Long Island Sound from RAMMPP flights to measurements collected during the July 2011 NASA air quality campaign: Deriving Information on Surface Conditions from COlumn and VERtically resolved observations relevant to Air Quality (DISCOVER-AQ) conducted in the Baltimore-Washington (BW) region. All three species were measured onboard NASA's P-3B aircraft (https://discover-aq.larc.nasa.gov/instruments.html) during DISCOVER-AQ. The P-3B flight paths for the entire campaign are shown in Figure 32.

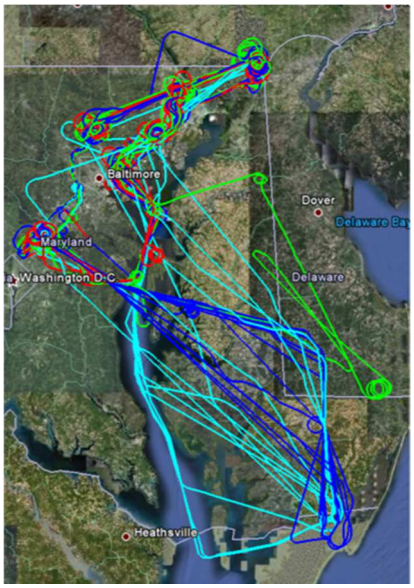

Figure 32: All of the flights for NASA's P-3B aircraft are shown. Flights were conducted from July 1st to July 29th, 2011 during the DISCOVER-AQ campaign. Spirals over designated areas were conducted to measure atmospheric profiles of various pollutants. (Figure is from https://www-air.larc.nasa.gov/missions/discover-aq/discover-aq.html)

Isoprene was measured by Armin Wisthaler's group from the University of Innsbruck with a Proton-Transfer-Reaction Mass Spectrometer. The abundance of NO_2 was measured using two instruments: the Thermal Dissociation-Laser Induced Fluorescence (TD-LIF) by Ronald Cohen's group from the University of California – Berkley, and the National Center for Atmospheric Research (NCAR) 4-channel

Chemiluminescence Instrument by Andrew Weinheimer's group. O_3 was also measured using the 4-channel Chemiluminescence Instrument by Andrew Weinheimer's group. All data were quality controlled and are publicly available at https://www-air.larc.nasa.gov/cgi-bin/ArcView/discover-aq.dc-2011.

4.3: VOC Can Analysis

As described in Section 1.4.3, aircraft flights were conducted over the Long Island Sound on May 17 and May 18 of 2017. A total of 35 canisters (hereafter called "cans") of air samples were collected during the three research flights and 50 VOCs were measured in each can. To correct for any contamination from the can interior or sample inlets, two reference or blank cans were collected during the sample period. All VOC data were corrected by first calculating the average reference can concentration for each VOC species. This value was then subtracted from the measured VOC concentration in each sample can.

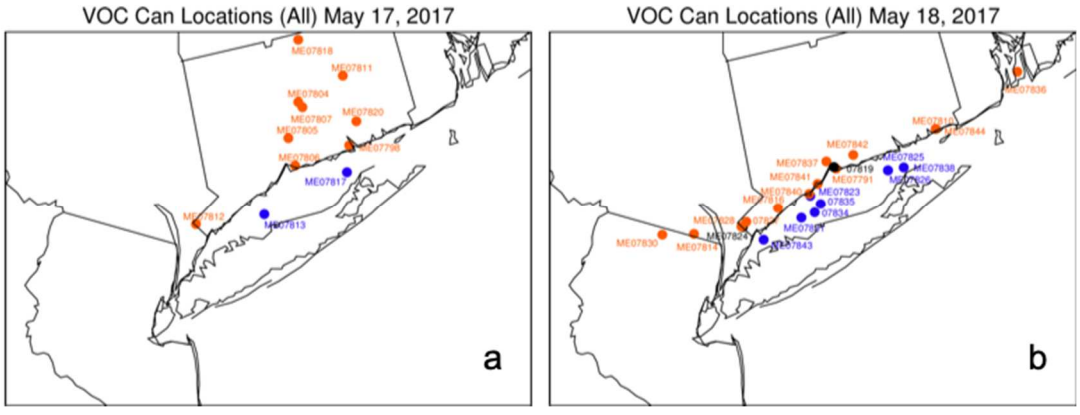

Figure 33: Geographic distribution of all VOC cans on (a) May 17, 2017 and (b) May 18, 2017. Cans were collected in flight and at various altitudes. Color distinctions represent cans collected over land (orange) and cans collected over water (blue). Cans with black colors overlap with other cans – color distinction purely for readability.

Figure 33 shows the spatial distribution of the cans collected on the two flight days. Most cans collected on May 18 were over the LIS or collected when flying along the CT shore of the LIS, sampling air downwind of New York City. Surface winds were westerly to south-westerly moving the New York City pollution plume over the LIS and CT (Figure 34).

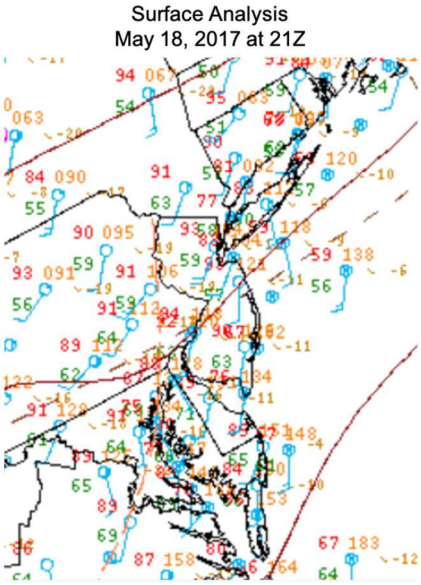

Figure 34: Surface observations of temperature, dew point, sky cover, sea-level pressure, pressure trend, wind speed and wind direction for the Long Island Sound region on May 18, 2017 (21Z).

(Image taken from the NOAA website: https://www.wpc.ncep.noaa.gov/html/sfc-zoom.php)

4.3.1: Reactivity with OH

Reaction of VOCs with OH initiates a series of chemical reactions that lead to photochemical production of O_3 and production of oxidants [*Kansal*, 2009]. Reaction rates of VOCs with OH (k_{OH}) are the primary factors for determining individual contributions of various VOCs, and therefore importance to O_3 formation [*Carter*, 1994; *Kansal*, 2009].

All 50 VOC species measured by the RAMMPP aircraft are ranked by their reaction with OH ($k_{OH} \times [VOC]$ (s^{-1})) to show the most important VOCs to O_3 formation in the LIS. The 12 VOCs with the highest ($k_{OH} \times [VOC]$ (s^{-1})) values are

shown ranked by median (Figure 35a) and ranked by average (Figure 35b). The reaction rate constants used for this analysis are included in Appendix A.

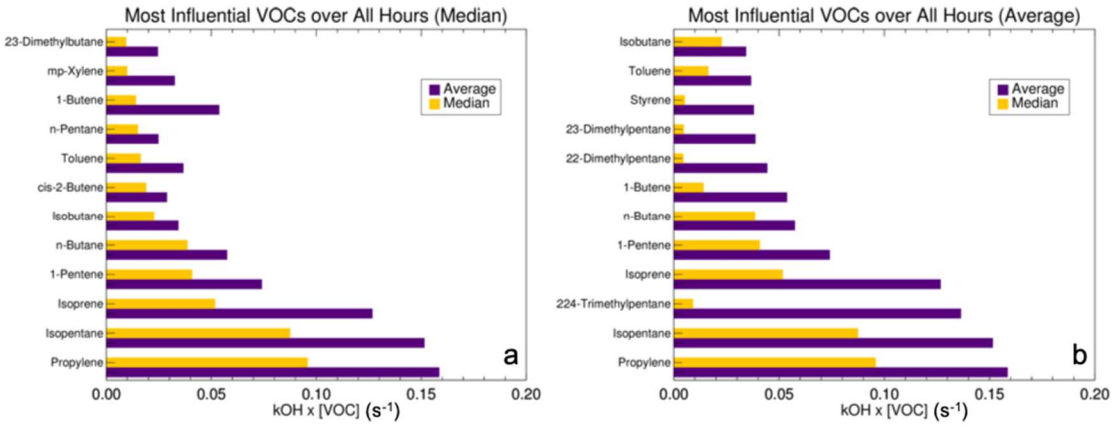

Figure 35: VOCs ranked by their reactivity with OH. Sorted by (a) median (gold bars) and by (b) average (purple bars).

Regardless of the sorting technique, propylene and isopentane are the two most influential VOCs in the LIS measured during the RAMMPP campaign. Isoprene is the 3rd most important VOC when ranked by the median, and the 4th when ranked by the average. One VOC canister contained concentrations of ~20 ppb for 224-trimethylpentane, explaining the large average $k_{OH} \times [VOC]$ value but relatively small median.

When sorting by time of day, it becomes clear that the reactivity of anthropogenic VOCs dominates biogenic isoprene in the morning (Figure 36a). Eight species rank higher than isoprene in Figure 36a compared to only two species in Figure 36b. This shows that morning VOC emissions may be contributing to the high afternoon O_3 concentrations in the LIS and downwind areas. Controlling the emission of anthropogenic VOCs, especially in the morning, may reduce the maximum O_3 concentrations reached in the afternoon. For example, propylene has a MIR value of

11.66 compared to 10.61 for isoprene [*Carter*, 2010b], and therefore could be responsible for significant amounts of tropospheric O_3 in the LIS. Many of the VOCs measured during the research flights (RFs) have large MIR values and therefore significant O_3 formation potential (Appendix A). Further analysis is necessary to determine the impact of these VOC emissions on surface air quality.

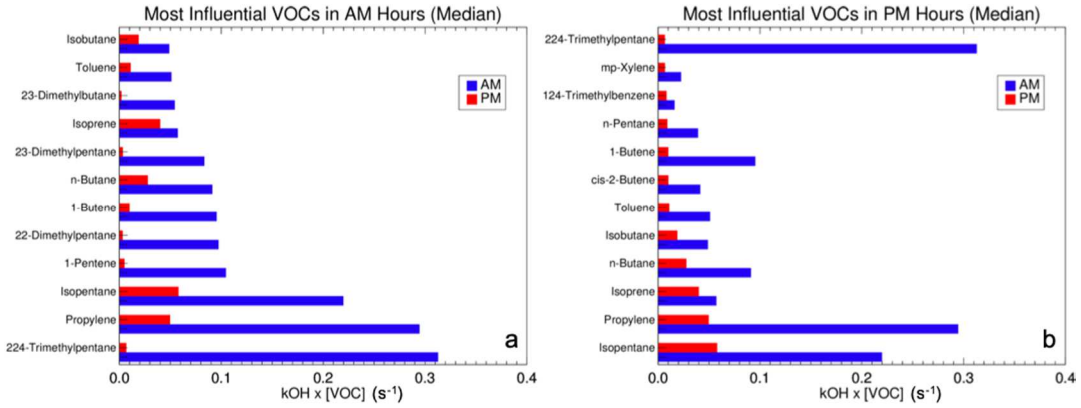

Figure 36: VOCs ranked by their reactivity with OH. Sorted by median values for cans collected during (a) AM (blue bars) and (b) PM (red bars) hours.

The lifetime of propylene is ~5 hours [*Atkinson*, 2000]. It is mainly emitted from petrochemical manufacturing facilities and diesel exhaust [*Buzcu and Fraser*, 2006; *Hocking*, 2005; *Liu et al.*, 2008]. Isopentane has a longer lifetime of ~1 day and is mainly emitted from gasoline vapors and engine exhaust emissions [*Buzcu and Fraser*, 2006; *Liu et al.*, 2008]. The compound 224-trimethylpentane has a lifetime of ~3 days with respect to reaction with OH [*Atkinson*, 2000] and sources mostly from industrial activity [*Buzcu and Fraser*, 2006]. Comparatively, isoprene (biogenic) has an atmospheric lifetime of ~1-2 hours [*Atkinson*, 2000].

In Figure 37, the OH reactivity of all measured species from the canisters are calculated and sorted for each VOC. The cans with reactivity values in the highest 10%

of the distribution are averaged and the cans with reactivity values in the middle 20% are averaged for each VOC species. The average reactivity values for each VOC in the highest 10% and middle 20% are grouped into their representative categories shown in Figure 37. This shows the relative importance of the various VOC groups to O_3 production in the NYC/LIS region. The values reported in Figure 37 are in relative agreement with the *Kleinman et al.* [2005] values, however more VOCs are present in the RAMMPP observations than in observations collected by *Kleinman et al.* [2005] in 1996. The large reactivity for the alkane group is because 26 alkanes were measured (over half of all VOCs), and isopentane is prominent in the VOC observations.

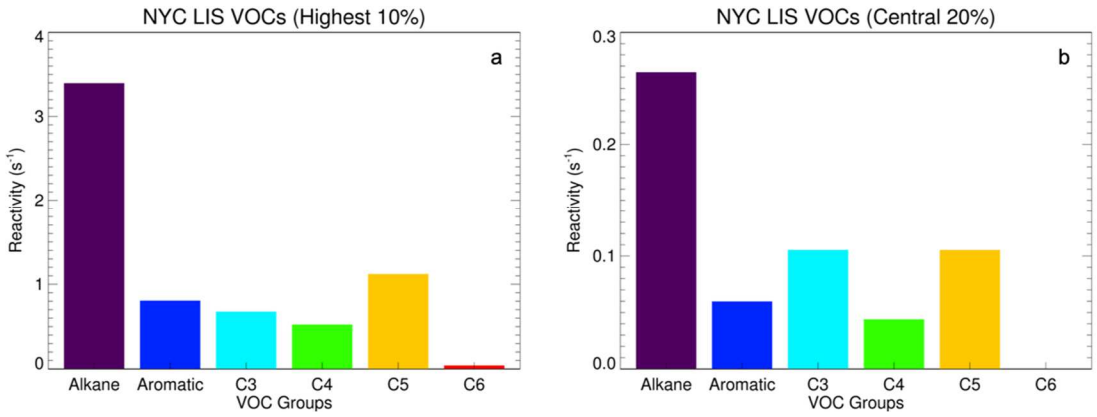

Figure 37: OH-VOC reactivity for the categories of hydrocarbons for the (a) top 10% of measurements and the (b) middle 20% of measurements for all VOCs measured throughout the RAMMPP 2017 flight campaign. Analysis is based upon Figure 12 from *Kleinman et al.* [2005].

In recent personal communication with Joel Dreessen from the Maryland Department of the Environment (MDE), we discovered that high concentrations of isopentane associated with high levels of O_3 are observed in the Chesapeake Bay. The winds carrying these polluted air masses generally come from the south, directly over

the Bay. The sources for the VOC-polluted air are not immediately known at this time. A forthcoming collaboration with Joel Dreessen and MDE will address these findings.

These results provide evidence that anthropogenic VOCs are playing a more important role in O_3 production in this region than was expected. However, given the sample size and short duration (2-days) of these flights, further observations are needed to confirm this result. Continued monitoring of NO_x, O_3, and VOCs in the LIS would improve confidence in the conclusion that emission controls targeting the most important anthropogenically produced VOCs would improve air quality in the LIS/CT region.

In a study by *Sillman et al.* [1993], model simulations incorporating a combination of polluted air, stagnant meteorology (usually associated with high pressure systems) and suppressed PBL height, indicate near-surface air over large bodies of water like the LIS or Lake Michigan (downwind from Chicago) is VOC-sensitive. It is likely that air aloft in the vertical column, over the LIS, is decoupled from the terrestrial biosphere and therefore low in isoprene concentrations due to the short lifetime ($\tau = \sim$1-2 hours) [*Sillman et al.*, 2002]. Surface measurements of VOCs and NO_x may not explain the photochemical O_3 production regime conditions aloft (500 to 1000 m) [*Sillman*, 1999], therefore measurement of the urban plume from aircraft in subsequent campaigns would provide valuable information about the photochemical O_3 production regime downwind from NYC. This has important implications for states downwind as vertical mixing of the boundary layer can bring O_3 produced in VOC-sensitive conditions down to the surface [*Sillman*, 1999; 2002; *Sillman et al.*, 1993].

4.4: Evaluating RAMMPP and DISCOVER-AQ measurements

We compare RAMMPP and DISCOVER-AQ data to examine the average atmospheric profiles for O_3, NO_2, and isoprene for the duration of the respective flight campaigns. In the analysis from Chapter 3, we determine that in the CMAQ model framework the BW region and the LIS region are controlled by two different photochemical O_3 production regimes, evidenced by the behavior of surface O_3 (Figure 28). Despite measurement collection during different years, and in different locations, comparison of the data is valuable. We see notable differences in the vertical profile of isoprene (Figure 38a), similarities with NO_2 (Figure 38b) and differences again with O_3 (Figure 38c). Measurements of isoprene detected in the RAMMPP canisters collected over the LIS are much smaller than DISCOVER-AQ measurements collected over the BW region.

There is more NO_2 in the sampled atmospheric column over the LIS during the RAMMPP campaign than in the BW region during July, but measurements follow a similar profile trend reaching minimum mixing ratios by the 3000 to 3500 m height bin (Figure 38).

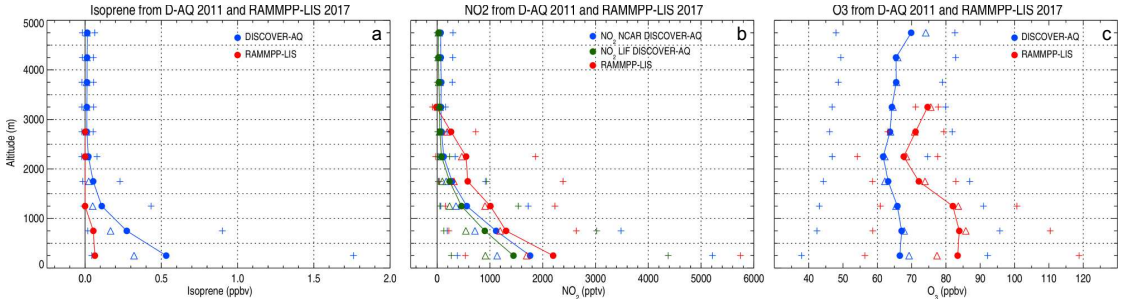

Figure 38: Comparisons between DISCOVER-AQ measurements from the P-3B in 2011 and RAMMPP measurements from the Cessna in 2017. Panel (a) shows the vertical distribution of Isoprene binned every 500 m over the entire sampling period, (b) shows the vertical distribution of NO_2 and (c) shows

the vertical distribution of O_3. The triangles represent the 50th percentile, the plus signs represent the 5th and 95th percentiles, and the solid circles represent the average for each binned layer.

Figure 39 shows the vertical distribution of the 12 most influential VOCs from Figure 35b binned every 500 m. Average concentrations of these anthropogenic VOCs are generally larger in each altitude bin than isoprene.

Based on the NO_2 shown in Figure 38b and VOC concentrations shown in Figure 39, it is possible that VOC-sensitive conditions near the surface and aloft could be responsible for some of the O_3 produced over the LIS. The increasing concentrations of O_3 aloft could also indicate a possible up-wind source of pollution advected into the LIS region. More discussion of this will follow in the next section.

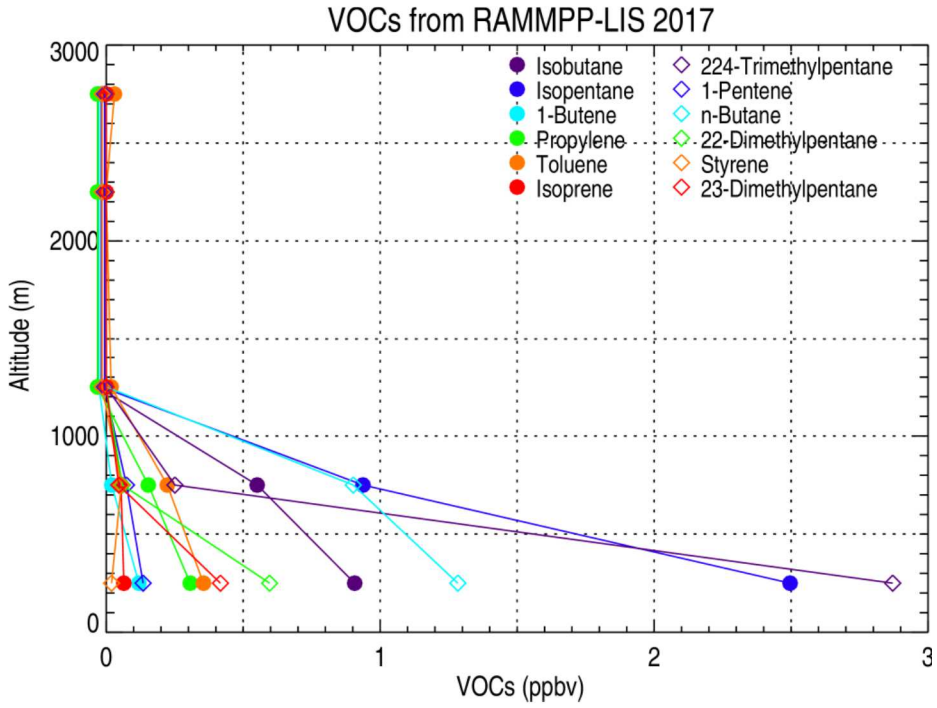

Figure 39: The vertical distribution of the 12 most influential VOCs binned every 500 m over the LIS sampling period. Each symbol represents the average for the binned layer.

4.5: Long-Range Transport

The long-range transport of O_3 and O_3 precursors into the Mid-Atlantic and Northeast regions of the US has long been an area of active research [*Altshuiler*, 1976; *Angevine et al.*, 2006; *Bergin et al.*, 2007; *Cleveland and Graedel*, 1979; *Endlich et al.*, 1984; *Frost et al.*, 2006; *He et al.*, 2016b; *McDonald-Buller et al.*, 2016; *Ryan et al.*, 1998; *Stehr et al.*, 2000; *Taubman et al.*, 2006; *Vukovich*, 1994; *Wolff et al.*, 1977]. Pollution transport from upwind sources bring air parcels with elevated O_3 in the lower free troposphere into the Northeast US and can contribute to local surface O_3 exceedance events if mixed into the planetary boundary layer [*Bergin et al.*, 2007; *Cleveland and Graedel*, 1979; *Frost et al.*, 2006; *He et al.*, 2016b; *Lippmann*, 1989; *McDonald-Buller et al.*, 2016; *Ryan et al.*, 1998]. As shown in Figure 40a, high O_3 levels were measured throughout the atmospheric column, with a minimum in the 2000 to 2500 m bin. In Figure 40b, we see low surface SO_2 concentrations that steadily increase with height, until the highest bin (3000 to 3500 m) where the average SO_2 concentration nearly doubles. Temperature for the aircraft profile that measured the highest SO_2 during RF3 is shown in Figure 40c. A temperature inversion, a common feature associated with pollution events [*Moghani et al.*, 2018; *Ryan et al.*, 1998], can be seen at about 2500m which can keep air aloft of the inversion from mixing with the air below meaning the O_3 above the inversion is likely not from local sources. The combination of the O_3, SO_2 and temperature profiles in Figure 40 indicates O_3 and SO_2 from an upwind source (or sources) has been transported into the LIS region.

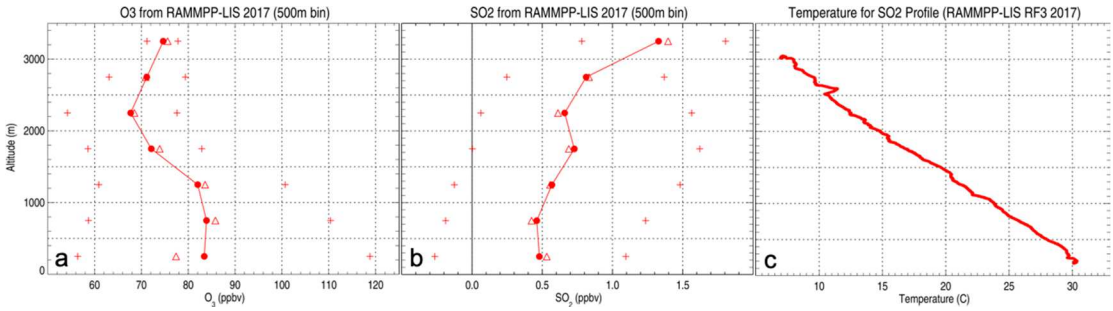

Figure 40: O_3 and SO_2 concentrations from all 3 research flights during the period binned every 500 m. (a) Average O_3 for each 500 m bin is represented by the filled circles, 50th percentile for each 500 m bin is represented by the open triangles, and the 5th and 95th percentiles for each 500 m bin are represented by the +. (b) The same as in (a) but for SO_2. (c) The temperature profile along the aircraft spiral during RF3 that recorded the highest SO_2 measurement. The spiral began ~14:25 LST and ended ~14:51 LST on May 18, 2017.

We conduct ensemble HYSPLIT back-trajectories to examine the source of the measured SO_2 over the LIS (Figure 40b). Simulations were conducted for 2 days using archived 3 km High Resolution Rapid Refresh (HRRR) meteorological input (https://rapidrefresh.noaa.gov/hrrr). The ensemble back-trajectories end over the LIS at 3016 m (Figure 41b), the height of the highest SO_2 measurement. All SO_2 measurements were taken on May 18th between 14:48 and 14:50 LST. The black dots in Figure 41 along the back-trajectories represent power plants in operation on May 17th and 18th according to the Continuous Emissions Measurement Systems (CEMS) data. To monitor emissions, the EPA requires installation of CEMS instruments on power plant exhaust towers. Species important for air quality are measured, such as SO_2, NO_x, Particulate Matter, and other Hazardous Air Pollutants (HAPs) (https://www.epa.gov/emc/emc-continuous-emission-monitoring-systems). We use these data to highlight active point sources of SO_2 along the back-trajectory paths, indicating possible sources for the high SO_2 and O_3 aloft over the LIS.

To confirm the presence of synoptic meteorological conditions favorable for atmospheric transport, we conducted two additional ensemble back-trajectories, from a height of 2500 m (Figure 41a) and 3500 m (Figure 41c) respectively. A consistent pattern is discernable among all three trajectory figures.

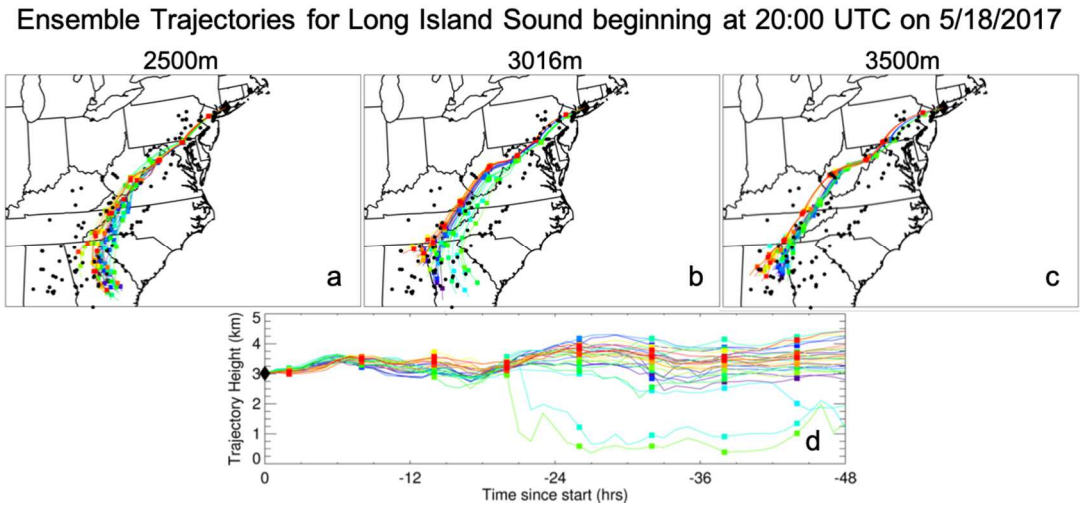

Figure 41: 2-day ensemble HYSPLIT back-trajectories ending at the location of the highest SO_2 measurement over Long Island Sound. The trajectories end at 3 different heights: (a) 2500 m, (b) 3016 m, and (c) 3500 m. (d) Trajectory height shown for the trajectory ending at 3016m (b) over the 48-hour back trajectory period. The black dots represent power plants with CEMS reported SO_2 emissions during the time period.

Review of a NASA Worldview true-color image of the US East Coast on May 17, 2017 at ~13:30 LST, shows fair-weather cumulus along the Appalachian Mountains, following the HYSPLIT back-trajectory paths (Figure 42). This image is approximately 24-hours prior to the highest SO_2 measurement in the LIS. The fair-weather cumulus clouds indicate vertical mixing in the atmosphere [*Chen et al.*, 2012; *Ching and Alkezweeny*, 1986; *Seigel*, 2014] where emissions from power-plants (black dots in trajectory figures) could be vented to an elevation shown in the HYSPLIT back trajectories and thus transported to the LIS.

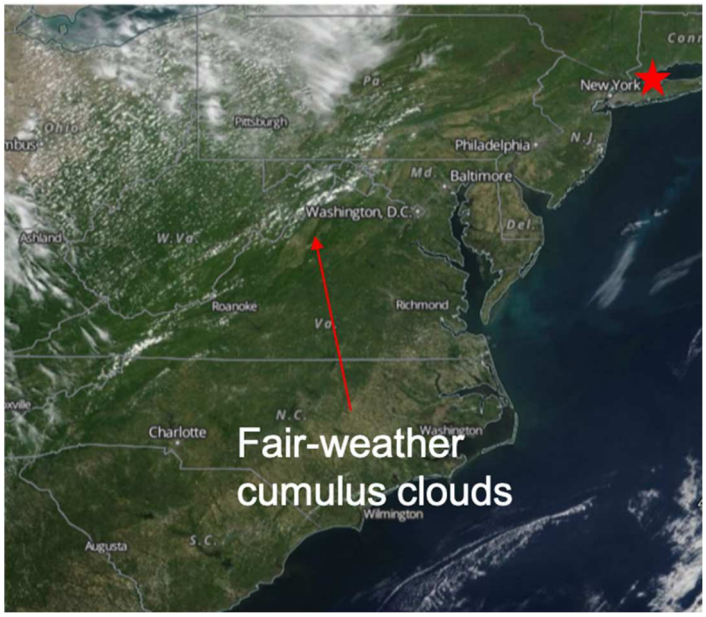

Figure 42: NASA Worldview true color image from Suomi NPP/VIIRS for May 17, 2017. The red star represents the approximate origin of the back-trajectories. Fair weather cumulus clouds are present along the HYSPLIT trajectory. Imagery can be found at: https://worldview.earthdata.nasa.gov/.

Additional comparison of the trajectories with archived NAM surface observations for May 17, 2017 at 18z and 21z shown in Figure 43, and archived Storm Prediction Center (SPC) analysis from May 17, 2017 at 12z and from May 18, 2017 at 00z shown in Figure 44 confirm the presence of a high-pressure system centered just east of the US coast near Bermuda. Surface observations in Figure 43 show southerly winds over the Appalachian Mountains, clear sky conditions, and warm surface temps (85-90°F); atmospheric conditions that are prime for O_3 production and transport. The upper air maps in Figure 44 further support the southerly to south-westerly winds along the Appalachian Mountains into the LIS region.

This atmospheric pattern is known for bringing pollution from upwind sources into the Mid-Atlantic and Northeast regions of the US. Emissions of SO_2 from power plants coincide with emissions of NO which produce O_3 relatively close to the emission

source, once the balance between NO and NO_2 has shifted towards NO_2 [*Cleveland and Graedel*, 1979]. Due to their short atmospheric lifetime, concentrations of NO (and NO_2) are not transported like SO_2 and the resulting O_3 [*Cleveland and Graedel*, 1979; *He et al.*, 2016b; *Ryan et al.*, 1998; *Stehr et al.*, 2000] which explains elevated levels of O_3 (Figure 40a) and SO_2 (Figure 40b) in the highest 500m bins, with little NO_2 (Figure 38b).

In summary, analysis of atmospheric conditions during May 17, 2017 strongly indicate long-range transport of pollution contributed to the elevated measurements of SO_2 and O_3 aloft in the LIS region on May 18, 2017.

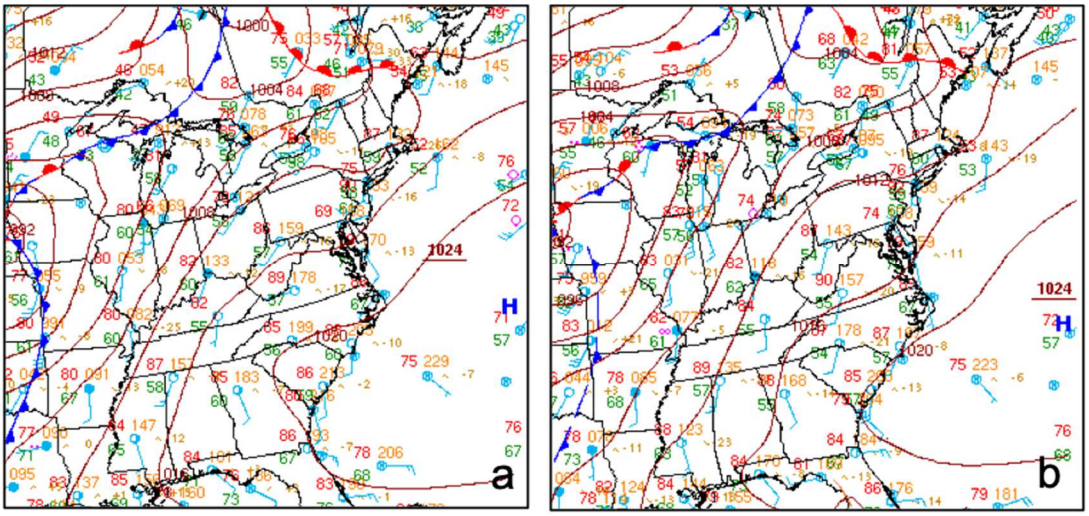

Figure 43: Archived surface analysis with observations from the NOAA Weather Prediction Center (WPC) for May 17, 2017 (a) at 18z and (b) 21z. Both maps are zoomed in over the Eastern US, highlighting the region of the HYSPLIT back-trajectories. Archived surface maps can be found here: https://www.wpc.ncep.noaa.gov/archives/web_pages/sfc/sfc_archive.php.

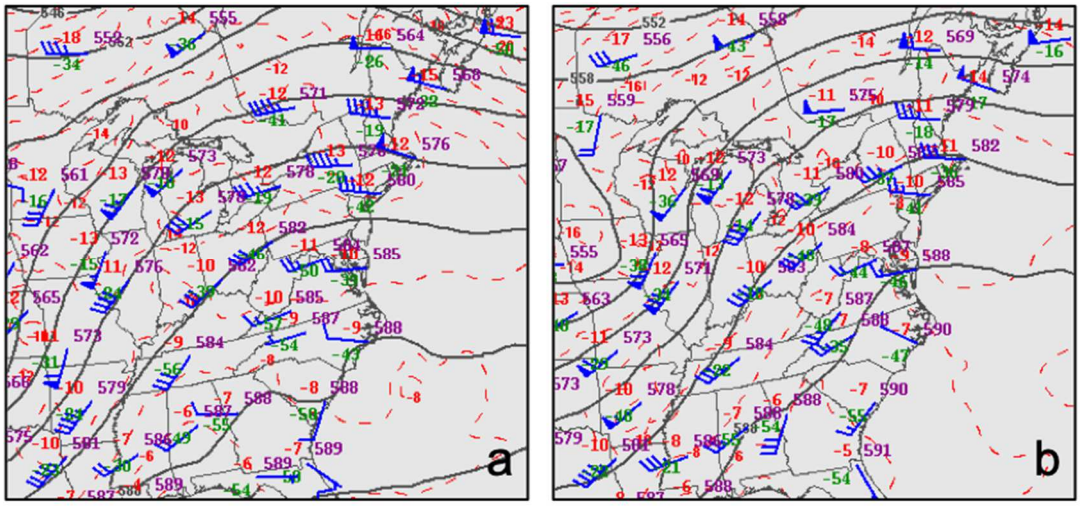

Figure 44: Archived 500mb upper air maps with observations from the NOAA Storm Prediction Center (SPC) for (a) May 17, 2017 at 12z and (b) May 18, 2017 at 00z. Both maps are zoomed in over the Eastern US, highlighting the region of the HYSPLIT back-trajectories. Archived upper air maps can be found here: https://www.spc.noaa.gov/obswx/maps/.

4.6: Comparison of RAMMPP Data with Forecast CMAQ Output

4.6.1: Measured and Modeled O_3, NO_2, and CO

Research flights were conducted on May 17 and 18, 2017 because the CMAQ air quality forecasts from NOAA indicated an O_3 exceedance event would occur. These forecast model simulations of O_3 are directly compared to observational data for all RFs (Figure 45). The CMAQ model platform used by NOAA is described in Section 1.5.2.

Figure 45 (a, b, and c) show O_3 measured along each RF plotted over modeled O_3. To create the curtain of modeled O_3, we find the closest surface CMAQ grid cell spatially and temporally to the aircraft observation and extract O_3 from all the grid cells above that point. The extracted O_3 is then plotted as a function of time and height for comparison to RAMMPP observations. This method allows the modeled atmosphere

to be sampled in a similar manner to how the aircraft observed the actual atmosphere. Figure 45 (d, e, and f) show the average of the 1st km of O_3 from CMAQ at hour 17 EST (d), hour 10 EST (e) and hour 15 EST (f) each corresponding to the figure above, with measured O_3 from the flight path again over plotted.

For RF1 (Figure 45a) the model and data show good agreement above 1.5 km but indicate differences by as much as 50 ppb near the surface (~17:15 and 17:45 EST). The spiral at 17:15 EST occurred just outside the model surface plume in Figure 45d, in the middle of CT. The spiral at 17:45 EST occurred at the CT border with Massachusetts shown in Figure 45d, again outside the CMAQ surface plume. Comparing Figure 45a and Figure 45d we notice CMAQ produced an O_3 plume mostly capturing the vertical structure of the high O_3 concentrations (between hours 16 and 17 for example), but missed the magnitude and horizontal extent of the plume. Measured near-surface air quality was in excess of 100 ppb for the spiral at 17:45 EST, but CMAQ only modeled concentrations between 50 and 60 ppb.

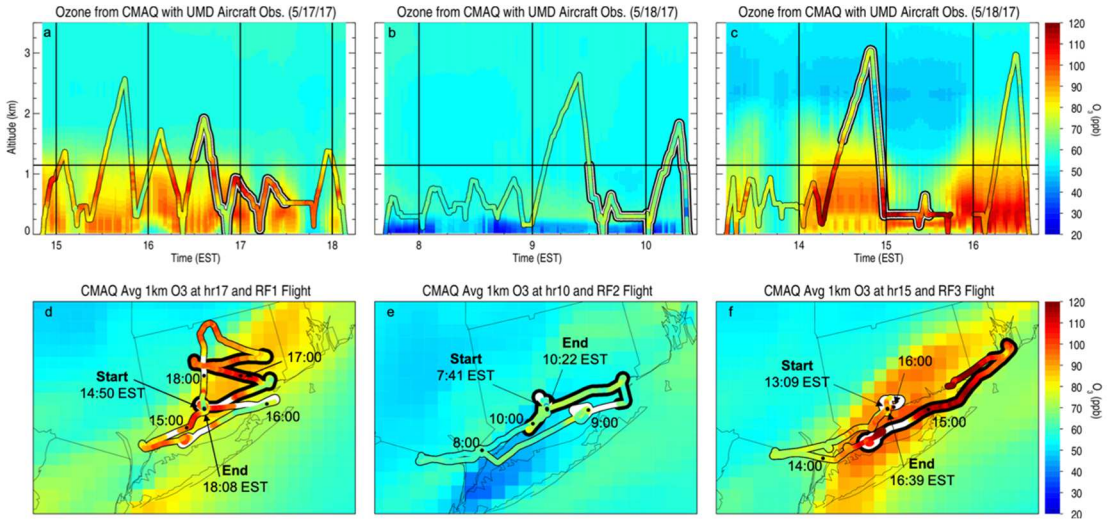

Figure 45: The top three panels show RAMMPP aircraft measured O_3 plotted over curtains of modeled O_3 concentrations from the closest CMAQ grid point for (a) RF1 (b) RF2 (c) RF3. The bottom three panels show RAMMPP aircraft measured O_3 plotted over average 1 km CMAQ O_3 at (d) hour 17 EST of RF1, (e) hour 10 EST of RF2 and (f) hour 15 EST of RF3. Hour demarcations are shown in all plots

for convenience. The bolded portion of the flight data (outlined in black) in the top three panels is also shown in its corresponding panel below (a and d, b and e, c and f). The bolded portion is centered around the hour shown in the bottom three panels. The white portion of the flight path in the bottom three panels corresponds to flight observations at altitudes higher than ~1 km.

For RF2 (Figure 45b), measured and modeled O_3 show similar concentrations aloft of ~250 m. At hours 9 and 10 the aircraft again measured near surface O_3 to be ~50 ppb higher than modeled values. In the 1st km over the LIS near NYC (Figure 45e), CMAQ produces O_3 concentrations ~ 40 ppb, much smaller than measured values. Overall, RF2 O_3 and average 1 km CMAQ O_3 are similar along much of the flight track.

Comparison of modeled and measured O_3 (Figure 45c) from RF3 shows similar results to RF1, however the differences are even greater (see ~14:15 EST). CMAQ does produce an O_3 plume at hour 16 (not pictured) that corresponds well with the aircraft measurements. Additionally, the model resolves a thin filament of high O_3 between hours 15 and 16 in Figure 45c corresponding to measured aircraft values but shows a slight vertical displacement. Clear model underestimations of O_3 are shown in Figure 45f, especially along the flight track over the LIS. This magnitude discrepancy is quite large (~30 to 40 ppb) and corresponds to areas where the measured O_3 levels are well above modeled values. Overall for this observational campaign, CMAQ forecasts generally capture the vertical and temporal extent of O_3 plumes but are below (in some cases severely below) the observed magnitudes.

Correlations of the measured and modeled O_3 for each RF are shown in Figure 46. These plots indicate poor or no correlation of the measurement with its corresponding closest CMAQ grid point and vertical level for all three RFs. All three panels indicate a general underestimation of modeled compared to measured O_3 shown

as negative normal mean bias (NMB) values and mean ratios < 1, which agrees well with panels a-c in Figure 45. For modeled and measured O_3 to have good agreement, CMAQ must produce the appropriate magnitude of O_3 in the correct grid cell; a significant challenge for an air quality model with a resolution of 12 × 12 km grid boxes and 35 vertical levels. Based on Figure 45, we see CMAQ produced high O_3 but usually in the wrong location. This explains the poor correlations in Figure 46.

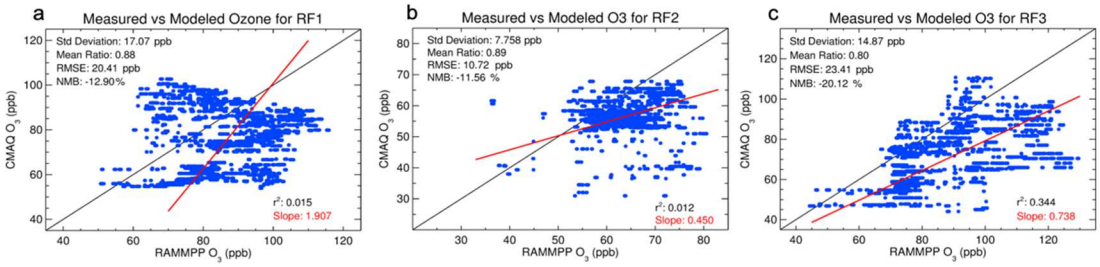

Figure 46: Scatter plots comparing measured O_3 from the RAMMPP aircraft and modeled CMAQ from the closest grid point and model layer for (a) RF1, (b) RF2, (c) RF3. The standard deviation, mean ratio (CMAQ O3/RAMMPP O3), root mean square error (RMSE), normal mean bias (NMB), liner fit, and r^2 are calculated for each flight.

In this CMAQ configuration, the first model layer is ~40 m (necessary for computational speed) compared to the UMD CMAQ configuration that has a first model layer of ~20 m. The lower vertical resolution of the NOAA CMAQ model may explain some of the vertical displacement of O_3. Small-scale boundary layer dynamics are known to impact surface O_3 concentrations [*Loughner et al.*, 2011; *Loughner et al.*, 2014; *Mazzuca et al.*, 2017; *Sillman et al.*, 1993; *Stauffer et al.*, 2015] so improving model resolution near the surface may help correct this issue.

Comparisons of measured and modeled NO_2 were also performed. NO_2 is critical to O_3 production and therefore requires appropriate representation within the CMAQ framework to accurately model O_3. Figure 47 panels a, b, and c show measured

NO_2 along the RAMMPP flight track over a curtain of modeled CMAQ NO_2 from the closest model grid point. Near-surface modeled NO_2 values are generally high compared to measured, especially in Figure 47b just before 9 EST and Figure 47c at ~14:15 EST. In both cases, measured NO_2 is much lower than modeled NO_2.

Comparison of Figure 45b and Figure 47b show low O_3 collocated with very high NO_2 which may indicate near-surface VOC-sensitivity in the morning hours over the LIS within the CMAQ model framework. The corresponding measurements of O_3 and NO_2 in these regions do not agree with the model, therefore model adjustments are necessary to rectify this discrepancy with the data.

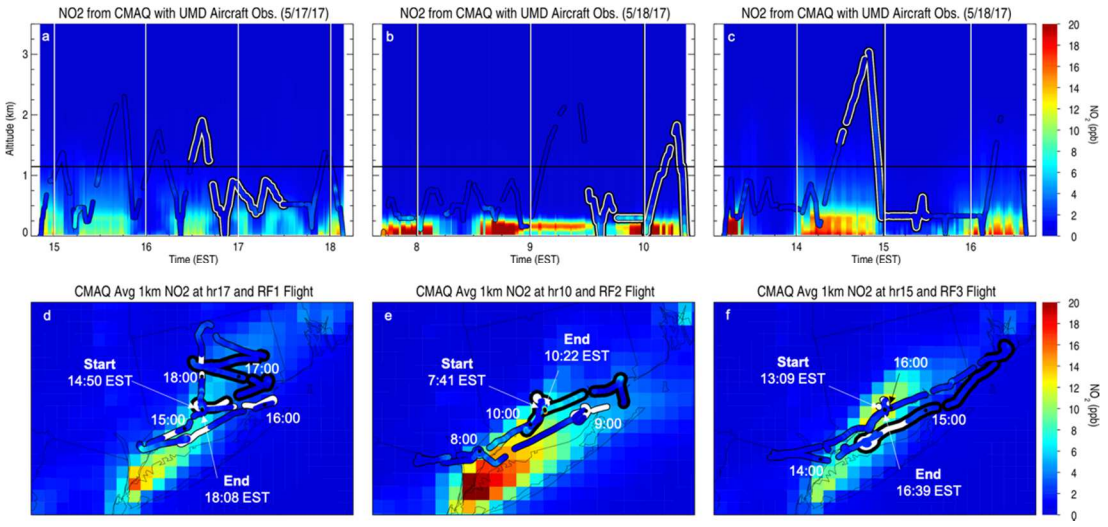

Figure 47: Same as Figure 45 except for NO_2.

Panels d, e, and f of Figure 47 show NO_2 measured by the RAMMPP aircraft (below ~1 km) over average ~1 km CMAQ NO_2 for the indicated hour. Measured NO_2 values agree well with modeled NO_2 outside of the plume downwind of NYC over the LIS (most evident in Figure 47e and f). Elevated levels of NO_2 are shown along the

model plume over the Connecticut coastline in Figure 47e, however measurements directly over the LIS within the urban plume are much lower than modeled NO_2.

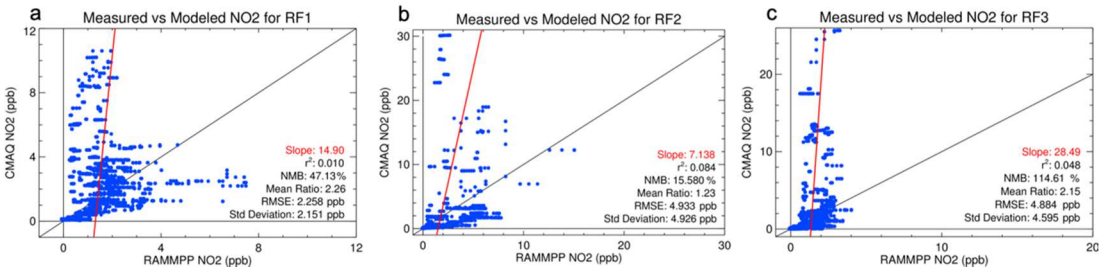

Figure 48: Same as Figure 46 except for NO_2.

Poor correlations of measured and modeled NO_2 are shown in Figure 48, along with significant overestimation of CMAQ NO_2 compared to measured NO_2. Based on Figure 47 and Figure 48, it is evident that the measurements and model agree well at low NO_2 mixing ratios, aloft of the near-surface region. The outliers shown in Figure 48 are from near-surface regions within the model. It is important to note that this forecast CMAQ simulation does not include the necessary 50% reduction of mobile NO_x first discovered by *Anderson et al.* [2014]. Implementation of the 50% emissions reduction of mobile NO_x will likely not be enough to offset the large overestimation of model near-surface NO_2 in the noted plumes shown in Figure 47. Therefore, it is possible that the NO_2 emissions in some model grid cells are much too high and/or vertical mixing of pollutants within CMAQ is not representative of the actual atmosphere.

Comparison of measured and modeled carbon monoxide (CO) are performed to examine the vertical mixing within the forecast CMAQ model. Figure 49 panels a, b, and c show the CO measured along the respective flights over the curtain of model

output from the closest CMAQ grid point. Overall, the model produces much larger CO mixing ratios near the surface than are measured.

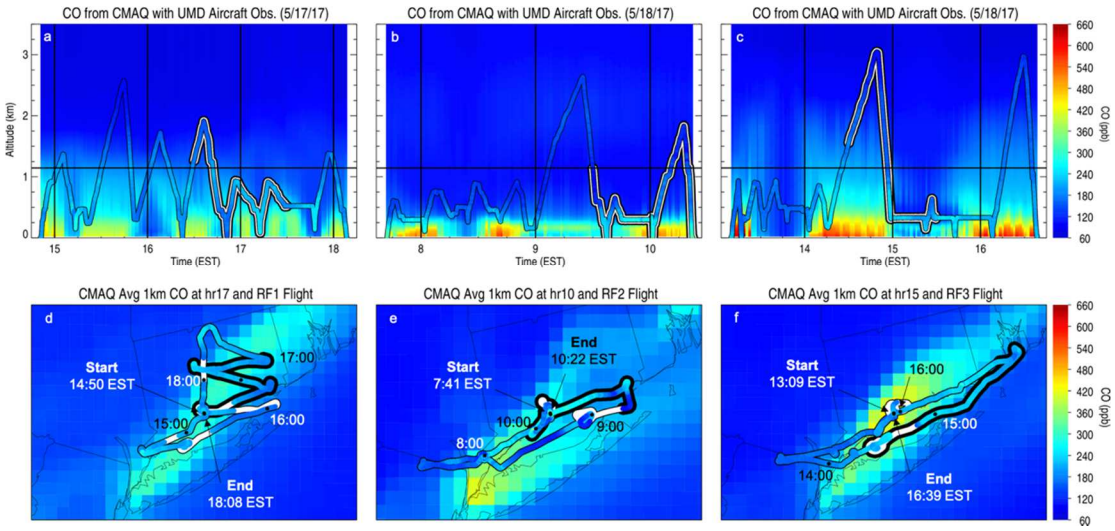

Figure 49: Same as Figure 45 except for CO.

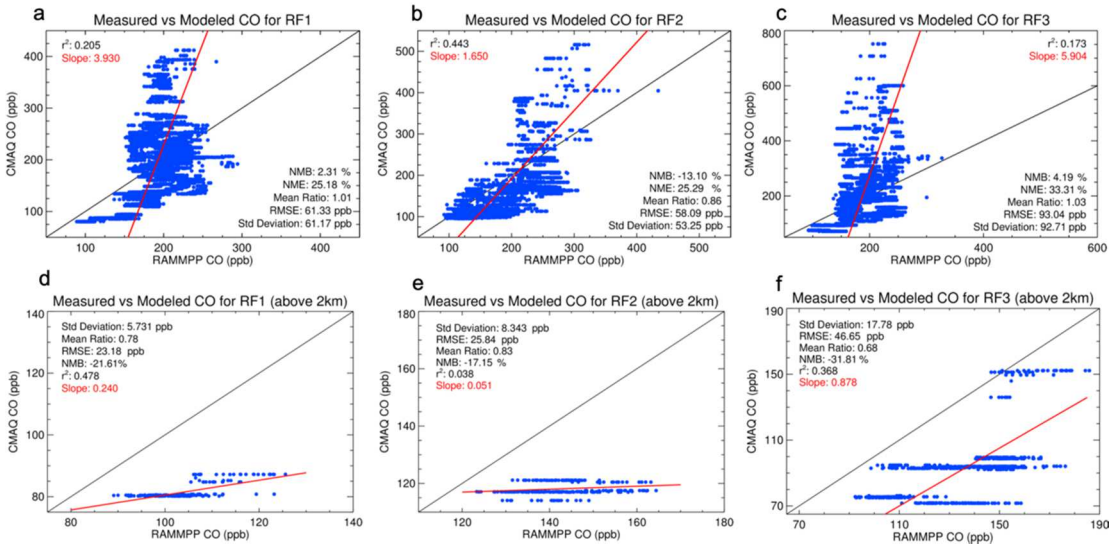

Figure 50: Same as Figure 46 except for CO (panels a, b, and c). Panels d, e, and f compare values above 2 km.

Figure 50 panels a, b, and c show scatter plots comparing measured and modeled CO for the respective RFs. CMAQ produces much larger CO values than are

measured in the near-surface region, especially for RF3 shown in panel c. Panels d, e, and f of Figure 50 compare measured and modeled CO at altitudes above 2 km and should mostly represent background CO values. In this region, CO from CMAQ is consistently low compared to observations. The overestimation at the surface coupled with the underestimation above 2 km could indicate vertical mixing within the model is too slow (i.e. CO is not mixing aloft fast enough), and/or it could indicate CO emissions are too high in the model.

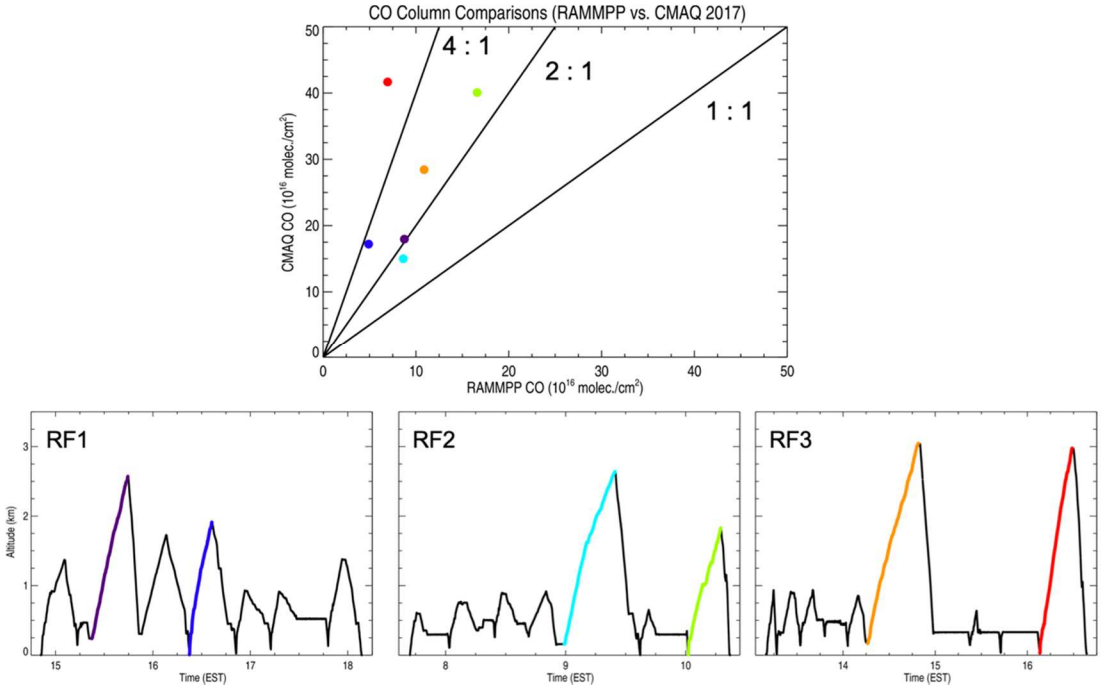

Figure 51: Comparison of measured and modeled column CO for six color coded spirals (three panels below). The 1:1, 2:1 and 4:1 lines show the degree of modeled CO overestimation compared to measured CO.

Integrated column concentrations of measured and modeled CO are calculated along six spirals (highlighted in Figure 51). The closest CMAQ grid point to each RAMMPP measurement is used in the column integration. The total column concentration for each spiral is shown in the top panel of Figure 51. Based on this

analysis, the modeled column CO is high by a factor of 2 for some spirals and a factor of 4 for others. The underestimation of modeled CO above 2 km coupled with the large overestimation of the integrated column CO provides evidence that vertical mixing within the model is too slow. Further analysis is necessary to definitively prove this point.

4.6.2: Measured and Modeled VOCs

It is difficult to compare observed and modeled VOCs because CMAQ uses the CB05 chemical mechanism and therefore produces concentrations for VOC groups rather than individual VOC species. We reference the CB05 documentation (Table 1 of *Yarwood et al.* [2005]) to speciate the measured VOCs into CB05 groups. It is important to note that we are only speciating the 50 measured VOCs into the appropriate CB05 groups; CB05 speciates *many* more VOCs into these representative groups. Therefore, comparisons of magnitude between measured and modeled VOC groups are inappropriate. Instead, we compare the relative composition of the VOC groups in the collected canisters to the composition of VOC groups in the closest CMAQ grid point at the appropriate vertical level. Once speciated, we use the OH reaction rates (k_{OH}) for each VOC group from CB05 (see Appendix B) to compare their relative importance to O_3 formation.

Comparisons for two VOC cans are shown in Figure 52. The left side of Figure 52 shows the relative composition of the collected VOC cans, and the right side shows the relative composition of the corresponding CMAQ grid cell. The time and altitude for the measurement and corresponding CMAQ grid cell are provided. For can ME07812 (top row of Figure 52), relative contribution of the species groups is in good

agreement, however CMAQ has more contribution of isoprene (ISOP) and less olefin (OLE) than was measured in the can. For can ME07817, much more paraffin (PAR) is attributed to the CMAQ grid cell than was measured. It is possible that other VOCs missing from the 50 that were measured contribute significantly to the PAR group, explaining the discrepancy in the composition. It is also possible that the VOCs are speciated incorrectly in CB05 or emissions are incorrectly attributed to the PAR group. Drawing any significant conclusions about CB05 speciation based on composition assessments of 35 VOC cans from a single case study is difficult. We can say however that these cans include more VOCs contributing to the OLE group than are present in the CMAQ output. Further analysis of the speciating algorithm with the newer chemical mechanism (CB6) that includes 26 more species may improve this discrepancy.

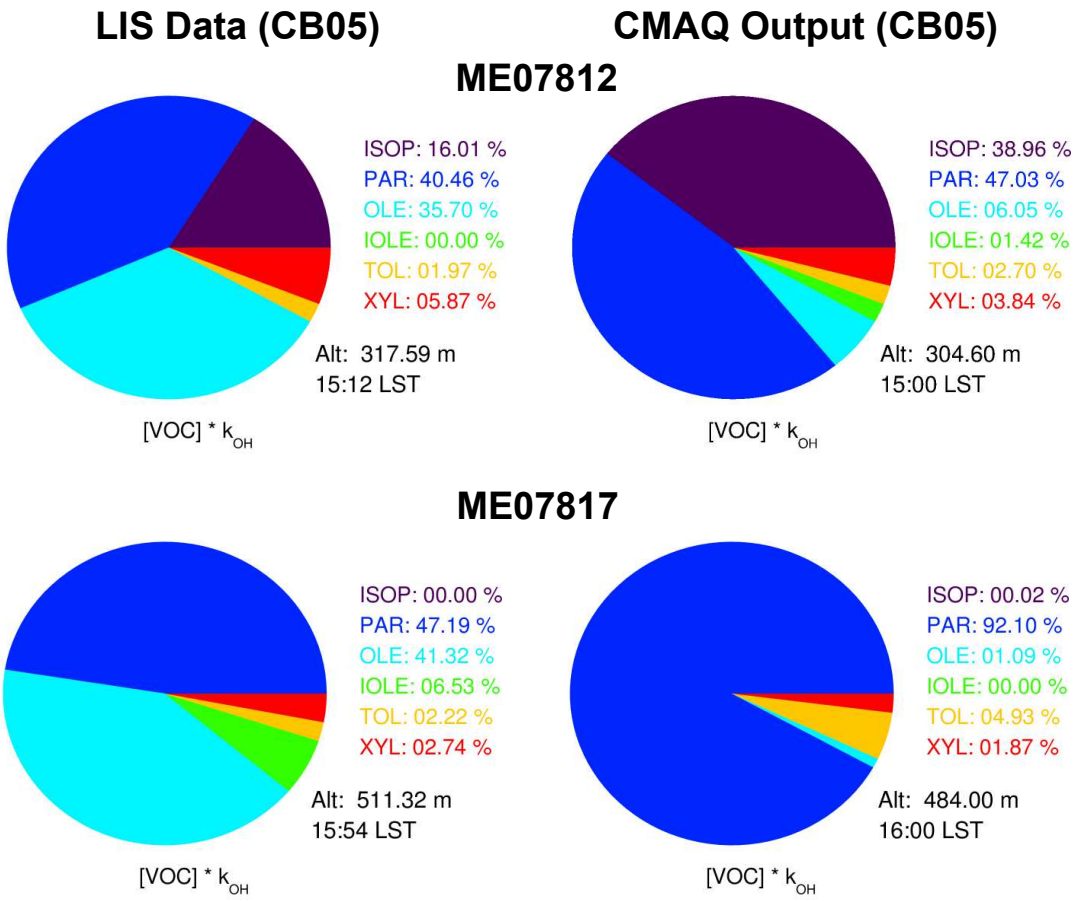

Figure 52: Composition comparison for two example canisters. Top: Can ME07812 data grouped as CB05 (left) and corresponding CMAQ grid point and height (right). Bottom: Same as the top except for can ME07817. Data are expressed in terms of the CB05 reaction rate for each CB05 VOC speciated group.

A recent study by *Zhao et al.* [2019] compared high resolution WRF-Chem modeled and observed 8-hour average O_3 and calculated MDA8 for the May 17 and 18, 2017 air quality episode in the LIS. They state that the biogenic emissions inventory Model of Emissions of Gases and Aerosols from Nature (MEGANv2.04) underestimates isoprene emissions by a factor of two in the LIS. This finding is justified by comparing the correlations between two respective model simulations (unadjusted isoprene and doubled isoprene) with measured surface O_3. *Zhao et al.* [2019] reported that the simulation with doubled isoprene emissions correlates better with surface O_3

observations. *Canty et al.* [2015] determined CMAQ simulations using MEGANv2.1 rather than MEGANv2.04 biogenic emissions produced better agreement between modeled and OMI observed tropospheric column NO_2. The updated MEGANv2.1 inventory reduces isoprene emissions by ~25% compared to MEGANv2.04 [*Canty et al.*, 2015]. According to *Goldberg et al.* [2016], comparison of DISCOVER-AQ BW measurements of isoprene to Comprehensive Air Quality Model with Extensions (CAMx) simulations using MEGANv2.1 biogenic emissions shows significant overestimation of modeled isoprene. Correlation of modeled and isoprene observed during DISCOVER-AQ further improved when CAMx simulations using BEISv3.61 (the biogenic inventory used for all modeling in this analysis) were performed [*Goldberg et al.*, 2016]. Based on these previous studies, it is unlikely that MEGANv2.04 underestimates isoprene emissions by a factor of two. It is possible however that the improved correlation between WRF-Chem simulated and observed O_3 found by *Zhao et al.* [2019] is due to the overall increase in total (highly reactive) VOCs in the region. Their simulations generally underestimated O_3, so increasing concentrations of a highly reactive VOC with a high production of O_3 potential (isoprene in this case), may be the underlying reason for the improved O_3 agreement. The findings by *Zhao et al.* [2019] would be further strengthened if modeled concentrations of isoprene were compared to observations. The RAMMPP VOC observations from the same O_3 event measure little isoprene in the atmosphere compared to other anthropogenic VOCs during the study period.

Figure *53* shows the comparison of measured and modeled isoprene. VOCs were only measured from the air collected in the 35 cans throughout the three flights, limiting the available data for comparison. In

Figure *53* panels a, b and c, a curtain of modeled isoprene is plotted along the flight tracks, with reported isoprene from the VOC cans along the flight path (solid circles). Panels d, e, and f of

Figure *53* show modeled average ~1 km isoprene with the corresponding measured isoprene.

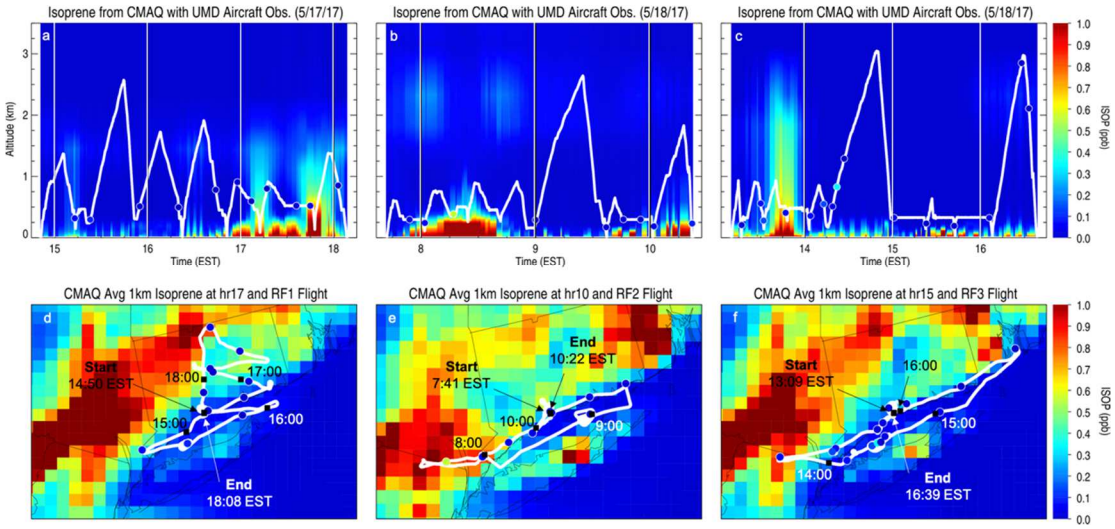

Figure 53: Same as Fig 45 but for Isoprene. The flight tracks are indicated in white with VOC can data shown as circles. Time-steps are shown as black squares in panels d, e, and f.

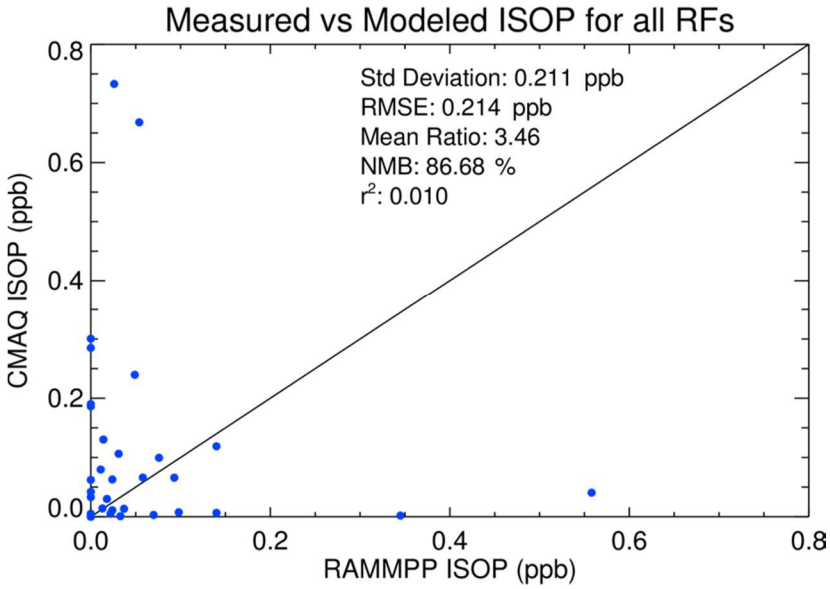

Figure 54: Comparison of measured and modeled isoprene for all three RFs during the May 17 and 18, 2017 flights.

Figure 54 shows no correlation between measured and modeled isoprene. The mean ratio of 3.46 indicates isoprene is generally high in the model compared to observations, but this high bias is not always true.

Figure ***53*** and Figure 54 compare observations and model output for the same O_3 event as examined by the *Zhao et al.* [2019] study and provide further evidence that the *Zhao et al.* [2019] findings (isoprene emissions are underestimated by a factor of 2) are questionable.

4.7: Modeled Sources of VOCs in Long Island Sound

We use CMAQ (configuration described in Section 1.5.1) to examine the various sources of anthropogenic VOCs in the model. All findings discussed in this section reference how the model sees the atmosphere rather than the actual atmosphere,

therefore this section comments only on VOC emission allocation within the CMAQ model framework, not on emission values.

4.7.1: Analysis with the Alpha2 Inventory

Motivated by the modeled surface O_3 dis-benefit when c3 Marine emissions are modified (discussed in Chapter 3 and exemplified by Figure 28), CMAQ simulations with perturbed VOC emissions values were performed. Reducing all anthropogenically produced VOC emissions in the model should show surface O_3 reductions in the same region as the O_3 dis-benefit in Figure 28 assuming the O_3 dis-benefit is because the region is VOC-sensitive. The initial CMAQ analysis is performed using emissions from the available Alpha2 inventory (described in section 1.5.3) because the Beta2 inventory emissions (described in section 1.5.4) were being gathered at the time of this analysis. CMAQ simulations with the Beta2 inventory are discussed in the next section.

To begin, all anthropogenic VOC emissions are reduced by 50%. This is executed in 3 steps:

1. Remove the biogenic emission file from the fully merged model-ready emission file using SMOKE;
2. Reduce all VOC species by half;
3. Re-merge the biogenic emissions with the adjusted VOC file to create the modified model-ready emissions file using SMOKE.

The difference in Average Maximum 8-hr O_3 ($AM8O_3$) (described in Section 3.3) between a CMAQ simulation with 50% reduced anthropogenic VOCs and one without adjustment to the anthropogenic VOCs in the c3 Science framework (Section

3.3, Table 2) is shown in Figure 55. The yellow star indicates the grid box with the largest change in surface O_3; a reduction of ~50 ppb.

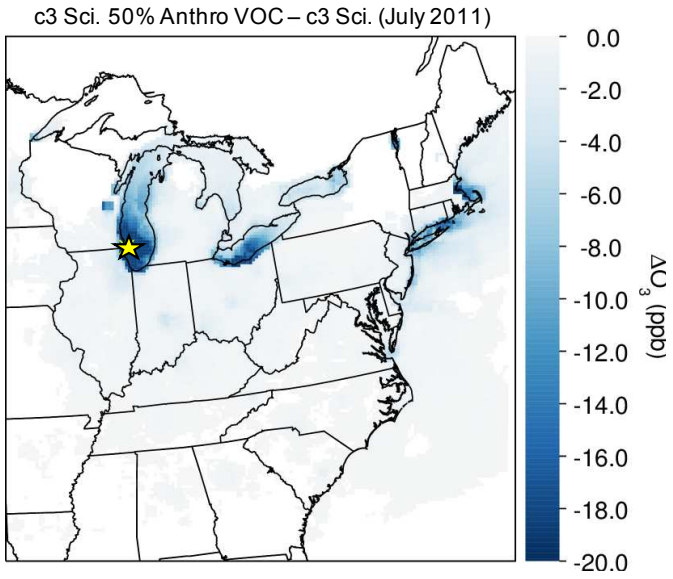

Figure 55: Change in surface O_3 due to reducing anthropogenic VOCs by 50% in the c3 Science (Table 2) model framework. Surface O_3 is represented as Average Maximum 8-hr O3 ($AM8O_3$), a metric used by the EPA and described in Section 3.3. The yellow star marks the grid box with the largest change: 50 ppb.

The largest surface O_3 concentrations are mostly concentrated over large bodies of water, near major cities like Chicago, New York, and Boston. As expected, surface O_3 reductions are shown in coastal NY, CT and MA, the same locations as the O_3 dis-benefit shown in the analysis in Chapter 3. To determine which inventory sector (or sectors) contributes most to this ozone reduction, model simulations with VOC perturbations in specific source sectors are executed. Due to the spatial location of the largest O_3 reductions, we reduced the c3 Marine VOC emissions by 50%. This modification produced an undetectable change in surface O_3 throughout the domain (not shown).

Emissions from power plants (EGUs) and cars have historically been the focus of air quality regulation due to their large emission rates and ubiquity throughout the model domain. Again, based on the spatial distribution of the change in surface O_3 shown in Figure 55 being predominantly over water and near-coastal areas coupled with the small VOC emission values in the EGU inventory files, we determine that EGUs are unlikely to be the predominant sector contributing to the surface O_3 change.

The mobile sector consists of both on-road and non-road sources and has concentrated emissions in the same general regions as the large surface O_3 reductions in Figure 55; densely populated areas like Chicago, New York, and Boston. Model simulations were performed with 50% reductions of VOCs for the entire mobile sector (Figure 56a), the on-road mobile sector only (Figure 56b), and the non-road mobile sector only (Figure 56c). The yellow star in each figure represents the grid box with the largest reduction in surface O_3. Reducing the VOCs from the entire mobile sector results in a maximum surface O_3 reduction of ~43 ppb. The on-road mobile sector adjustment results in a ~3 ppb reduction, and the non-road mobile sector adjustment results in a ~42 ppb reduction of surface O_3. Based on Figure 56a and c, it is likely that the non-road mobile sector is responsible for a considerable amount of surface O_3 within the model framework. Further analyses with the improved Beta2 emissions are necessary to confirm that this holds true with the updated inventory.

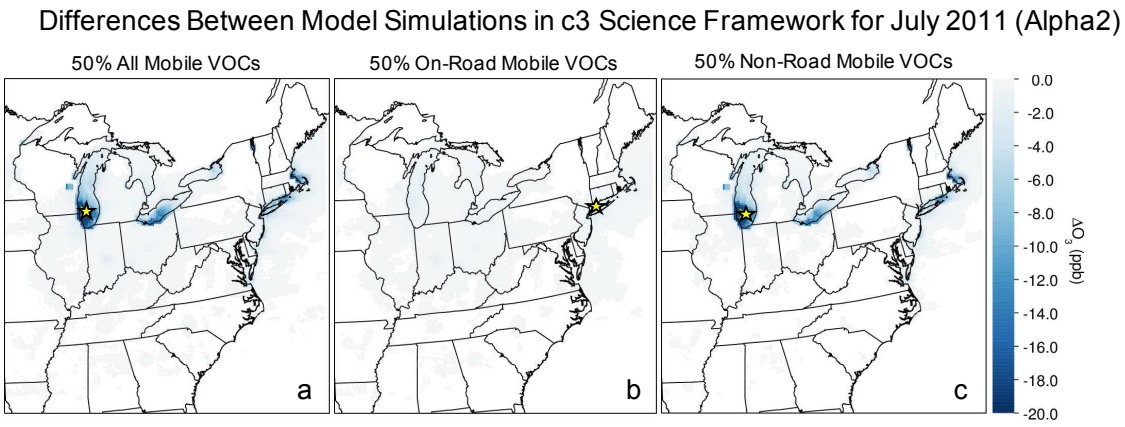

Figure 56: Change in surface O_3 due to reducing VOCs by 50% in the c3 Science (Table 2) model framework for the (a) entire mobile sector (b) on-road mobile only (c) non-road mobile only. Surface O_3 is represented as AM8O3. The yellow star highlights grid box with largest surface O_3 change.

For reference, the non-road inventory represents emissions from vehicles used for recreational purposes, construction, lawn maintenance, industrial and commercial activities, logging, underground mining practices, pleasure boating, and railroad/railyard equipment (not locomotives) [*McDill et al.*, 2015; 2017]. This sector represents emissions from gasoline, diesel, compressed natural gas, and liquefied petroleum gas fuel types [*McDill et al.*, 2015; 2017]. The diverse nature of the non-road sector and its current representation (all sources lumped together) in air quality models makes discerning the specific fuel and/or non-road engine type most responsible for producing the problematic VOCs difficult.

4.7.2: Analysis with the Beta2 Inventory

Model simulations for the month of July in 2011 are performed with the updated Beta2 emissions inventory (described in Section 1.5.4). Anthropogenic VOC emission perturbations are executed as described in the previous section. Figure 57a and b show contours of AM8O_3 from model simulations in the c3 Science framework and the c3

Science framework with 50% reduced anthropogenic VOCs. The white areas within the model domain indicate locations where the minimum threshold of 6 days during the month with Maximum Daily Average 8-hour O_3 (MDA8) above 60 ppb was not met.

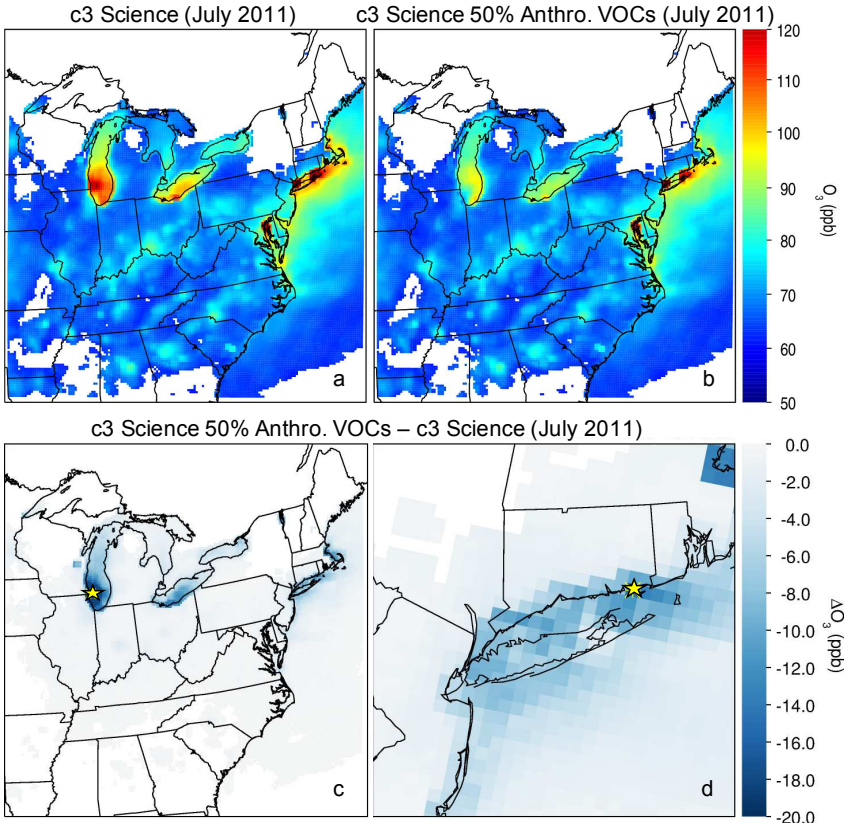

Figure 57: Contours of surface O_3 (represented as AM8O_3) for July 2011 CMAQ model simulations of the (a) c3 Science model platform (b) c3 Science platform with 50% reduced anthropogenic VOC emissions. (c) The change in surface O_3 between the c3 Science and c3 Science 50% Anthro. VOC model simulations. (d) Same as (c) but zoomed in to LIS region. Yellow stars on (c) and (d) mark the grid cell with the largest O_3 reduction for the displayed domain.

Figure 57c and d show the difference between the model simulations shown in Figure 57a and b, with Figure 57d zoomed in over the LIS. We find consistent spatial distribution of surface O_3 reductions near coastal regions over large bodies of water as with the Alpha2 model simulations. The maximum surface O_3 change in the entire model domain is again over Lake Michigan but with a value of ~36 ppb. The maximum

change in the LIS region is ~15 ppb. The smaller maximum change in the Lake Michigan area using the Beta2 emissions compared to the Alpha2 emissions is due to the inventory updates discussed in section. One notable improvement between the two versions is for the non-road sector. In the Alpha2 inventory, the non-road emissions derive from the NEIv1 data, in the Beta2 the non-road emission derive from the NEIv2 data.

Focusing on the mobile sector, we conduct three model simulations with mobile VOC emissions reduced by 50% in the c3 Science framework. Figure 58 shows the surface O_3 reductions for the three VOC perturbation simulations. For the 50% reduced on-road mobile VOC emissions scenario, the maximum change is ~3 ppb in the LIS (Figure 58a and d). For the 50% reduced non-road mobile VOC emissions scenario, the maximum change is ~32 ppb over Lake Michigan (Figure 58b) and ~13 ppb over the LIS (Figure 58d). For the 50% reduced all-road mobile VOC emissions scenario, the maximum change is ~33 ppb over Lake Michigan (Figure 58c) and ~14 ppb over the LIS (Figure 58f).

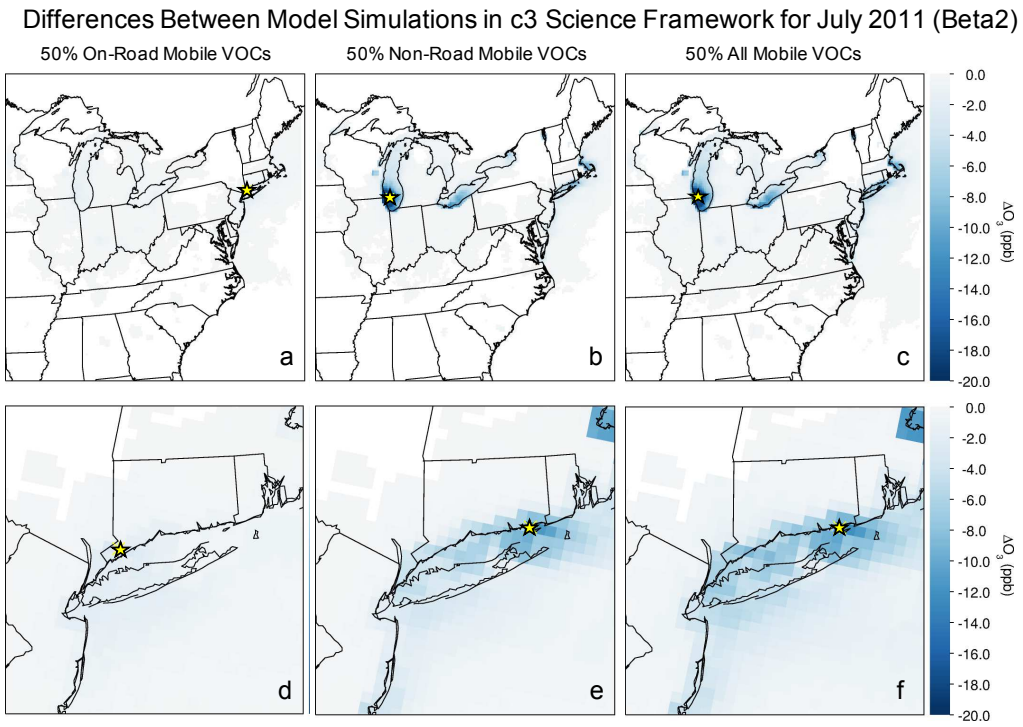

Figure 58: Same as Figure 56 but with Beta2 emissions. (a) c3 Science with 50% reduced on-road mobile VOC emissions, (b) c3 Science with 50% reduce non-road mobile VOC emissions, (c) c3 Science with 50% reduce VOC emissions for all mobile sectors. (d) Same as (a) but zoomed in to LIS, (e) same as (b) but zoomed in to LIS, (f) same as (c) but zoomed in to LIS region. Yellow stars on all panels mark the grid cell with the largest O_3 reduction for the displayed domain.

Figure 59 shows the relative contribution of various modeling scenarios with perturbed mobile VOC emissions to modeled surface O_3 reductions shown in the scenario with 50% reduce anthropogenic VOCs. The percent of the total surface O_3 change due to the 50% reduction of on-road mobile VOC emissions is shown in Figure 59a. The percent due to the emission reduction for the non-road sector is shown in Figure 59b, and percent due to the 50% adjustment applied to both mobile sectors is shown in Figure 59c. Together, these illustrate the impact of VOCs from the mobile emissions sectors to surface O_3 reductions domain wide.

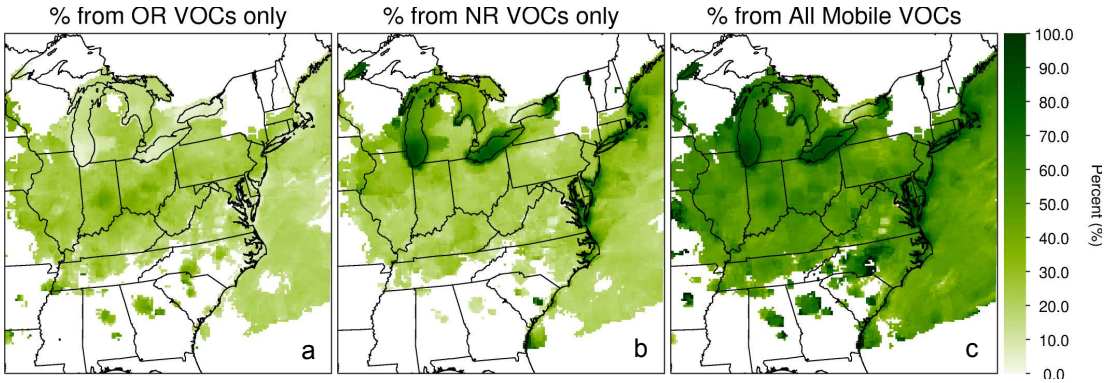

Figure 59: Percent of surface O_3 reductions in the c3 Science model framework attributed to the (a) on-road mobile sector only, (b) non-road mobile sector only (c) non-road and on-road mobile sectors combined, when compared to the simulation with 50% reduction of all anthropogenic VOCs.

It is evident from these simulations that VOC emission reductions from the non-road sector would greatly improve modeled surface O_3 in heavily populated coastal areas. Efforts aimed at ensuring emission inventories contain accurate data for this sector and are allocated correctly, along with further division of this broad modeling sector into more appropriate sources would help discern which specific non-road combustion engines are producing the problematic VOCs. A concerted effort to focus on this sector would greatly benefit air quality policy.

4.8: Conclusions

In this chapter we analyze observations from the RAMMPP aircraft campaign conducted on May 17 and 18, 2017 over the Long Island Sound (LIS), and compare these measurements to DISCOVER-AQ Baltimore-Washington observations. We also compare the RAMMPP data to forecast CMAQ model simulations conducted by NOAA for May 2017. Finally, we conduct model analysis using an in-house CMAQ model platform to discern the emissions sectors most responsible for O_3 formation in the LIS.

We find that atmospheric concentrations of anthropogenic VOCs dominate over isoprene in the NYC area and downwind over LIS throughout the May 17 and 18 O_3 exceedance event. Morning concentrations of VOCs are large compared to afternoon concentrations and may contribute to the high concentrations of O_3 measured later in the day. Propylene and isopentane (produced by the petrochemical industry and evaporative emissions) are shown to be the most important VOCs for O_3 production based on their concentrations and reactivity with OH. Efforts should be made to determine the specific sources of these problematic VOCs.

Comparison of DISCOVER-AQ isoprene, NO_2 and O_3 from the 2011 campaign in the Baltimore-Washington area show that significantly less isoprene and more NO_2 are present in the LIS region than in Maryland. It is possible that the atmosphere in the LIS may be VOC-sensitive at certain times and in certain locations. Elevated levels of O_3 and SO_2 above 2500 m over the LIS are shown to be due to long-range pollution transport. HYSPLIT back trajectories are performed and CEMS data are used to show active power plants along the trajectories. A Worldview image shows cumulus cloud formation along the HYSPLIT trajectories in areas of active power plants, indicating venting of the emissions due to atmospheric convection. Archived surface analysis and 500 mb maps show the presence of a high-pressure system off the east coast of the US during this time producing atmospheric flow consistent with the HYSPLIT trajectories.

CMAQ results from the NOAA National Air Quality Forecast Capability system for May 17 and 18 were compared to RAMMPP aircraft observations. Overall, the model produces concentrations of O_3 that support issuing an air quality alert, however it misses the full magnitude of the measured O_3 and often displaces the O_3

horizontally and vertically. Higher resolution modeling of the near-surface atmosphere may help to improve the distribution of O_3 within CMAQ. Comparison of measured and modeled CO indicate emissions of CO are too high by as much as a factor of 4 in the NYC/LIS region. Initial analysis indicates vertical mixing within the forecast CMAQ model framework is too slow.

Finally, model simulations conducted with two EPA emissions inventories indicate the non-road mobile sector contributes significantly to surface O_3 production in the LIS. The non-road sector consists of a variety of sources including recreational boats, construction vehicles, and railyard vehicles (not locomotives). Surface O_3 is significantly reduced when model simulations with 50% reductions in VOC emissions from the non-road mobile sector are performed. Areas with the largest reductions are over bodies of water like Lake Michigan (~32 ppb) and the Long Island Sound (~13 ppb). We suggest that air quality policies should consider controlling VOC emissions from member sources to the non-road sector. Inventory developers should consider providing model-ready emissions files that further categorize the non-road mobile inventory so model simulations can test attainment strategies that target specific sectors like recreational boating. A detailed, data-driven analysis of the various sub-categories that make up the non-road inventory is needed to verify the emission strength and attribution to this sector.

Chapter 5: Concluding Remarks

5.1: Conclusions from this Research

The work presented in this thesis provides the following contribution to the air quality community by answering the questions presented in Section 1.6:

1. Does the regulatory CMAQ modeling platform accurately represent the atmosphere? If not, what modifications can be made to improve this representation? How does this impact modeled ozone?

We found near-shore emissions from the largest shipping vessels (class 3 Commercial Marine Vessel (c3 Marine)) to be represented incorrectly in the regulatory CMAQ modeling platform. Modifications were performed to generate consistency between the off-shore and near-shore emissions files for the c3 Marine inventory sector. Comparison of baseline (unadjusted) and modified (c3 Adjust) simulations were performed. Model results show a decrease of Average Maximum 8-hr O_3 ($AM8O_3$) at Maryland AQS sites along the Chesapeake Bay where photochemical O_3 production is NO_x-sensitive (e.g. a decrease of ~6.5 ppb of O_3 at Essex, MD). This adjustment had the adverse effect of increasing $AM8O_3$ by ~3.5 ppb in the Long Island Sound (LIS). This result suggested local production of O_3 being within the VOC-sensitive regime. Vertical distribution of the near-shore c3 Marine emissions also improved model pollution dispersion and transport associated with these emissions; they are no longer remaining near the emission source, over-producing O_3 locally. Based on these changes, we conclude the CMAQ model represents the actual atmosphere more accurately.

Emissions for future year simulations are grown from a designated base year. In the 2018 modeling scenarios, AM8O_3 reductions are larger for the Chesapeake Bay (e.g. a decrease of ~13.6 ppb O_3 at Essex, MD). Surface O_3 in the LIS shows smaller increases that in the 2011 modeling, indicating the area may be transitioning to NO_x-sensitive conditions in the future. Analysis of a Maryland Department of the Environment (MDE) attainment strategy indicates legislation aimed at limiting O_3 precursors should be more effective in the adjusted model scenarios with the than in the baseline CMAQ simulation. This has important policy implications because incorrect emissions inventories for future years may obscure the true impacts of proposed attainment strategies.

We also examine accuracy of the NOAA forecast CMAQ model platform. We compare aircraft data to model output for the May 17 and 18, 2017 O_3 event over the LIS. Overall, the model reproduces an O_3 exceedance event, however it misses the full magnitude of the measured O_3. Additionally, this O_3 is often displaced from measured values. Limitations of model resolution may be to blame for this discrepancy.

2. Can we use CMAQ and relevant data sources to determine photochemical O_3 production regimes across the model domain?

We use column HCHO and NO_2 retrievals from the Ozone Monitoring Instrument (OMI) to calculate HCHO/NO_2 ratios across the CMAQ model domain. Baseline CMAQ ratios shows a larger area over the New York metropolitan area is within the VOC-sensitive to NO_x-sensitive transition region than is observed by the satellite. When empirically based model improvements are incorporated, known as the

c3 Science scenario (see Table 2), model performance improves compared to the satellite. Other metropolitan areas like Baltimore-Washington (MD), Chicago (IL), and Detroit (MI) are analyzed. Chicago and Detroit metro areas are within the transition region in the model framework; the satellite shows them as NO_x-sensitive. For the Baltimore-Washington region the model agrees well with the satellite; model and observations show the area to be NO_x-sensitive. In all cases, the proposed model adjustments improve performance in relation to the observed satellite $HCHO/NO_2$ ratio and more accurately represent tropospheric conditions. This comparison is relevant for *column* ratio calculations, not surface calculations for photochemical O_3 production regime. Care must be taken to keep from over-attributing column calculated ratios to surface conditions.

3. How does the photochemistry in the New York City pollution plume impact heavily populated areas downwind?

Analysis of aircraft observations for the May 2017 episode shows anthropogenic VOC concentrations are more important than isoprene over NYC and the LIS in the Planetary Boundary Layer. This goes against the conventional wisdom that isoprene, from biogenic sources, is the dominant VOC in the Eastern US. Air parcels decoupled from the surface biosphere will quickly lose isoprene ($\tau = \sim$1-2 hours) relative to longer lived anthropogenic hydrocarbons.

Diurnal variation in VOC concentrations are large, suggesting morning concentrations may contribute to high concentrations of O_3 observed later in the day. Propylene and isopentane are shown to be the most important VOCs for O_3 production

in the LIS for these flights. Comparison of isoprene, NO_2 and O_3 between the RAMMPP and DISCOVER-AQ campaigns show significantly less isoprene and more NO_2 are present in the LIS than in Maryland. It is possible that at certain times and locations, atmospheric conditions may be VOC-sensitive in the LIS. Determination of the specific sources for the anthropogenic VOCs measured over the LIS, along with the temporal emissions rates would improve air quality attainment strategy development.

4. What are the important emissions sectors contributing to O_3 production in heavily populated, near-coastal, urban centers within the model domain?

Model simulations performed with the EPA Alpha2 and Beta2 emissions inventories indicate the non-road mobile sector contributes significantly to surface O_3 production in near-coastal urban areas. The non-road sector is a catch-all for fossil fuel burning sources including pleasure craft boats, recreational vehicles, lawn care equipment, and construction vehicles. Surface O_3 is significantly reduced when model simulations are performed with 50% reductions in VOC emissions from the non-road mobile sector. This reduction is not feasible for current attainment strategies, but it serves to highlight the importance of this inventory sector to modeled surface O_3 in areas with high modeled surface O_3 like the LIS (~13 ppb) and downwind of Chicago (~32 ppb) (see Figure 58e and b respectively).

Surface O_3 decreases of this magnitude are considerable compared to other attainment strategy modeling efforts performed by the University of Maryland MDE modeling group. Focus for attainment strategy development for the LIS has been given mostly to peaking units or auxiliary power units; electricity generation from small

sources used during high-demand days [*McDill et al.*, 2017]. This effort has provided evidence and motivation for development of attainment strategies focusing on the non-road sector. Emission strength and attribution from the member sources should be confirmed with data.

State Implementation Plans (SIPs) are complete outlines for how the State proposes to meet the required NAAQS standards. These include the full cost analysis of the proposed emissions reductions [*EPA*, 2018d]. Air directors for each state must therefore provide evidence that the proposed control measures are necessary and cost-effective. Justification for the proposed emissions reductions stems directly from modeling efforts, like those described in this thesis. Therefore, improving model representation of the actual atmosphere is of paramount importance, and providing direction for effective attainment strategies is critical for the success of future SIP development.

The main findings about air quality from this work can be applied worldwide, especially to coastal urban centers. Approximately 40% of the world's population lives within 60 miles of the coast [*UN*, 2017] and is impacted by coastal activity. Pollution from large urban centers and shipping ports therefore impacts significant populations worldwide. Mitigation of pollution in these areas is paramount to the health and well-being of human populations.

5.2: Needs for the Air Quality Community

5.2.1: Model and Emission Inventory Improvements

The modeling in this research is performed with the regulatory air quality model used by the state of Maryland to develop air quality attainment strategies. This CMAQ platform is for 12 × 12 km resolution over the Eastern half of the US. Based on lake/bay breeze studies discussed previously [*Loughner et al.*, 2014; *Mazzuca et al.*, 2017; *Sillman et al.*, 1993; *Stauffer et al.*, 2015], it is necessary to increase model resolution to resolve these small-scale events. Using a nested modeling domain over the targeted regions may improve the dynamical representation of these events. This is important for near-coastal areas as high O_3 events are often associated with this atmospheric flow [*Loughner et al.*, 2014; *Mazzuca et al.*, 2017; *Sillman et al.*, 1993; *Stauffer et al.*, 2015]. Incorporation of this nested, high-resolution modeling scheme into the commonly used regulatory modeling platform would improve attainment strategy development.

Source-apportionment model analysis would be improved by the division of catch-all inventory sectors like the non-road mobile and non-point inventories [*McDill et al.*, 2017]. The current non-road mobile inventory consists of a variety of combustion sources, some over water and some over land. Further separation of these sources would provide the ability to examine the contribution of each specific combustion source to surface O_3 production. Analysis of the pollution associated with marine pleasure craft will be useful in the LIS, Chesapeake Bay, and Great Lakes region.

Finally, more focus on particulate matter ($PM_{2.5}$ and PM_{10}) modeling efforts are necessary. Particulate pollutants can be emitted directly into the atmosphere from sources like wildfires, smoke stacks, engine exhaust, and construction sites, or formed

in the atmosphere as secondary pollutants through reactions with, for example, SO_2 or NO_x compounds [*EPA*, 2018c]. Fine particulate matter is a source of human health issues including impaired lung function with inhaled into the lungs, and cardiovascular problems when particles ($PM_{2.5}$) cross the alveolar barrier into the blood stream [*EPA*, 2018c; *Fann et al.*, 2018; *Pope et al.*, 2002; *Pope and Dockery*, 2006]. Urban centers have large populations and emissions of PM associated with construction sites and combustion sources (cars, trucks, buses, shipping vessels, ferries, etc.) are numerous. City-scale modeling of these sources would improve understanding of the full extent of common exposure levels to PM. Larger scale modeling would highlight upwind sources of PM and the transport of PM throughout the domain. Air quality policy modeling efforts have mostly been focused on O_3; it is time to broaden the scope to include PM.

5.2.2: Field Campaigns and Measurements

This body of work has focused on the air quality in large coastal population centers where people are exposed to poor air quality episodes specifically related to O_3. Data for these areas, especially the New York City/Long Island Sound (LIS) region are scarce, relying heavily on available ground-based monitoring networks. A robust field campaign like the previous DISCOVER-AQ campaigns in Baltimore-Washington (2011), Houston (2013), California (2013), and Colorado (2014) would enhance the understanding of pollution in this region.

As shown earlier in Figure 4, the NJ/NYC/CT area currently has the worst air quality on the East Coast. A field mission dedicated to discerning the specific causes for this poor air quality is necessary. Measurement of air in the NYC/NJ urban centers,

air upwind, and air downwind would help to characterize emission flux for the region. Examination of the boundary layer dynamical processes over the LIS would provide valuable information about the circulation, impacts of the nocturnal inversions over the region, and the features of the small-scale on-shore atmospheric flow ("sound breeze") that contribute to high measured O_3 levels along the CT coast.

Exploration of the various sources of O_3 precursors in the NJ/NYC metropolitan area, and sources over the LIS, would improve analysis of model results. Specific attention to the emissions sources contained within the non-road mobile inventory would assist with development of effective State Implementation Plans for the region. Additional examination of emissions from other over-water sources such as those classified in the class 1 and class 2 commercial marine vessels (ferries, fishing boats, etc.) [*McDill et al.*, 2017] would provide data for inventory comparison.

Finally, measurements of important VOCs like isoprene and propylene would significantly expand the community's understanding of the role VOCs have in producing O_3 over the LIS. Quantifying the isoprene flux for the region would provide data for inventory comparison and assist with estimating the biogenic VOC contribution to the area. As we have shown in the analysis in Chapter 4, isoprene is not the dominant VOC (at least during this sampling period) in the region, therefore we cannot assume the effects of anthropogenic VOCs are minimal compared to biogenic VOCs. Measurements of the most important VOCs to O_3 production (Based on the MIR/POCP scales) would allow policy makers to target the most important VOCs, and design effective attainment strategies.

Findings from this proposed field campaign in the NYC/LIS region would be applicable in other heavily populated coastal areas like Chicago and the Great Lakes region. Modeling analyses performed in this body of work have shown that large concentrations of O_3 are produced over near-coastal regions. Comparison of the model results to data gathered during the field mission described above would assist with determining if the models are correct, and if so, why this is the case.

5.3: Halogens and Ozone: Future Research

CMAQ often produces extremely high values of modeled AM8O_3 (> 140ppb) for some locations, especially along large bodies of water (Figure 21a and b from Chapter 3). These high values are much greater than measured surface O_3 in 2011 and are unrealistic. A possible source of this model/measurement discrepancy is the simplified representation of the chemistry within the chemical mechanism used by CMAQ. The CAMx model can use a variety of chemical mechanisms including the most recently released version of the Carbon Bond mechanism, CB6r4 [*Emery et al.*, 2016; *Yarwood et al.*, 2005]. Halogens such as iodine, chlorine, and bromine are known to impact O_3 production [*Chang et al.*, 2002]. However, halogen chemistry is limited in the chemical mechanisms used for regulatory air quality modeling.

One important halogen mechanism is the heterogeneous reaction of N_2O_5 on an aerosol particle to form either HNO_3 of $ClNO_2$ [*Riedel et al.*, 2013; *Riedel et al.*, 2014; *Sarwar et al.*, 2014; *Simon et al.*, 2009; *Thornton et al.*, 2010]. This is reaction with direct influence on the production of O_3 because HNO_3 is considered a reservoir species for NO_2, leading to its loss from the atmosphere. In mechanisms with no halogen

chemistry, N_2O_5 is assumed to always produce HNO_3, which accounts for approximately 50% of loss of NO_x from the atmosphere [*Riedel et al.*, 2012]. Appropriate reaction partitioning, including the formation of $ClNO_2$ from the heterogeneous reaction of N_2O_5 on a chlorine containing aerosol particle would reduce the loss of NO_x from the atmosphere via N_2O_5. This is because $ClNO_2$ photolyzes just after sunrise to release NO_2 and Cl back into the atmosphere, enhancing the impact of NO_2 on the production of O_3 [*Riedel et al.*, 2012; *Riedel et al.*, 2013; *Riedel et al.*, 2014; *Simon et al.*, 2009; *Thornton et al.*, 2010].

In addition to the research focusing on Cl and $ClNO_2$, studies have shown that bromine contributes to O_3 removal in the free troposphere [*Schmidt et al.*, 2016] and in the arctic surface regions [*Salawitch et al.*, 2010]. Concentrations of bromine compounds increase significantly with altitude, reflecting the longer lifetimes of these species and emphasizing their impact in the free troposphere [*Sherwen et al.*, 2016]. Analysis of aircraft and satellite observations during the NASA ARCTAS (Arctic Research of the Composition of the Troposphere from Aircraft and Satellites) mission combined with 3-D model simulations indicate the presence of significant amount of BrO in the stratosphere [*Choi et al.*, 2012; *Salawitch et al.*, 2010]. Studies such as these have helped improve the representation of tropospheric BrO in models.

In a study using the GEOS-Chem global model, *Sherwen et al.* [2016] found that inclusion of halogen chemistry accounts for ~20% of the total loss of O_3. Incorporating various halogen related O_3 production and loss processes into the regulatory air quality modeling using currently studies as guidance would improve ozone representation within the model, especially for near-coastal areas.

5.3.1: Implementation of Halogen Chemistry in Air Quality Models

A previous study by *Sarwar et al.* [2012] used a continental US CMAQ domain and added halogen chemistry to the CB05 mechanism to analyze the impact of $ClNO_2$ from N_2O_5 on air quality. They showed that monthly mean O_3 increases throughout the eastern US when heterogeneous production of $ClNO_2$ is included [*Sarwar et al.*, 2012]. This group also assessed the impact of heterogeneous production of $ClNO_2$ for the Northern Hemisphere [*Sarwar et al.*, 2014]. They found significant levels of $ClNO_2$ in winter over highly populated areas like Europe and China, contributing to increased O_3 levels. Inclusion of iodine chemistry and examination of ozone deposition velocities over near-coastal salt water will better represent modeled surface O_3 in air quality models [*Gantt et al.*, 2017; *Wong and Cheng*, 2008].

To accurately model halogens, emission inventories must be updated and/or developed. Point source emissions of HCl, Cl_2 and other chlorine sources are shown to be potentially large and are currently not well characterized in emissions inventories [*Crisp et al.*, 2014; *Lawler et al.*, 2011]. Concentrations of HCl tend to be highest in polluted coastal regions [*Crisp et al.*, 2014; *Keene et al.*, 2007], like the Chesapeake Bay and Long Island Sound because of elevated sea salt concentrations. Additionally, air polluted with HCl is advected towards the East Coast from source regions like the Midwest [*Keene et al.*, 2007]. HCl is the dominant form of chlorine in the troposphere, and besides direct emission from coal combustion, it is also produced via reaction of Cl with VOCs [*Hossaini et al.*, 2016]. Studies suggest that halogen emissions can be approximated based on the EPA's Toxic Release Inventory (TRI), and the most recent National Emissions Inventory (NEI), both developed by the US EPA. For context,

important sources of atmospheric Cl are industrial point sources, cooling towers, swimming pools, and sea salt [*Chang et al.*, 2002; *Riedel et al.*, 2013; *Spicer et al.*, 1998; *Tanaka et al.*, 2000].

Evaluation of air quality models with data is necessary to ensure model chemistry and emissions inventories are within reason. Various monitoring networks measure halogen species including the Clean Air Status and Trends Network (CASTNET), National Atmospheric Deposition Program (NADP), and observations from the Interagency Monitoring of Protected Visual Environments (IMPROVE) network. Observational campaigns conducted throughout the US like SENEX 2013 (https://www.esrl.noaa.gov/csd/projects/senex/) focused mostly over the southeast portion of the US, and the WINTER 2015 campaign centered mostly over the Mid-Atlantic US (https://www.esrl.noaa.gov/csd/groups/csd7/measurements/2015winter/) provide the opportunity to gain a better understanding of halogen chemistry under different geographic, seasonal and meteorological conditions.

Based on previous studies, implementation of sophisticated halogen chemistry in regulatory air quality models should reduce surface O_3 over large salt water bodies (iodine chemistry) and within the free troposphere, but a more localized increase in O_3 downwind from power plants and in some near-shore polluted regions due to chlorine chemistry is expected. Model results should be compared to available data to examine this hypothesis.

Appendix A

Table 5: Measured VOCs from RAMMPP aircraft campaign, corresponding rate constants for reaction with OH, and their Maximum Incremental Reactivity value.

VOCs	Rate Reaction (k_{OH})[a]	MIR[b]
Benzene	$k_{OH} = (2.3 \times 10^{-12}) \times e^{(-190/T)}$	0.72
Cyclohexane	$k_{OH} = (2.88 \times 10^{-17}) \times T^2 \times e^{(-309/T)}$	1.25
Cyclopentane	$k_{OH} = (2.67 \times 10^{-17}) \times e^{(-509/T)}$	2.39
Ethylbenzene	$k_{OH} = (7.00 \times 10^{-12})$	3.04
Isobutane	$k_{OH} = (5.4 \times 10^{-12}) \times e^{(-285/T)}$	1.23
Isopentane	$k_{OH} = (3.70 \times 10^{-12})$	1.45
Isoprene	$k_{OH} = (2.70 \times 10^{-11}) \times e^{(390/T)}$	10.61
Methylcyclohexane	$k_{OH} = (9.29 \times 10^{-12})$	1.70
Methylcyclopentane	$k_{OH} = (7.66 \times 10^{-12})$	2.19
Propane	$k_{OH} = (7.60 \times 10^{-12}) \times e^{(-585/T)}$	0.49
Propylene	$k_{OH} = (3.0 \times 10^{-11}) \times e^{(300/T)}$	11.66
Styrene	$k_{OH} = (5.80 \times 10^{-11})$	1.73
Toluene	$k_{OH} = (1.8 \times 10^{-12}) \times e^{(340/T)}$	4.00
cis-2-Butene	$k_{OH} = (1.10 \times 10^{-11}) \times e^{(487/T)}$	14.24
cis-2-Pentene	$k_{OH} = (6.54 \times 10^{-11})$	10.38
m-Ethyltoluene	$k_{OH} = (1.86 \times 10^{-11})$	7.39
o-Ethyltoluene	$k_{OH} = (1.19 \times 10^{-11})$	5.59
p-Ethyltoluene	$k_{OH} = (1.18 \times 10^{-11})$	4.44
mp-Xylene	$k_{OH} = (1.65 \times 10^{-11})$	7.80
o-Xylene	$k_{OH} = (1.36 \times 10^{-11})$	7.64
n-Butane	$k_{OH} = (9.8 \times 10^{-12}) \times e^{(-425/T)}$	1.15
n-Decane	$k_{OH} = (3.13 \times 10^{-17}) \times T^2 \times e^{(416/T)}$	0.68
n-Dodecane	$k_{OH} = (1.39 \times 10^{-11})$	0.55
n-Heptane	$k_{OH} = (1.59 \times 10^{-17}) \times T^2 \times e^{(478/T)}$	1.07

n-Hexane	$k_{OH} = (1.53 \times 10^{-17}) \times T^2 \times e^{(414/T)}$	1.24
n-Nonane	$k_{OH} = (2.51 \times 10^{-17}) \times T^2 \times e^{(447/T)}$	0.78
n-Octane	$k_{OH} = (2.76 \times 10^{-17}) \times T^2 \times e^{(378/T)}$	0.90
n-Pentane	$k_{OH} = (2.44 \times 10^{-17}) \times T^2 \times e^{(183/T)}$	1.31
n-Propylbenzene	$k_{OH} = (5.80 \times 10^{-12})$	2.03
n-Undecane	$k_{OH} = (1.29 \times 10^{-11})$	0.61
m-Diethylbenzene	$k_{OH} = (2.31 \times 10^{-11})$	7.10
p-Diethylbenzene	$k_{OH} = (1.43 \times 10^{-11})$	4.43
trans-2-Butene	$k_{OH} = (1.01 \times 10^{-11}) \times e^{(550/T)}$	15.16
trans-2-Pentene	$k_{OH} = (6.69 \times 10^{-11})$	10.56
123-Trimethylbenzene	$k_{OH} = (3.27 \times 10^{-11})$	11.97
124-Trimethylbenzene	$k_{OH} = (3.25 \times 10^{-11})$	8.87
135-Trimethylbenzene	$k_{OH} = (5.67 \times 10^{-11})$	11.76
1-Butene	$k_{OH} = (6.60 \times 10^{-12}) \times e^{(465/T)}$	9.73
1-Hexene	$k_{OH} = (3.70 \times 10^{-11})$	5.49
1-Pentene	$k_{OH} = (5.86 \times 10^{-12}) \times e^{(500/T)}$	7.21
224-Trimethylpentane	$k_{OH} = (2.09 \times 10^{-12}) \times e^{(140/T)}$	1.26
22-Dimethylbutane	$k_{OH} = (3.22 \times 10^{-11}) \times e^{(-781/T)}$	1.17
23-Dimethylbutane	$k_{OH} = (1.24 \times 10^{-17}) \times T^2 \times e^{(494/T)}$	0.97
22-Dimethylpentane	$k_{OH} = (5.20 \times 10^{-12})$	1.12
23-Dimethylpentane	$k_{OH} = (1.95 \times 10^{-11}) \times e^{(-330/T)}$	1.34
2-Methylhexane	$k_{OH} = (6.86 \times 10^{-12})$	1.19
2-Methylpentane	$k_{OH} = (5.30 \times 10^{-12})$	1.50
3-Methylpentane	$k_{OH} = (5.40 \times 10^{-12})$	1.80
3-Methylheptane	$k_{OH} = (6.30 \times 10^{-12})$	1.24
3-Methylhexane	$k_{OH} = (7.15 \times 10^{-12})$	1.61

[a] Reaction rates are from MCMv3.3.1 (http://mcm.leeds.ac.uk/MCM/)
[b] Maximum Incremental Reactivity (MIR) values are from [*Carter*, 2010b]

Appendix B

Table 6: The species used in the core Carbon Bond 05 (CB05) chemical mechanism. Species for the 16 added chemical reactions, the secondary organic aerosol formation, and chlorine mechanisms in the UMD CMAQ installation (CB05TUCl) are indicated with an *. (Core CB05 species are in Table 2-1 from *Yarwood et al.* [2005].)

Species Name	Description
NO	Nitric oxide
NO2	Nitrogen dioxide
O3	Ozone
O	Oxygen atom in the $O^3(P)$ electronic state
O1D	Oxygen atom in the $O^1(D)$ electronic state
OH	Hydroxyl radical
HO2	Hydroperoxy radical
H2O2	Hydrogen peroxide
NO3	Nitrate radical
N2O5	Dinitrogen pentoxide
HONO	Nitrous acid
HNO3	Nitric acid
PNA	Peroxynitric acid (HNO_4)
CO	Carbon monoxide
FORM	Formaldehyde
ALD2	Acetaldehyde
C2O3	Acetylperoxy radical
PAN	Peroxyacetyl nitrate
ALDX	Propionaldehyde and higher aldehydes
CXO3	C3 and higher acylperoxy radicals
PANX	C3 and higher peroxyacyl nitrates
XO2	NO to NO2 conversion from alkylperoxy (RO_2) radical
XO2N	NO to organic nitrate conversion from alkylperoxy (RO_2) radical
NTR	Organic nitrate (RNO_3)
ETOH	Ethanol
CH4	Methane
MEO2	Methylperoxy radical
MEOH	Methanol
MEPX	Methylhydroperoxide
FACD	Formic acid
ETHA	Ethane
ROOH	Higher organic peroxide

AACD	Acetic and higher carboxylic acids
PACD	Peroxyacetic and higher peroxycarboxylic acids
PAR	Paraffin carbon bond (C-C)
ROR	Secondary alkoxy radical
ETH	Ethene
OLE	Terminal olefin carbon bond (R-C=C)
IOLE	Internal olefin carbon bond (R-C=C-R)
ISOP	Isoprene
ISPD	Isoprene product (lumped methacrolein, methyl vinyl ketone, etc.)
TERP	Terpene
TOL	Toluene and other monoalkyl aromatics
XYL	Xylene and other polyalkyl aromatics
CRES	Cresols and higher molecular weight phenols
TO2	Toluene-hydroxyl radical adduct
OPEN	Aromatic ring opening product
CRO	Methylphenoxy radical
MGLY	Methylglyoxal and other aromatic products
SO2	Sulfur dioxide
SULF	Sulfuric acid (gaseous)
*BENZ	Benzene
*CAO2	Peroxy radical from aromatic degradation products
*CAT1	Methyl-catechols
*CRN2	Peroxy radical from nitro-cresol
*CRNO	Alkoxy radical from nitro-cresols
*CRON	Nitro-cresols
*CRPX	Nitro-cresol hydroperoxides
*HCO3	Adduct from HO2 + formaldehyde
*OPAN	Peroxyacyl nitrate (PAN compound) from OPO3
*OPO3	Peroxyacyl radical from OPEN
*SESQ	Sesquiterpene
*SULRXN	Counter species for aerosol from SO2
*TOLRXN	Counter species for aerosol from TOL
*XYLRXN	Counter species for aerosol from XYL
*ISOPRXN	Counter species for aerosol from ISOP
*TRPRXN	Counter species for aerosol from TERP
*TOLRO2	First generation products from TOL that react with NO and NO2
*XYLRO2	First generation products from XYL that react with NO and NO2
*BENZRO2	First generation products from BENZ that react with NO and NO2

*TOLNRXN	Counter species for aerosol from TOL (from reaction with NO)
*TOLHRXN	Counter species for aerosol from TOL (from reaction with HO2)
*XYLNRXN	Counter species for aerosol from XYL (from reaction with NO)
*XYLHRXN	Counter species for aerosol from XYL (from reaction with HO2)
*BNZNRXN	Counter species for aerosol from BENZ (from reaction with NO)
*BNXHRXN	Counter species for aerosol from BENZ (from reaction with HO2)
*SESQRXN	Counter species for aerosol from SESQ
Chlorine Mechanism Species	
*CL2	Molecular chlorine
*HOCL	Hypochlorous acid
*CL	Chlorine atom
*CLO	Chlorine monoxide
*FMCL	Formyl chloride (HC(O)Cl)
Constants	
H2	Molecular hydrogen fixed constant (0.56)
N2	Molecular nitrogen fixed constant (0.7808E+06)
O2	Molecular oxygen fixed constant (0.2095E+06)
AIR	Fixed constant (1.00E+06)
CH4	Methane fixed constant (1.85)

Table 7: Reactions used in the UMD CMAQ installation (CB05TUCl) that consist of the core CB05 chemical mechanism (156 reactions) with updates from the mechanism definitions file mech.def (16 additional reactions, 10 secondary organic aerosol formation reactions, 23 chlorine reactions). Any reactions with modifications from the core CB05 mechanism are indicated with an *. Interpretation of the rate expression is described below the table. (Core CB05 rates in Table 2-2 from *Yarwood et al.* [2005]).

Rxn	Reactants	Products	Rate Expression (k)
R1	NO2	NO + O	1.00 x j_{NO2} (SAPRC 99)
R2	O + O2 + M	O3 + M	6.00E-34^-2.4
R3	O3 + NO	NO2	3.00E-12 @ 1500
R4	O + NO2	NO	5.60E-12 @ -180
R5	O + NO2	NO3	2.50E-31^-1.8 & 2.20E-11^-0.7
R6	O + NO	NO2	9.00E-32^-1.5 & 3.00E-11
R7	NO2 + O3	NO3	1.20E-13 @ 2450
R8	O3	O	1.00 x $j_{O3(O3P)}$ (IUPAC 05)
R9	O3	O1D	1.00 x $j_{O3(O1D)}$ (IUPAC 05)
R10	O1D + M	O + M	2.10E-11 @ -102
R11	O1D + H2O	2*OH	2.20E-10
R12	O3 + OH	HO2	1.70E-12 @ 940
R13	O3 + HO2	OH	1.00E-14 @ 490
R14	NO3	NO2 + O	1.00 x $j_{NO3(NO2)}$ (SAPRC99)
R15	NO3	NO	1.00 x $j_{NO3(NO)}$ (SAPRC99)
R16	NO3 + NO	2*NO2	1.50E-11 @ -170
R17	NO3 + NO2	NO + NO2	4.50E-14 @ 1260
R18	NO3 + NO2	N2O5	2.00E-30^-4.4 & 1.40E-12^-0.7
*R19	N2O5 + H2O	2*HNO3	1.00E-22 (IUPAC 10)
*R20	N2O5 + H2O + H2O	2*HNO3	0.00 (IUPAC 10)
R21	N2O5	NO3 + NO2	1.0E-03^-3.5 @ 11000 & 9.70E14^0.1 @ 11080 & 0.45 & 1.0
R22	NO + NO + O2	2*NO2	3.30E-39 @ -530
R23	NO + NO2 + H2O	2*HONO	5.00E-40

R24	NO + OH	HONO	7.00E-31^-2.6 & 3.60E-11^-0.1
R25	HONO	NO + OH	1.00 x j_{HONO} (IUPAC 05)
R26	OH + HONO	NO2	1.80E-11 @ 390
R27	HONO + HONO	NO + NO2	1.00E-20
R28	NO2 + OH	HNO3	2.00E-30^-3.0 & 2.50E-11
R29	OH + HNO3	NO3	%2 2.4E-14 @ -460 & 2.70E-17 @ -2199 & 6.50E-34 @ -1335
R30	HO2 + NO	OH + NO2	3.50E-12 @ -250
R31	HO2 + NO2	PNA	1.80E-31^-3.2 & 4.70E-12 & 0.6
R32	PNA	HO2 + NO2	4.10E-5 @ 10650 & 4.80E15 @ 11170 & 0.6
R33	OH + PNA	NO2	1.30E-12 @ -380
R34	HO2 + HO2	H2O2	%3 2.3E-13 @ -600 & 1.70E-33 @ -1000
R35	HO2 + HO2 + H2O	H2O2	%3 3.22E-34 @ -2800 & 2.38E-54 @ -3200
R36	H2O2	2*OH	1.00 x j_{H2O2} (SAPRC99)
R37	OH + H2O2	HO2	2.90E-12 @ 160
R38	O1D + H2	OH + HO2	1.10E-10
R39	OH + H2	HO2	5.50E-12 @ 2000
R40	OH + O	HO2	2.20E-11 @ -120
R41	OH + OH	O	4.20E-12 @ 240
R42	OH + OH	H2O2	6.90E-31^-1.0 & 2.60E-11^0
R43	OH + HO2		4.80E-11 @ -250
R44	HO2 + O	OH	3.00E-11 @ -200
R45	H2O2 + O	OH + HO2	1.40E-12 @ 2000
R46	NO3 + O	NO2	1.00E-11
R47	NO3 + OH	HO2 + NO2	2.20E-11
R48	NO3 + HO2	HNO3	3.50E-12
R49	NO3 + O3	NO2	1.00E-17
R50	NO3 + NO3	2*NO2	8.50E-13 @ 2450
R51	PNA	0.610*HO2 + 0.610*NO2 + 0.390*OH + 0.390*NO3	1.00 x $j_{HO2(NO2)}$ (IUPAC 05)
R52	HNO3	OH + NO2	1.00 x j_{HO3} (IUPAC 05)

R53	N2O5	NO2 + NO3	1.00 x j_{N2O5} (IUPAC05)
R54	XO2 + NO	NO2	2.60E-12 @ -365
R55	XO2N + NO	NTR	2.60E-12 @ -365
R56	XO2 + HO2	ROOH	7.50E-13 @ -700
R57	XO2N + HO2	ROOH	7.50E-13 @ -700
R58	XO2 + XO2		6.80E-14
R59	XO2N + XO2N		6.80E-14
R60	XO2 + XO2N		6.80E-14
R61	NTR + OH	HNO3 + HO2 + 0.330*FORM + 0.330*ALD2 + 0.330*ALDX - 0.660*PAR	5.90E-13 @ 360
R62	NTR	NO2 + HO2 + 0.330*FORM + 0.330*ALD2 + 0.330*ALDX - 0.660*PAR	1.00 x j_{NTR} (IUPAC 05 isopropyl nitrate)
***R62**	**NTR**	*Adjusted binned values for the absorption cross section to be more representative of NTR species	*NTR adjustment in c3 Science
R63	ROOH + OH	XO2 + 0.500*ALD2 + 0.500*ALDX	3.01E-12 @ -190
R64	ROOH	OH + HO2 + 0.500*ALD2 + 0.500*ALDX	1.00 x j_{COOH} (SAPRC99)
R65	OH + CO	HO2	%3 1.44E-13 @ 0.0 & 3.43E-33 @ 0.0
R66	OH + CH4	MEO2	2.45E-12 @ 1775
R67	MEO2 + NO	FORM + HO2 + NO2	2.80E-12 @ -300
R68	MEO2 + HO2	MEPX	4.10E-13 @ -750
R69	MEO2 + MEO2	1.370*FORM + 0.740*HO2 + 0.630*MEOH	9.50E-14 @ -390
R70	MEPX + OH	0.700*MEO2 + 0.300*XO2 + 0.300*HO2	3.80E-12 @ -200
R71	MEPX	FORM + HO2 + OH	1.00 x j_{COOH} (SAPRC99)
R72	MEOH + OH	FORM + HO2	7.30E-12 @ 620
R73	FORM + OH	HO2 + CO	9.00E-12
*R74	FORM	2*HO2 + CO	1.00 x j_{HCHO}

			(SAPRC99)
R75	FORM	CO	1.00 x j_{HCHO} (SAPRC99)
R76	FORM + O	OH + HO2 + CO	3.40E-11 @ 1600
R77	FORM + NO3	HNO3 + HO2 + CO	5.80E-16
R78	FORM + HO2	HCO3	9.70E-15 @ -625
R79	HCO3	FORM + HO2	2.40E+12 @ 7000
R80	HCO3 + NO	FACD + NO2 + HO2	5.60E-12
R81	HCO3 + HO2	MEPX	5.60E-15 @ -2300
R82	FACD + OH	HO2	4.00E-13
R83	ALD2 + O	C2O3 + OH	1.80E-11 @ 1100
R84	ALD2 + OH	C2O3	5.60E-12 @ -270
R85	ALD2 + NO3	C2O3 + HNO3	1.40E-12 @ 1900
R86	ALD2	MEO2 + CO + HO2	1.00 x $j_{CCHO(R)}$ (SAPRC99)
R87	C2O3 + NO	MEO2 + NO2	8.10E-12 @ -270
R88	C2O3 + NO2	PAN	2.70E-28^-7.1 & 1.20E-11^-0.9 & 0.3
R89	PAN	C2O3 + NO2	4.90E-3 @ 12100 & 5.40E16 @ 13830 & 0.3
R90	PAN	C2O3 + NO2	1.00 x j_{PAN} (IUPAC 05)
R91	C2O3 + HO2	0.800*PACD + 0.200*AACD + 0.200*O3	4.30E-13 @ -1040
R92	C2O3 + MEO2	0.900*MEO2 + 0.900*HO2 + FORM + 0.100*AACD	2.00E-12 @ -500
R93	C2O3+XO2	0.900*MEO2 + 0.100*AACD	4.40E-13 @ -1070
R94	C2O3 + C2O3	2*MEO2	2.90E-12 @ -500
R95	PACD + OH	C2O3	4.00E-13 @ -200
*R96	PACD	MEO2 + OH	1.00 x j_{PACD} (CB05 peroxyacetic acid)
R97	AACD + OH	MEO2	4.00E-13 @ -200
R98	ALDX + O	CXO3 + OH	1.30E-11 @ 870
R99	ALDX + OH	CXO3	5.10E-12 @ -405

R100	ALDX + NO3	CXO3 + HNO3	6.50E-15
R101	ALDX	MEO2 + CO + HO2	1.00 x j_{C2CHO} (SAPRC99)
R102	CXO3 + NO	ALD2 + NO2 + HO2 + XO2	6.70E-12 @ -340
R103	CXO3 + NO2	PANX	2.70E-28^-7.1 & 1.20E-11^-0.9 & 0.3
R104	PANX	CXO3 + NO2	4.90E-3 @ 12100 & 5.40E16 @ 13830 & 0.3
R105	PANX	CXO3 + NO2	1.00 x j_{PAN} (IUPAC 05)
R106	PANX + OH	ALD2 + NO2	3.00E-13
R107	CXO3 + HO2	0.800*PACD + 0.200*AACD + 0.200*O3	4.30E-13 @ -1040
R108	CXO3 + MEO2	0.900*ALD2 + 0.900*XO2 + HO2 + 0.100*AACD + 0.100*FORM	2.00E-12 @ -500
R109	CXO3 + XO2	0.900*ALD2 + 0.100*AACD	4.40E-13 @ -1070
R110	CXO3 + CXO3	2*ALD2 + 2*XO2 + 2*HO2	2.90E-12 @ -500
R111	CXO3 + C2O3	MEO2 + XO2 + HO2 + ALD2	2.90E-12 @ -500
R112	PAR + OH	0.870*XO2 + 0.130*XO2N + 0.110*HO2 + 0.060*ALD2 – 0.110*PAR + 0.760*ROR + 0.050*ALDX	8.10E-13
R113	ROR	0.960*XO2 + 0.600*ALD2 + 0.940*HO2 – 2.100*PAR + 0.040*XO2N + 0.020*ROR + 0.500*ALDX	1.00E+15 @ 8000
R114	ROR	HO2	1.60E+03
R115	ROR + NO2	NTR	1.50E-11
R116	O + OLE	0.200*ALD2 + 0.300*ALDX + 0.300*HO2 + 0.200*XO2 + 0.200*CO + 0.200*FORM + 0.010*XO2N + 0.200*PAR + 0.100*OH	1.00E-11 @ 280
R117	OH + OLE	0.800*FORM + 0.330*ALD2 + 0.620*ALDX + 0.800*XO2 + 0.950*HO2 – 0.700*PAR	3.20E-11
R118	O3 + OLE	0.180*ALD2 + 0.740*FORM + 0.320*ALDX + 0.220*XO2	6.50E-15 @ 1900

		+ 0.100*OH + 0.330*CO + 0.440*HO2 – PAR	
R119	NO3 + OLE	NO2 + FORM + 0.910*XO2 + 0.090*XO2N + 0.560*ALDX + 0.350*ALD2 – PAR	7.00E-13 @ 2160
R120	O + ETH	FORM + 1.700*HO2 + CO + 0.700*XO2 + 0.300*OH	1.04E-11 @ 792
R121	OH + ETH	XO2 + 1.560*FORM + 0.220*ALDX + HO2	1.00E-28^-0.8 & 8.80E-12
R122	O3 + ETH	FORM + 0.630*CO + 0.130*HO2 + 0.130*OH + 0.370*FACD	1.20E-14 @ 2630
R123	NO3 + ETH	NO2 + XO2 + 2.0*FORM	3.30E-12 @ 2880
R124	IOLE + O	1.240*ALD2 + 0.660*ALDX + 0.100*HO2 + 0.100*XO2 + 0.100*CO + 0.100*PAR	2.30E-11
R125	IOLE + OH	1.300*ALD2 + 0.700*ALDX + HO2 + XO2	1.00E-11 @ -550
R126	IOLE + O3	0.650*ALD2 + 0.350*ALDX + 0.250*FORM + 0.250*CO + 0.500*O + 0.500*OH + 0.500*HO2	8.40E-15 @ 1100
R127	IOLE + NO3	1.180*ALD2 + 0.640*ALDX + HO2 + NO2	9.6E-13 @ 270
*R128	TOL + OH	0.280*HO2 + 0.100*XO2 + 0.180*CRES + 0.650*TO2 + 0.072*OH + 1.0*TOLRO2	1.80E-12 @ -355
*R129	TO2 + NO	0.860*NO2 + 1.20*HO2 + 0.860*OPEN + 0.140*NTR + 0.52*MGLY + 0.336*FORM + 0.336*CO	2.70E-12 @ -360
*R130	TO2 + HO2		1.90E-13 @ -1300
*R131	OH + CRES	0.060*CRO + 0.120*XO2 + 1.120*HO2 + 0.130*OPEN + 0.732*CAT1 + 0.060*CO + 0.060*XO2N + 0.060*FORM	1.70E-12 @ -950
*R132	CRES + NO3	0.300*CRO + HNO3 + 0.600*XO2 + 0.360*HO2 + 0.480*ALDX + 0.240*FORM + 0.240*MGLY + 0.120*OPEN + 0.100*XO2N + 0.240*CO	1.40E-11
*R133	CRO + NO2	CRON	2.10E-12
R134	CRO + HO2	CRES	5.50E-12

*R135	CRON + OH	CRNO	1.53E-12
*R136	CRON + NO3	CRNO + HNO3	3.80E-12
*R137	CRNO + NO2	2.0*NTR	2.10E-12
*R138	CRNO + O3	CRN2	2.86E-13
*R139	CRN2 + NO	CRNO + NO2	2.54E-12 @ -360
*R140	CRN2 + HO2	CRPX	2.40E-13 @ -1300
*R141	CRPX	CRNO + OH	0.01 x j_{NO2} (SAPRC99)
*R142	CRPX + OH	CRN2	1.90E-12 @ -190
*R143	OPEN	OPO3 + HO2 + CO	0.04 x j_{NO2} (SAPRC99)
*R144	OPEN + OH	0.600*OPO3 + 0.400*CAO2	4.40E-11
*R145	OPEN + O3	0.030*ALDx + 0.620*OPO3 + 0.700*FORM + 0.030*XO2 + 0.690*CO + 0.080*OH + 0.760*HO2 + 0.200*MGLY	5.40E-17 @ 500
*R146	OPEN + NO3	OPO3 + HNO3	3.80E-12
*R147	CAT1 + OH	CAO2	7.00E-11
*R148	CAT1 + NO3	CRO + HNO3	1.70E-10
*R149	CAO2 + NO	0.860*NO2 + 1.200*HO2 + 0.344*FORM + 0.344*CO + 0.140*NTR	2.54E-12 @ -360
*R150	CAO2 + HO2		2.40E-13 @ -1300
*R151	OPO3 + NO	NO2 + XO2 + HO2 + ALDX	1.10E-11
*R152	OPO3 + NO2	OPAN	1.10E-11
*R153	OPAN	OPO3 + NO2	1.00E-04
*R154	OH + XYL	0.700*HO2 + 0.500*XO2 + 0.200*CRES + 0.800*MGLY + 1.100*PAR + 0.300*TO2 + 1.0*XYLRO2	1.7E-11 @ -116
*R155	OH + MGLY	XO2 + C2O3	1.80E-11
R156	MGLY	C2O3 + HO2 + CO	1.00 x j_{MGLY} (IUPAC 05)

R157	O + ISOP	0.750*ISPD + 0.500*FORM + 0.250*XO2 + 0.250*HO2 + 0.250*CXO3 + 0.250*PAR	3.60E-11
R158	OH + ISOP	0.912*ISPD + 0.629*FORM + 0.991*XO2 + 0.912*HO2 + 0.088*XO2N	2.54E-11 @ -407.6
R159	O3 + ISOP	0.650*ISPD + 0.600*FORM + 0.200*XO2 + 0.066*HO2 + 0.266*OH + 0.200*CXO3 + 0.150*ALDX + 0.350*PAR + 0.066*CO	7.86E-15 @ 1912
R160	NO3 + ISOP	0.200*ISPD + 0.800*NTR + XO2 + 0.800*HO2 + 0.200*NO2 + 0.800*ALDX + 2.40*PAR	3.03E-12 @ 448
R161	OH + ISPD	1.565*PAR + 0.167*FORM + 0.713*XO2 + 0.503*HO2 + 0.334*CO + 0.168*MGLY + 0.252*ALD2 + 0.210*C2O3 + 0.250*CXO3 + 0.120*ALDX	3.36E-11
R162	O3 + ISPD	0.114*C2O3 + 0.150*FORM + 0.850*MGLY + 0.154*HO2 + 0.268*OH + 0.064*XO2 + 0.020*ALD2 + 0.360*PAR + 0.225*CO	7.10E-18
R163	NO3 + ISPD	0.357*ALDX + 0.282*FORM + 1.282*PAR + 0.925*HO2 + 0.643*CO + 0.850*NTR + 0.075*CXO3 + 0.075*XO2 + 0.150*HNO3	1.00E-15
R164	ISPD	0.333*CO + 0.067*ALD2 + 0.900*FORM + 0.832*PAR + 1.033*HO2 + 0.700*XO2 + 0.967*C2O3	0.0036 x $j_{ACROLEIN}$ (SAPRC99)
*R165	TERP + O	0.150*ALDX + 5.12*PAR + TRPRXN	3.60E-11
*R166	TERP + OH	0.750*HO2 + 1.250*XO2 + 0.250*XO2N + 0.280*FORM + 1.66*PAR + 0.470*ALDX + TRPRXN	1.50E-11 @ -449
*R167	TERP + O3	0.570*OH + 0.070*HO2 + 0.760*XO2 + 0.180*XO2N + 0.240*FORM + 0.001*CO + 7.000*PAR + 0.210*ALDX + 0.390*CXO3 + TRPRXN	1.20E-15 @ 821

*R168	TERP + NO3	0.470*NO2 + 0.280*HO2 + 1.030*XO2 + 0.250*XO2N + 0.470*ALDX + 0.530*NTR + TRPRXN	3.70E-12 @ -175
*R169	SO2 + OH	SULF + HO2 + SULRXN	3.30E-31^-4.3 & 1.60E-12^0.0
R170	OH + ETOH	HO2 + 0.900*ALD2 + 0.050*ALDX + 0.100*FORM + 0.100*XO2	6.90E-12 @ 230
R171	OH + ETHA	0.991*ALD2 + 0.991*XO2 + 0.009*XO2N + HO2	8.70E-12 @ 1070
R172	NO2 + ISOP	0.200*ISPD + 0.800*NTR + XO2 + 0.800*HO2 + 0.200*NO + 0.800*ALDX + 2.400*PAR	1.50E-19
		Chlorine Mechanism	
CL1	CL2	2.00*CL	1.00 x j_{Cl} (IUPAC 05)
CL2	HOCL	OH + CL	1.00 x j_{HOCl} (IUPAC 05)
CL3	CL + O3	CLO	2.30E-11 @ 200
CL4	CLO + CLO	0.300*CL2 + 1.400*CL	1.63E-14
CL5	CLO + NO	CL + NO2	6.40E-12 @ -290
CL6	CLO + HO2	HOCL	2.70E-12 @ -220
CL7	OH + FMCL	CL + CO	5.00E-13
CL8	FMCL	CL + CO + HO2	1.00 x j_{FMCL} (IUPAC 05)
CL9	CL + CH4	HCL + MEO2	6.60E-12 @ 1240
CL10	CL + PAR	HCL + 0.870*XO2 + 0.130*XO2N + 0.110*HO2 + 0.060*ALD2 + 0.110*PAR + 0.760*ROR + 0.050*ALDX	5.00E-11
CL11	CL + ETHA	HCL + 0.991*ALD2 + 0.991*XO2 + 0.009*XO2N + HO2	8.30E-11 @ 100
CL12	CL + ETH	FMCL + 2.0-*XO2 + 1.00*HO2 + 1.00*FORM	1.07E-11
CL13	CL + OLE	FMCL + 0.330*ALD2 + 0.670*ALDX + 2.00*XO2 + 1.00*HO2 – 1.00*PAR	2.50E-10
CL14	CL + IOLE	0.300*HCL + 0.700*FMCL + 0.450*ALD2 + 0.550*ALDX + 0.300*OLE + 0.300*PAR + 1.70*XO2 + 1.00*HO2	3.50E-10

CL15	CL + ISOP	0.150*HCL + 1.00*HO2 + 1.00*HO2 + 0.850*FMCL + 1.00*ISPD	4.30E-10
CL16	CL + FORM	HCL + 1.00*HO2 + 1.00*CO	8.20E-11 @ 34
CL17	CL + ALD2	HCL + 1.00*C2O3	7.90E-11
CL18	CL + ALDX	HCL + 1.00*CXO3	1.30E-10
CL19	CL + MEOH	HCL + 1.00*HO2 + 1.00*FORM	5.50E-11
CL20	CL + ETOH	HCL + 1.00*HO2 + 1.00*ALD2	8.20E-11 @ -45
CL21	HCL + OH	CL	6.58E-13^1.16 @ -58
CL22	CL + TOL	HCL + 0.880*XO2 + 0.880*HO2 + 0.12*XO2N	6.10E-11
CL23	CL + XYL	HCL + 0.840*XO2 + 0.840*HO2 + 0.160*XO2N	1.20E-10
		Secondary Aerosol Mechanism	
SA1	TOLRO2 + NO	NO + TOLRXN	2.70E-12 @ -360
SA2	TOLRO2 + HO2	HO2 + TOLHRXN	1.90E-13 @ -1300
SA3	XYLRO2 + NO	NO + XYLNRXN	2.70E-12 @ -360
SA4	XYLRO2 + HO2	HO2 + XYLRXN	1.90E-13 @ -1300
SA5	BENZ + OH	OH + 1.00*BENZRO2	2.47E-12 @ 206
SA6	BENZRO2 + NO	NO + BNZNRXN	2.70E-12 @ -360
SA7	BENZRO2 + HO2	HO2 + BNZHRXN	1.90E-13 @ -1300
SA8	SESQ + O3	O3 + SESQRXN	1.16E-14
SA9	SESQ + OH	OH + SESQRXN	1.97E-10
SA10	SESQ + NO3	NO3 + SESQRXN	1.90E-11

Bibliography

Altshuiler, A. P. (1976), Regional Transport and Transformation of Sulfur Dioxide to Sulfates in the U. S, *Journal of the Air Pollution Control Association*, *26*(4), 318-325, doi:10.1080/00022470.1976.10470256.

Anderson, D. C., et al. (2014), Measured and modeled CO and NOy in DISCOVER-AQ: An evaluation of emissions and chemistry over the eastern US, *Atmospheric Environment*, *96*, 78-87, doi:10.1016/j.atmosenv.2014.07.004.

Angevine, W. M., M. Tjernström, and M. Žagar (2006), Modeling of the Coastal Boundary Layer and Pollutant Transport in New England, *Journal of Applied Meteorology and Climatology*, *45*(1), 137-154, doi:10.1175/jam2333.1.

Atkinson, R. (2000), Atmospheric chemistry of VOCs and NOx, *Atmospheric Environment*, *34*(12-14), 2063-2101, doi:Doi 10.1016/S1352-2310(99)00460-4.

Avery, R. J. (2006), Reactivity-Based VOC Control for Solvent Products: More Efficient Ozone Reduction Strategies, *Environmental Science & Technology*, *40*, 4845-4850.

Bash, J. O., K. R. Baker, and M. R. Beaver (2016), Evaluation of improved land use and canopy representation in BEIS v3.61 with biogenic VOC measurements in California, *Geoscientific Model Development*, *9*(6), 2191-2207, doi:10.5194/gmd-9-2191-2016.

Bell, M. L., R. Goldberg, C. Hogrefe, P. L. Kinney, K. Knowlton, B. Lynn, J. Rosenthal, C. Rosenzweig, and J. A. Patz (2007), Climate change, ambient ozone, and health in 50 US cities, *Climatic Change*, *82*(1-2), 61-76, doi:10.1007/s10584-006-9166-7.

Bell, M. L., R. D. Peng, and F. Dominici (2006), The Exposure-Resoinse Curve for Ozone and Risk of Mortality and the Adequacy of Current Ozone Regulations, *Environmental Health Perspectives*, *114*(4), 532-536.

Bergin, M. S., J.-S. Shih, A. J. Krupnick, J. W. Boylan, J. G. Wilkinson, M. T. Odman, and A. G. Russell (2007), Regional Air Quality: Local and Interstate Impacts of NOxand SO2Emissions on Ozone and Fine Particulate Matter in the Eastern United States, *Environmental Science & Technology*, *41*(13), 4677-4689, doi:10.1021/es062302s.

Bloomer, B. J., J. W. Stehr, C. A. Piety, R. J. Salawitch, and R. R. Dickerson (2009), Observed relationships of ozone air pollution with temperature and emissions, *Geophysical Research Letters*, *36*(9), doi:Artn L09803 10.1029/2009gl037308.

Boersma, K. F., H. J. Eskes, and E. J. Brinksma (2004), Error analysis for tropospheric NO2 retrieval from space, *Journal of Geophysical Research-Atmospheres*, *109*(D4), n/a-n/a, doi:10.1029/2003jd003962.

Boersma, K. F., et al. (2011), An improved tropospheric NO2 column retrieval algorithm for the Ozone Monitoring Instrument, *Atmospheric Measurement Techniques*, *4*(9), 1905-1928, doi:10.5194/amt-4-1905-2011.

Boersma, K. F., et al. (2007), Near-real time retrieval of tropospheric NO2 from OMI, *Atmospheric Chemistry and Physics*, *7*(8), 2103-2118.

Bovensmann, H., J. P. Burrows, M. Buchwitz, J. Frerick, S. Noël, V. V. Rozanov, K. V. Chance, and A. P. H. Goede (1999), SCIAMACHY: Mission Objectives and Measurement Modes, *Journal of the Atmospheric Sciences*, *56*(2), 127-150, doi:10.1175/1520-0469(1999)056<0127:Smoamm>2.0.Co;2.

Bucsela, E. J., E. A. Celarier, M. O. Wenig, J. F. Gleason, J. P. Veefkind, K. F. Boersma, and E. J. Brinksma (2006), Algorithm for NO/sub 2/ vertical column retrieval from the ozone monitoring instrument, *IEEE Transactions on Geoscience and Remote Sensing*, *44*(5), 1245-1258, doi:10.1109/tgrs.2005.863715.

Bucsela, E. J., N. A. Krotkov, E. A. Celarier, L. N. Lamsal, W. H. Swartz, P. K. Bhartia, K. F. Boersma, J. P. Veefkind, J. F. Gleason, and K. E. Pickering (2013), A new stratospheric and tropospheric NO2 retrieval algorithm for nadir-viewing satellite instruments: applications to OMI, *Atmospheric Measurement Techniques*, *6*(10), 2607-2626, doi:10.5194/amt-6-2607-2013.

Burrows, J. P., et al. (1999), The Global Ozone Monitoring Experiment (GOME): Mission Concept and First Scientific Results, *Journal of the Atmospheric Sciences*, *56*, 151-175.

Buzcu, B., and P. Fraser (2006), Source Identification and Apportionment of Volatile Organic Compounds in Houston, TX, *Atmospheric Environment*, *40*, 2385-2400.

Byun, D., and K. L. Schere (2006), Review of the governing equations, computational algorithms, and other components of the models-3 Community Multiscale Air Quality (CMAQ) modeling system, *Applied Mechanics Reviews*, *59*(1-6), 51-77, doi:10.1115/1.2128636.

Canty, T. P., L. Hembeck, T. P. Vinciguerra, D. C. Anderson, D. L. Goldberg, S. F. Carpenter, D. J. Allen, C. P. Loughner, R. J. Salawitch, and R. R. Dickerson (2015), Ozone and NOx chemistry in the eastern US: evaluation of CMAQ/CB05 with satellite (OMI) data, *Atmospheric Chemistry and Physics*, *15*(19), 10965-10982, doi:10.5194/acp-15-10965-2015.

Carter, W. P. L. (1994), Development of Ozone Reactivity Scales for Volatile Organic Compounds, *Journal of Air & Waste Management Association*, *44*(7), 881-899, doi:10.1080/1073161X.1994.10467290.

Carter, W. P. L. (2010a), Development of the SAPRC-07 Chemical Mechanism, *Atmospheric Environment*, *44*, 5324-5335.

Carter, W. P. L. (2010b), Updated Maximum Incremental Reactivity Scale and Hydrocarbon Bin Reactivities for Regulatory Applications, *California Air Resources Board Contract 07-339*, https://www.arb.ca.gov/regact/2009/mir2009/mir2010.pdf.

Castellanos, P., L. T. Marufu, B. G. Doddridge, B. F. Taubman, J. J. Schwab, J. C. Hains, S. H. Ehrman, and R. R. Dickerson (2011), Ozone, oxides of nitrogen, and carbon monoxide during pollution events over the eastern United States: An evaluation of emissions and vertical mixing, *Journal of Geophysical Research-Atmospheres*, *116*(D16), doi:Artn D16307 10.1029/2010jd014540.

Castellanos, P., J. W. Stehr, R. R. Dickerson, and S. H. Ehrman (2009), The sensitivity of modeled ozone to the temporal distribution of point, area, and mobile source emissions in the eastern United States, *Atmospheric Environment*, *43*(30), 4603-4611, doi:10.1016/j.atmosenv.2009.05.045.

Chang, S., E. McDonald-Buller, Y. Kimura, G. Yarwood, J. Neece, M. Russell, P. Tanaka, and D. Allen (2002), Sensitivity of urban ozone formation to chlorine emission estimates, *Atmospheric Environment*, *36*(32), 4991-5003, doi:http://dx.doi.org/10.1016/S1352-2310(02)00573-3.

Chen, D., X. Wang, Y. Li, J. Lang, Y. Zhou, X. Guo, and Y. Zhao (2017a), High-spatiotemporal-resolution ship emission inventory of China based on AIS data in 2014, *Sci Total Environ*, *609*, 776-787, doi:10.1016/j.scitotenv.2017.07.051.

Chen, D., N. Zhao, J. Lang, Y. Zhou, X. Wang, Y. Li, Y. Zhao, and X. Guo (2017b), Contribution of ship emissions to the concentration of PM2.5: A comprehensive study using AIS data and WRF/Chem model in Bohai Rim Region, China, *Sci Total Environ*, *610-611*, 1476-1486, doi:10.1016/j.scitotenv.2017.07.255.

Chen, D., Y. Zhao, P. Nelson, Y. F. Li, X. Wang, Y. Zhou, J. Lang, and X. Guo (2016), Estimating ship emissions based on AIS data for port of Tianjin, China, *Atmospheric Environment*, *145*, 10-18, doi:10.1016/j.atmosenv.2016.08.086.

Chen, G., et al. (2005), An investigation of the chemistry of ship emission plumes during ITCT 2002, *Journal of Geophysical Research*, *110*(D10), doi:10.1029/2004jd005236.

Chen, G., H. Xue, G. Feingold, and X. Zhou (2012), Vertical transport of pollutants by shallow cumuli from large eddy simulations, *Atmospheric Chemistry and Physics*, *12*(23), 11319-11327, doi:10.5194/acp-12-11319-2012.

Ching, J. K. S., and A. J. Alkezweeny (1986), Tracer Study of Vertical Exchange by Cumulus Clouds, *Journal of Climate and Applied Meteorology*, *25*(11), 1702-1711, doi:10.1175/1520-0450(1986)025<1702:Tsoveb>2.0.Co;2.

Choi, S., et al. (2012), Analysis of satellite-derived Arctic tropospheric BrO columns in conjunction with aircraft measurements during ARCTAS and ARCPAC, *Atmospheric Chemistry and Physics*, *12*(3), 1255-1285, doi:10.5194/acp-12-1255-2012.

Cleary, P. A., et al. (2015), Ozone distributions over southern Lake Michigan: comparisons between ferry-based observations, shoreline-based DOAS observations and model forecasts, *Atmospheric Chemistry and Physics*, *15*(9), 5109-5122, doi:10.5194/acp-15-5109-2015.

Cleveland, W. S., and T. E. Graedel (1979), Photochemical air pollution in the northeast United States, *Science*, *204*(4399), 1273-1278, doi:10.1126/science.204.4399.1273.

CMAS (2014a), CMAQ version 5.0.2 (April 2014 release) Technical Documentation, https://www.airqualitymodeling.org/index.php/CMAQ_version_5.0.2_(April_2014_release)_Technical_Documentation.

CMAS (2014b), SMOKE v3.6 User's Manual, edited, The Institute for the Environment, University of North Carolina, Chapel Hill.

CMAS (2015), MCIP 4.3 Documentation, edited, The Institute for the Environment, University of North Carolina, Chapel Hill.

Cohan, D. S., and R. Chen (2014), Modeled and observed fine particulate matter reductions from state attainment demonstrations, *J Air Waste Manag Assoc*, *64*(9), 995-1002, doi:10.1080/10962247.2014.905509.

Cohen, A. J., et al. (2017), Estimates and 25-year Trends of the GLobal Burden of Disease Attributed to Ambient Air Pollution: An Analysis of Data from the Global Burden of Diseases Study 2015, *The Lancet*, *389*, 1907-1918.

Cohen, A. J., et al. (2005), The global burden of disease due to outdoor air pollution, *J Toxicol Environ Health A*, *68*(13-14), 1301-1307, doi:10.1080/15287390590936166.

Cooper, D. A. (2003), Exhaust emissions from ships at berth, *Atmospheric Environment*, *37*(27), 3817-3830, doi:10.1016/S1352-2310(03)00446-1.

Cooper, O. R., R.-S. G, D. Tarasick, T. Leblanc, and C. Sweeney (2012), Long-term Ozone Trends at Rural Ozone Monitoring Sites Across the United States, 1990-2010, *Journal of Geophysical Research*, *117*(D22307).

Corbett, J. J., and H. W. Koehler (2003), Updated emissions from ocean shipping, *Journal of Geophysical Research-Atmospheres*, *108*(D20), doi:Artn 4650 10.1029/2003jd003751.

Corbett, J. J., J. J. Winebrake, E. H. Green, P. Kasibhatla, V. Eyring, and A. Lauer (2007), Mortality from ship emissions: a global assessment, *Environ Sci Technol*, *41*(24), 8512-8518, doi:10.1021/es071686z.

Crisp, T. A., B. M. Lerner, E. J. Williams, P. K. Quinn, T. S. Bates, and T. H. Bertram (2014), Observations of gas phase hydrochloric acid in the polluted marine boundary layer, *Journal of Geophysical Research: Atmospheres*, *119*(11), 6897-6915, doi:10.1002/2013JD020992.

Davis, D. D., G. Grodzinsky, P. Kasibhatla, J. Crawford, G. Chen, S. Liu, A. Bandy, D. Thornton, H. Guan, and S. Sandholm (2001), Impact of ship emissions on marine boundary layer NOxand SO2Distributions over the Pacific Basin, *Geophysical Research Letters*, *28*(2), 235-238, doi:10.1029/2000gl012013.

Dickerson, R. R., S. Kondragunta, G. Stenchikov, K. L. Civerolo, B. G. Doddridge, and B. N. Holben (1997), The Impact of Aerosols on Solar Ultraviolet Radiation and Photochemical Smog, *Science*, *278*(5339), 827-830, doi:10.1126/science.278.5339.827.

Ding, J., R. J. Van Der A, B. Mijling, J.-P. Jalkanen, L. Johansson, and P. F. Levelt (2018), Maritime NOx Emissions over Chinese Seas Derived from Satellite Observations, *Geophysical Research Letters*, *45*, 2031-2037, doi:10.1002/2017GL076788.

Ding, J., R. J. van der A, B. Mijling, and P. F. Levelt (2017), Space-Based NOx Emission Estimates over Remote Regions Improved in DESCO, *Atmospheric Measurement Techniques*, *10*, 925-928, doi:10.5194/amt-10-925-2017.

Duncan, B. N., et al. (2010), Application of OMI observations to a space-based indicator of NOx and VOC controls on surface ozone formation, *Atmospheric Environment*, *44*(18), 2213-2223, doi:10.1016/j.atmosenv.2010.03.010.

Eichmann, K., J. Kaiser, C. von Savigny, A. Rozanov, V. Rozanov, H. Bovensmann, M. von Konig, and J. P. Burrows (2004), SCIAMACHY Limb Measurements in the UV/Vis Spectral Region: First Results, *Advances in Space Research*, *34*(4), 775-779, doi:10.1016/j.asr.2003.05.057.

Emery, C., J. Jung, B. Koo, and G. Yarwood (2015), Improvements to CAMx Snow Cover Treatments and Carbon Bond Chemical Mechanism for Winter Ozone, *http://www.camx.com/files/udaq_snowchem_final_6aug15.pdf*.

Emery, C., B. Koo, W. C. Hsieh, A. Wentland, G. Wilson, and G. Yarwood (2016), Update Carbon Bond Chemical Mechanism, *http://www.camx.com/files/emaq4-07_task7_techmemo_r1_1aug16.pdf*.

Endlich, R. M., K. C. Nitz, R. Brodzinsky, and C. M. Bhumralkar (1984), A Long-Range Air Pollution Transport Model for Eastern North America - I. Sulfur Oxides, *Atmospheric Environment*, *18*(11), 2345-2360.

Endresen, Ø., E. Sørgård, J. K. Sundet, S. B. Dalsøren, I. S. A. Isaksen, T. F. Berglen, and G. Gravir (2003), Emission from international sea transportation and environmental impact, *Journal of Geophysical Research*, *108*(D17), doi:10.1029/2002jd002898.

EPA (1970), The Clean Air Act, in *Title 42, Chapter 85 United States Congress §7401 et seq.*, edited.

EPA (1990), Clean air act amendments of 1990, in *Public Law*, edited.

EPA (2002), Commercial Marine Emissions Inventory Development, *Final Report*, *EPA420-R-02-019*.

EPA (2008), Act to Prevent Pollution from Ships to Implement MARPOL Annex VI, in *Public Law 110-280*, edited by Congress, p. 6.

EPA (2009a), Current Methodologies in Preparing Mobile Source Port Related Emissions Inventories: Final Report, http://archive.epa.gov/sectors/web/pdf/ports-emission-inv-april09.pdf.

EPA (2009b), Regulatory impact analysis: Control of emissions of air pollution from category 3 marine diesel engines, *EPA-420-R-09-019*.

EPA (2014), Technical Support Document (TSD): Preparation of Emissions Inventories for the Version 6.0, 2011 Emissions Modeling Platform, https://www.epa.gov/sites/production/files/2015-2010/documents/2011v2016_2018base_emismod_tsd_2026feb2014.pdf.

EPA (2015a), 2011 National Emissions Inventory, Version 2 Technical Support Document, https://www.epa.gov/sites/production/files/2015-2010/documents/nei2011v2012_tsd_2014aug2015.pdf.

EPA (2015b), 2014 NEI Commercial Marine Vessels - Final, https://www.epa.gov/sites/production/files/2015-2012/documents/2014_nei_commercial_marine_vessels_reviewdraft20151217_cleaned.pdf.

EPA (2015c), National Ambient Air Quality Standards for Ozone; Final Rule, *Fed. Reg.*, *80:*, 65293-65467.

EPA (2015d), Technical Support Document (TSD): Preparation of Emissions Inventories for the Version 6.2, 2011 Emissions Modeling Platform, https://www.epa.gov/sites/production/files/2015-2010/documents/2011v2016_2012_2017_2025_emismod_tsd_aug2015.pdf.

EPA (2016a), Multi-pollutant Comparison, edited, United States Environmental Protection Agency, https://www.epa.gov/air-emissions-inventories/multi-pollutant-comparison.

EPA (2016b), NAAQS Table, *Criteria Air Pollutants*, https://www.epa.gov/criteria-air-pollutants/naaqs-table.

EPA (2016c), Technical Support Document (TSD): Preparation of Emissiosn Inventories for the Version 6.3, 2011 Emissions Modeling Platform, https://www.epa.gov/sites/production/files/2016-2009/documents/2011v2016_2013_2017_emismod_tsd_aug2016_final.pdf.

EPA (2017a), Basic Information about Air Quality SIPS, in *Air Quality Implementation Plans* edited, https://www.epa.gov/sips/basic-information-air-quality-sips.

EPA (2017b), Carbon Monoxide Emissions, *Report on the Environment*(https://cfpub.epa.gov/roe/indicator.cfm?i=10), https://cfpub.epa.gov/roe/indicator.cfm?i=10.

EPA (2017c), Clean Air Act History and Requirements, in *Clean Air Act Overview*, edited, https://www.epa.gov/clean-air-act-overview/clean-air-act-requirements-and-history.

EPA (2017d), CMAQv5.2 Operational Guidance Document, https://github.com/USEPA/CMAQ/blob/5.2.1/DOCS/User_Manual/PDF/CMAQ_OGD_Full.06302017.pdf.

EPA (2017e), Nitrogen Oxides Emissions, in *Report on the Environment*, edited, p. https://cfpub.epa.gov/roe/indicator.cfm?i=15.

EPA (2017f), Volatile Organic Compound Emissions, edited, p. https://cfpub.epa.gov/roe/indicator.cfm?i=23#23.

EPA (2018a), 8-Hour Ozone Nonattainment Areas (2015 Standard), edited.

EPA (2018b), National Air Quality Status and Trends of Key Air Pollutants, edited.

EPA (2018c), Particulate Matter (PM) Pollution, edited, pp. https://www.epa.gov/pm-pollution/particulate-matter-pm-basics#PM.

EPA (2018d), Title 40 Protection of Environment: Chapter 1: Subchapter C, in *Code of Federal Regulation*, edited, Government Publishing Office, https://www.ecfr.gov/cgi-bin/retrieveECFR?gp=&SID=c3d5704ddb77389b30450eb3baba9b92&mc=true&n=pt40.2.50&r=PART&ty=HTML.

ERG (2010), Documentation for the Commercial Marine Vessel Component of the National Emissions Inventory Methodology *Eastern Research Group* (ERG No. 0245.02.302.001; Contract No. EP-D-07-097).

Eskes, H. J., and K. F. Boersma (2003), Averaging kernels for DOAS total-column satellite retrievals, *Atmospheric Chemistry and Physics*, *3*(5), 1285-1291, doi:10.5194/acp-3-1285-2003.

Eyring, V., H. W. Kohler, J. van Aardenne, and A. Lauer (2005), Emissions from international shipping: 1. The last 50 years, *Journal of Geophysical Research-Atmospheres*, *110*(D17), doi:Artn D17305 10.1029/2004jd005619.

Fann, N., E. Coffman, B. Timin, and J. T. Kelly (2018), The estimated change in the level and distribution of PM2.5-attributable health impacts in the United States: 2005-2014, *Environ Res*, *167*, 506-514, doi:10.1016/j.envres.2018.08.018.

Fann, N., C. G. Nolte, P. Dolwick, T. L. Spero, A. C. CBrown, S. Phillips, and S. Anenberg (2015), The Geographic Distribution and Economic Value of Climate CHange-Related Ozone Health Impacts in the United States in 2030, *Journal of Air & Waste Management Association*, *65*(5), 570-580, doi:10.1080/10962247.2014.996270.

Fauroux, B., M. Sampil, P. Quenel, and Y. Lemoullec (2000), Ozone: A Trigger for Hospital Pediatric Asthma Emergency Room Visits, *Pediatric Pulmonology*, *30*, 41-46, doi:10.1002/1099-0496(200007)30:1<41::AID-PPUL7>3.0.CO;2-4.

Finlayson-Pitts, B. J., and J. N. Pitts (2000), *Chemistry of the Upper and Lower Atmosphere*, Academic Press, San Diego, CA.

Fishman, J., and P. J. Crutzen (1978), The Origin of Ozone in the Troposphere, *Nature*, *274*, 855-858.

Franke, K., A. Richter, H. Bovensmann, V. Eyring, P. Jockel, P. Hoor, and J. P. Burrows (2009), Ship emitted NO2 in the Indian Ocean: comparison of model results with satellite data, *Atmospheric Chemistry and Physics*, *9*(19), 7289-7301, doi:10.5194/acp-9-7289-2009.

Frost, G. J., et al. (2006), Effects of changing power plant NOxemissions on ozone in the eastern United States: Proof of concept, *Journal of Geophysical Research*, *111*(D12), doi:10.1029/2005jd006354.

Gantt, B., G. Sarwar, J. Xing, H. Simon, D. Schwede, W. T. Hutzell, R. Mathur, and A. Saiz-Lopez (2017), The Impact of Iodide-Mediated Ozone Deposition and Halogen Chemistry on Surface Ozone Concentrations Across the Continental United States, *Environ Sci Technol*, *51*(3), 1458-1466, doi:10.1021/acs.est.6b03556.

Gégo, E., P. S. Porter, A. Gilliland, and S. T. Rao (2007), Observation-Based Assessment of the Impact of Nitrogen Oxides Emissions Reductions on Ozone Air Quality over the Eastern United States, *Journal of Applied Meteorology and Climatology*, *46*(7), 994-1008, doi:10.1175/jam2523.1.

Goldberg, D. L., C. P. Loughner, M. Tzortziou, J. W. Stehr, K. E. Pickering, L. T. Marufu, and R. R. Dickerson (2014), Higher surface ozone concentrations over the Chesapeake Bay than over the adjacent land: Observations and models from the DISCOVER-AQ and CBODAQ campaigns, *Atmospheric Environment*, *84*, 9-19, doi:10.1016/j.atmosenv.2013.11.008.

Goldberg, D. L., et al. (2016), CAMx ozone source attribution in the eastern United States using guidance from observations during DISCOVER-AQ Maryland, *Geophysical Research Letters*, *43*(5), 2249-2258, doi:10.1002/2015gl067332.

Goldberg, D. L., T. P. Vinciguerra, K. M. Hosley, C. P. Loughner, T. P. Canty, R. J. Salawitch, and R. R. Dickerson (2015), Evidence for an increase in the ozone photochemical lifetime in the eastern United States using a regional air quality model, *Journal of Geophysical Research-Atmospheres*, *120*(24), 12778-12793, doi:10.1002/2015jd023930.

González Abad, G., X. Liu, K. Chance, H. Wang, T. P. Kurosu, and R. Suleiman (2015), Updated Smithsonian Astrophysical Observatory Ozone Monitoring Instrument (SAO OMI) formaldehyde retrieval, *Atmospheric Measurement Techniques*, *8*(1), 19-32, doi:10.5194/amt-8-19-2015.

Granier, C., et al. (2011), Evolution of anthropogenic and biomass burning emissions of air pollutants at global and regional scales during the 1980–2010 period, *Climatic Change*, *109*(1-2), 163-190, doi:10.1007/s10584-011-0154-1.

Guarnieri, M., and J. R. Balmes (2014), Outdoor Air Pollution and Asthma, *The Lancet*, *383*, 1581-1592.

Haagen-Smit, A. J., C. E. Bradley, and M. M. Fox (1953), Ozone Formation in Photochemical Oxidation of Organic Substances, *Industrial & Engineering Chemistry*, *45*(9), 2086-2089, doi:10.1021/ie50525a044.

Halpern, B. S., et al. (2008), A global map of human impact on marine ecosystems, *Science*, *319*(5865), 948-952, doi:10.1126/science.1149345.

Hastie, D. R., et al. (1999), Observational evidence for the impact of the lake breeze circulation on ozone concentrations in Southern Ontario, *Atmospheric Environment*, *33*(2), 323-335, doi:10.1016/s1352-2310(98)00199-x.

He, H., L. Hembeck, K. M. Hosley, T. P. Canty, R. J. Salawitch, and R. R. Dickerson (2013a), High ozone concentrations on hot days: The role of electric power demand and NOx emissions, *Geophysical Research Letters*, *40*(19), 5291-5294, doi:10.1002/grl.50967.

He, H., X.-Z. Liang, H. Lei, and D. J. Wuebbles (2016a), Future U.S. ozone projections dependence on regional emissions, climate change, long-range transport and differences in modeling design, *Atmospheric Environment*, *128*, 124-133, doi:10.1016/j.atmosenv.2015.12.064.

He, H., et al. (2013b), Trends in emissions and concentrations of air pollutants in the lower troposphere in the Baltimore/Washington airshed from 1997 to 2011, *Atmospheric Chemistry and Physics*, *13*(15), 7859-7874, doi:10.5194/acp-13-7859-2013.

He, H., K. Y. Vinnikov, C. Li, N. A. Krotkov, A. R. Jongeward, Z. Li, J. W. Stehr, J. C. Hains, and R. R. Dickerson (2016b), Response of SO2and particulate air pollution to local and regional emission controls: A case study in Maryland, *Earth's Future*, *4*(4), 94-109, doi:10.1002/2015ef000330.

Hildebrandt Ruiz, L., and G. Yarwood (2013), Interactions between Organic Aerosol and NOy: Influence on Oxidant Production, *http://aqrp.ceer.utexas.edu/projectinfoFY12_13%5C12-012%5C12-012%20Final%20Report.pdf*.

Hocking, M. B. (2005), *Handbook of Chemical Technology and Pollution Control*, 830 pp., Academic Press, doi:10.1016/B978-0-12-088796-5.X5000-5.

Hossaini, R., M. P. Chipperfield, A. Saiz-Lopez, R. Fernandez, S. Monks, W. Feng, P. Brauer, and R. von Glasow (2016), A global model of tropospheric chlorine chemistry: Organic versus inorganic sources and impact on methane oxidation, *Journal of Geophysical Research: Atmospheres*, *121*(23), 14,271-214,297, doi:10.1002/2016JD025756.

IMO (1948), Convention on the International Maritime Organization, edited, International Maritime Organization, http://www.imo.org/en/About/Conventions/ListOfConventions/Pages/Convention-on-the-International-Maritime-Organization.aspx.

IMO (1973), Final Act of the International Conference on Marine Pollution, edited by IMO.

IMO (1975), Ammendments to the IMCO Convention, edited.

IMO (1998), Focus on IMO: MARPOL - 25 Years.

IMO (2014), Implications of the United Nations Convention on the Law of the Sea for the International Maritime Organization, *LEG/MISC.8*.

Jacob, D. J. (1999), *Introduction to Atmospheric Chemistry*, Princeton University Press, Princeton University.

Jacob, D. J. (2000), Heterogeneous chemistry and tropospheric ozone, *Atmospheric Environment*, *34*(12-14), 2131-2159, doi:Doi 10.1016/S1352-2310(99)00462-8.

Jacobson, M. L. (2002), *Atmospheric Pollution: History, Science, and Regulation*, Cambridge University Press, Cambridge, UK.

Janjic, Z. I. (2003), A Nonhydrostatic Model Based on a New Approach, *Meteorology and Atmospheric Physics*, *82*, 271-285, doi:10.1007/s00703-001-0587-6.

Jenkin, M. E., R. G. Derwent, and T. J. Wallington (2017), Photochemical Ozone Creation Potentials for Volatile Organic Compounds: Rationalization and Estimation, *Atmospheric Environment*, *163*, 128-137.

Kamal, M. S., S. A. Razzak, and M. M. Hossain (2016), Catalytic Oxidation of Volatile Organic Compounds (VOCs) - A Review, *Atmospheric Environment*, *140*, 117-134.

Kampa, M., and E. Castanas (2007), Human Health Effects of Air Pollution, *Environmental Pollution*, *151*, 362-367.

Kansal, A. (2009), Sources and Reactivity of NMHCs and VOCs in the Atmopshere: A Review, *Journal of Hazardous Materials*, *166*, 17-26, doi:10.1016/j.jhazmat.2008.11.048.

Keene, W. C., J. Stutz, A. A. P. Pszenny, J. R. Maben, E. V. Fischer, A. M. Smith, R. von Glasow, S. Pechtl, B. C. Sive, and R. K. Varner (2007), Inorganic chlorine and bromine in coastal New England air during summer, *Journal of Geophysical Research*, *112*(D10), doi:10.1029/2006jd007689.

Kleinman, L. I. (1994), Low and High Nox Tropospheric Photochemistry, *Journal of Geophysical Research-Atmospheres*, *99*(D8), 16831-16838, doi:Doi 10.1029/94jd01028.

Kleinman, L. I. (2005), The dependence of tropospheric ozone production rate on ozone precursors, *Atmospheric Environment*, *39*(3), 575-586, doi:10.1016/j.atmosenv.2004.08.047.

Kleinman, L. I., P. H. Daum, D. G. Imre, J. H. Lee, Y. N. Lee, L. J. Nunnermacker, S. R. Springston, J. Weinstein-Lloyd, and L. Newman (2000), Ozone production in the

New York City urban plume, *Journal of Geophysical Research-Atmospheres*, *105*(D11), 14495-14511, doi:Doi 10.1029/2000jd900011.

Kleinman, L. I., P. H. Daum, Y. N. Lee, L. J. Nunnermacker, S. R. Springston, J. Weinstein-Lloyd, and J. Rudolph (2001), Sensitivity of ozone production rate to ozone precursors, *Geophysical Research Letters*, *28*(15), 2903-2906, doi:Doi 10.1029/2000gl012597.

Kleinman, L. I., P. H. Daum, Y. N. Lee, L. J. Nunnermacker, S. R. Springston, J. Weinstein-Lloyd, and J. Rudolph (2005), A comparative study of ozone production in five U.S. metropolitan areas, *110*(D2), doi:10.1029/2004jd005096.

Krotkov, N. A. (2013), OMNO2 README File, *NASA/Goddard Space Flight Center*, *Version 6.7*.

Krotkov, N. A., L. N. Lamsal, E. A. Celarier, W. H. Swartz, S. V. Marchenko, E. J. Bucsela, K. L. Chan, and M. Wenig (2017), The version 3 OMI NO2 standard product, *Atmospheric Measurement Techniques Discussions*, *2017*, 1-42, doi:10.5194/amt-2017-44.

Krotkov, N. A., and P. Veefkind (2016), OMI/Aura Nitrogen Dioxide (NO2) Total and Tropospheric Column 1-orbit L2 Swath 13x24 km V003 Greenbelt, MD, USA, *Goddard Earth Sciences Data and Information Services Center (GES DISC)*, Accessed April, 2017, doi:10.5067/Aura/OMI/DATA2017.

Lamsal, L. N., B. N. Duncan, Y. Yoshida, N. A. Krotkov, K. E. Pickering, D. G. Streets, and Z. F. Lu (2015), U.S. NO2 trends (2005-2013): EPA Air Quality System (AQS) data versus improved observations from the Ozone Monitoring Instrument (OMI), *Atmospheric Environment*, *110*, 130-143, doi:10.1016/j.atmosenv.2015.03.055.

Lamsal, L. N., R. V. Martin, A. Padmanabhan, A. van Donkelaar, Q. Zhang, C. E. Sioris, K. Chance, T. P. Kurosu, and M. J. Newchurch (2011), Application of satellite observations for timely updates to global anthropogenic NOx emission inventories, *Geophysical Research Letters*, *38*(5), n/a-n/a, doi:Artn L05810 10.1029/2010gl046476.

Lawler, M. J., R. Sander, L. J. Carpenter, J. D. Lee, R. von Glasow, R. Sommariva, and E. S. Saltzman (2011), HOCl and Cl2 observations in marine air, *Atmospheric Chemistry and Physics*, *11*(15), 7617-7628, doi:10.5194/acp-11-7617-2011.

Lawrence, M. G., and P. J. Crutzen (1999), Influence of NOx emissions from ships on tropospheric photochemistry and climate, *Nature*, *402*(6758), 167-170, doi:Doi 10.1038/46013.

Lee, P., et al. (2017), NAQFC Developmental Forecast Guidance for Fine Particulate Matter (PM2.5), *Weather and Forecasting*, *32*(1), doi:10.1175/WAF-D-15-0163.1.

Lelieveld, J., J. S. Evans, M. Fnais, D. Giannadaki, and A. Pozzer (2015), The contribution of outdoor air pollution sources to premature mortality on a global scale, *Nature*, *525*(7569), 367-371, doi:10.1038/nature15371.

Levelt, P. F., E. Hilsenrath, G. W. Leppelmeier, G. H. J. van den Oord, P. K. Bhartia, J. Tamminen, J. F. de Haan, and J. P. Veefkind (2006a), Science objectives of the Ozone Monitoring Instrument, *Ieee Transactions on Geoscience and Remote Sensing*, *44*(5), 1199-1208, doi:10.1109/Tgrs.2006.872336.

Levelt, P. F., G. H. J. van den Oord, M. R. Dobber, A. Malkki, V. Huib, V. Johan de, P. Stammes, J. O. V. Lundell, and H. Saari (2006b), The ozone monitoring instrument, *IEEE Transactions on Geoscience and Remote Sensing*, *44*(5), 1093-1101, doi:10.1109/tgrs.2006.872333.

Levy, H., 2nd (1971), Normal atmosphere: large radical and formaldehyde concentrations predicted, *Science*, *173*(3992), 141-143, doi:10.1126/science.173.3992.141.

Liao, K. J., X. T. Hou, and D. R. Baker (2014), Impacts of interstate transport of pollutants on high ozone events over the Mid-Atlantic United States, *Atmospheric Environment*, *84*, 100-112, doi:10.1016/j.atmosenv.2013.10.062.

Lippmann, M. (1989), Health Effects of Ozone: A Critical Review, *Journal of Air & Waste Management Association*, *39*(5), 672-695.

Liu, Y., M. Shao, L. Fu, S. Lu, L. Zeng, and D. Tang (2008), Source Profiles of Volatile Organic Comounds (VOCs) Measured in China: Part 1, *Atmospheric Environment*, *42*, 6247-6260.

Loughner, C. P., D. J. Allen, K. E. Pickering, D. L. Zhang, Y. X. Shou, and R. R. Dickerson (2011), Impact of fair-weather cumulus clouds and the Chesapeake Bay breeze on pollutant transport and transformation, *Atmospheric Environment*, *45*(24), 4060-4072, doi:10.1016/j.atmosenv.2011.04.003.

Loughner, C. P., et al. (2014), Impact of Bay-Breeze Circulations on Surface Air Quality and Boundary Layer Export, *Journal of Applied Meteorology and Climatology*, *53*(7), 1697-1713, doi:10.1175/Jamc-D-13-0323.1.

Madronich, S. (2014), Atmospheric chemistry: Ethanol and ozone, *Nature Geoscience*, *7*(6), 395-397, doi:10.1038/ngeo2168.

Marvin, M. R., et al. (2017), Impact of evolving isoprene mechanisms on simulated formaldehyde: An inter-comparison supported by in situ observations from SENEX, *Atmospheric Environment*, *164*, 325-336, doi:10.1016/j.atmosenv.2017.05.049.

Mazzuca, G. M., K. E. Pickering, R. D. Clark, C. P. Loughner, A. Fried, D. C. S. Zweers, A. J. Weinheimer, and R. R. Dickerson (2017), Use of tethersonde and

aircraft profiles to study the impact of mesoscale and microscale meteorology on air quality, *Atmospheric Environment*, *149*, 55-69, doi:10.1016/j.atmosenv.2016.10.025.

Mazzuca, G. M., X. R. Ren, C. P. Loughner, M. Estes, J. H. Crawford, K. E. Pickering, A. J. Weinheimer, and R. R. Dickerson (2016), Ozone production and its sensitivity to NOx and VOCs: results from the DISCOVER-AQ field experiment, Houston 2013, *Atmospheric Chemistry and Physics*, *16*(22), 14463-14474, doi:10.5194/acp-16-14463-2016.

McDill, J., S. McCusker, and E. Sabo (2015), Technical Support Document: Emission Inventory Development for 2011, 2018, and 2028 for the Northeastern US Alpha 2 Version(http://www.marama.org/images/stories/documents/2011-2018-2028_Technical_Support_Docs/TSD%20ALPHA2%20Northeast%20Emission%20Inventory%20for%202011%202018%202028%20DraftFinal%2020151123.pdf).

McDill, J., S. McCusker, and E. Sabo (2017), Technical Support Document: Emission Inventory Development for 2011 and 2017 for the Northeastern US Beta2 Version(http://www.marama.org/images/stories/documents/TSD%20BETA%20Northeast%20Emission%20Inventory%20for%202011%202017%2020170712%20FINAL.pdf).

McDonald-Buller, E., Y. Kimura, M. Craig, G. McGaughey, D. Allen, and M. Webster (2016), Dynamic Management of NOx and SO2 Emissions in the Texas and Mid-Atlantic Electric Power Systems and Implications for Air Quality, *Environ Sci Technol*, *50*(3), 1611-1619, doi:10.1021/acs.est.5b04175.

Millet, D. B., et al. (2006), Formaldehyde distribution over North America: Implications for satellite retrievals of formaldehyde columns and isoprene emission, *Journal of Geophysical Research-Atmospheres*, *111*(D24), doi:Artn D24s02 10.1029/2005jd006853.

Moghani, M., C. L. Archer, and A. Mirzakhalili (2018), The importance of transport to ozone pollution in the U.S. Mid-Atlantic, *Atmospheric Environment*, *191*, 420-431, doi:10.1016/j.atmosenv.2018.08.005.

Murphy, S. M., et al. (2009), Comprehensive Simultaneous Shipboard and Airborne Characterization of Exhaust from a Modern Container Ship at Sea, *Environmental Science & Technology*, *43*(13), 4626-4640, doi:10.1021/es802413j.

Noel, S., H. Bovensmann, M. W. Wuttke, J. P. Burrows, M. Gottwald, E. Krieg, A. P. H. Goede, and C. Muller (2002), Nadir, Limb, and Occultation Measurements with SCIAMACHY, *Advances in Space Research*, *29*(11), 1819-1824, doi:10.1016/S0273-1177(02)00102-3.

OAQPS (2007), The Plain English Guide to the Clean Air Act, *Environmental Protection Agency* (EPA-456/K-07-001), https://www.epa.gov/clean-air-act-overview/plain-english-guide-clean-air-act.

OAQPS (2015), Technical Support Document (TSD): Preparation of Emissions Inventories for the Version 6.2, 2011 Emissions Modeling Platform, *https://www.epa.gov/sites/production/files/2015-10/documents/2011v6_2_2017_2025_emismod_tsd_aug2015.pdf*.

OAQPS (2016), Technical Support Document (TSD) Preparation of Emissions Inventories for the Version 6.3, 2011 Emissions Modeling Platform, *https://www.epa.gov/sites/production/files/2016-09/documents/2011v6_3_2017_emismod_tsd_aug2016_final.pdf*.

Olivier, J., J. Peters, C. Granier, G. Petron, J. Muller, and S. Wallens (2003), Present and Future Surface Emissions of Atmospheric Compounds, POET report #2, *EU project EVK2-1999-00011*, *http://www.aero.jussieu.fr/project/ACCENT/Documents/del2_final.doc*.

Otte, T. L., and J. E. Pleim (2010), The Meteorology-Chemistry Interface Processor (MCIP) for the CMAQ modeling system: updates through MCIPv3.4.1, *Geoscientific Model Development*, *3*(1), 243-256.

Pan, L., D. Tong, P. Lee, H. Kim, and T. Chai (2014), Assessment of NOx and O3 Forecasting Performances in the U.S National Air Quality Forecasting Capability Before and After the 2012 Major Emissions Updates, *Atmospheric Environment*, *95*, 610-619, doi:10.1016/j.atmosenv.2014.06.020.

Parrish, D., D. Millet, and A. H. Goldstein (2009), Increasing Ozone in the Marine Boundary Layer Inflow at the West Coasts of North America and Europe, *Atmospheric Chemistry and Physics*, *9*, 1303-1323, doi:10.5194/acp-9-1303-2009.

Perner, D., et al. (1987), Measurements of tropospheric OH concentrations: A comparison of field data with model predictions, *5*(2), 185-216, doi:10.1007/bf00048859.

Pirjola, L., A. Pajunoja, J. Walden, J. P. Jalkanen, T. Ronkko, A. Kousa, and T. Koskentalo (2014), Mobile measurements of ship emissions in two harbour areas in Finland, *Atmospheric Measurement Techniques*, *7*(1), 149-161, doi:10.5194/amt-7-149-2014.

Pope, C. A., 3rd, R. T. Burnett, M. J. Thun, E. E. Calle, D. Krewski, K. Ito, and G. D. Thurston (2002), Lung cancer, cardiopulmonary mortality, and long-term exposure to fine particulate air pollution, *JAMA*, *287*(9), 1132-1141, doi:10.1001/jama.287.9.1132.

Pope, C. A., and D. W. Dockery (2006), Health Effects of Fine Particulate Air Pollution: Lines that Connect, *Journal of the Air & Waste Management Association*, *56*(6), 709-742, doi:10.1080/10473289.2006.10464485.

Ren, X., et al. (2018), Methane Emissions From the Baltimore-Washington Area Based on Airborne Observations: Comparison to Emissions Inventories, *Journal of Geophysical Research: Atmospheres*, *123*(16), 8869-8882, doi:doi:10.1029/2018JD028851.

Richter, A., and J. P. Burrows (2002), Tropospheric NO2 from GOME Measurements, *Advanced Space Research*, *29*(11), 1673-1683.

Richter, A., V. Eyring, J. P. Burrows, H. Bovensmann, A. Lauer, B. Sierk, and P. J. Crutzen (2004), Satellite measurements of NO2 from international shipping emissions, *Geophysical Research Letters*, *31*(23), doi:Artn L23110 10.1029/2004gl020822.

Riedel, T. P., et al. (2012), Nitryl chloride and molecular chlorine in the coastal marine boundary layer, *Environ Sci Technol*, *46*(19), 10463-10470, doi:10.1021/es204632r.

Riedel, T. P., et al. (2013), Chlorine activation within urban or power plant plumes: Vertically resolved ClNO2 and Cl2measurements from a tall tower in a polluted continental setting, *Journal of Geophysical Research: Atmospheres*, *118*(15), 8702-8715, doi:10.1002/jgrd.50637.

Riedel, T. P., et al. (2014), An MCM modeling study of nitryl chloride (ClNO2) impacts on oxidation, ozone production and nitrogen oxide partitioning in polluted continental outflow, *Atmospheric Chemistry and Physics*, *14*(8), 3789-3800, doi:10.5194/acp-14-3789-2014.

Ring, A. M., T. P. Canty, D. C. Anderson, T. P. Vinciguerra, H. He, D. L. Goldberg, S. H. Ehrman, R. R. Dickerson, and R. J. Salawitch (2018), Evaluating commercial marine emissions and their role in air quality policy using observations and the CMAQ model, *Atmospheric Environment*, *173*, 96-107, doi:10.1016/j.atmosenv.2017.10.037.

Rozanov, V., M. Buchwitz, K. Eichmann, R. de Beek, and J. P. Burrows (2002), SCIATRAN - A New Radiative Transfer Model for Geophysical Applications in the 240-2400 nm Spectral Region: The Pseudo-Spherical Version, *Advances in Space Research*, *29*(11), 1831-1835.

Ruiz, L. H., and G. Yarwood (2013), Interactions between Organic Aerosol and NOy: Influence on Oxidant Production, *Texas Air Quality Research Program Project 12-012*, *University of Texas, Austin,TX and ENVIRON International Corporation, Novato, CA*.

Ryan, W. F., B. G. Doddridge, R. R. Dickerson, R. M. Morales, K. A. Hallock, P. T. Roberts, D. L. Blumenthal, J. A. Anderson, and K. L. Civerolo (1998), Pollutant Transport During a Regional O3 Episode in the Mid-Atlantic States, *Journal of the*

Air & Waste Management Association, *48*(9), 786-797, doi:10.1080/10473289.1998.10463737.

Salawitch, R. J., et al. (2010), A new interpretation of total column BrO during Arctic spring, *Geophysical Research Letters*, *37*(21), n/a-n/a, doi:10.1029/2010gl043798.

Sarwar, G., H. Simon, P. Bhave, and G. Yarwood (2012), Examining the impact of heterogeneous nitryl chloride production on air quality across the United States, *Atmospheric Chemistry and Physics*, *12*(14), 6455-6473, doi:10.5194/acp-12-6455-2012.

Sarwar, G., H. Simon, J. Xing, and R. Mathur (2014), Importance of tropospheric ClNO2
chemistry across the Northern Hemisphere, *Geophysical Research Letters*, *41*(11), 4050-4058, doi:10.1002/2014gl059962.

Schmidt, J. A., et al. (2016), Modeling the observed tropospheric BrO background: Importance of multiphase chemistry and implications for ozone, OH, and mercury, *Journal of Geophysical Research: Atmospheres*, *121*(19), 11,819-811,835, doi:10.1002/2015jd024229.

Schnell, J. L., and M. J. Prather (2017), Co-occurrence of extremes in surface ozone, particulate matter, and temperature over eastern North America, *Proc Natl Acad Sci U S A*, *114*(11), 2854-2859, doi:10.1073/pnas.1614453114.

Schroeder, J. R., et al. (2017), New Insights into the Column CH2O/NO2 Ratio as an Indicator of Near-surface Ozone Sensitivity, *Journal of Geophysical Research: Atmospheres*, doi:10.1002/2017JD026781.

Seigel, R. B. (2014), Shallow Cumulus Mixing and Subcloud-Layer Responses to Variations in Aerosol Loading, *Journal of the Atmospheric Sciences*, *71*(7), 2581-2603, doi:10.1175/jas-d-13-0352.1.

Seinfeld, J. H., and S. N. Pandis (2006), *Atmospheric Chemistry and Physics: From Air Pollution to Climate Change*, John Wiley Press, New York.

Sherwen, T., et al. (2016), Global impacts of tropospheric halogens (Cl, Br, I) on oxidants and composition in GEOS-Chem, *Atmospheric Chemistry and Physics*, *16*(18), 12239-12271, doi:10.5194/acp-16-12239-2016.

Sillman, S. (1990), The sensitivity of ozone to nitrogen oxides and hydrocarbons in regional ozone episodes, *Journal of geophysical research.*, *95*(D2), 1837.

Sillman, S. (1999), The relation between ozone, NOx and hydrocarbons in urban and polluted rural environments, *Atmospheric Environment*, *33*(12), 1821-1845, doi:Doi 10.1016/S1352-2310(98)00345-8.

Sillman, S. (2002), Some theoretical results concerning O3-NOx-VOC chemistry and NOx-VOC indicators, *Journal of Geophysical Research*, *107*(D22), doi:10.1029/2001jd001123.

Sillman, S., et al. (2002), Loss of isoprene and sources of nighttime OH radicals at a rural site in the United States: Results from photochemical models, *Journal of Geophysical Research: Atmospheres*, *107*(D5), ACH 2-1-ACH 2-14, doi:10.1029/2001jd000449.

Sillman, S., P. J. Samson, and J. M. Masters (1993), Ozone production in urban plumes transported over water: Photochemical model and case studies in the northeastern and midwestern United States, *Journal of Geophysical Research*, *98*(D7), doi:10.1029/93jd00159.

Simon, H., Y. Kimura, G. McGaughey, D. T. Allen, S. S. Brown, H. D. Osthoff, J. M. Roberts, D. Byun, and D. Lee (2009), Modeling the impact of ClNO2 on ozone formation in the Houston area, *Journal of Geophysical Research*, *114*, doi:10.1029/2008jd010732.

Simon, H., A. Reff, B. Wells, J. Xing, and N. Frank (2015), Ozone Trends Across the United States over a Period of Decreasing NOx and VOC Emissions, *Environmental Science & Technology*, *49*, 186-195.

Skamarock, W. C., J. B. Klemp, J. Dudhia, D. O. Gill, D. M. Barker, M. G. Duda, X.-Y. Huang, W. Wang, and J. G. Powers (2008), A Description of the Advanced Research WRF Version 3, *NCAR Tech. Note NCAR/TN-475+STR*, 119, doi:10.5065/D68S4MVH.

Sorooshian, A., G. Prabhakar, H. Jonsson, R. K. Woods, R. C. Flagan, and J. H. Seinfeld (2015), On the presence of giant particles downwind of ships in the marine boundary layer, *Geophysical Research Letters*, *42*(6), 2024-2030, doi:10.1002/2015gl063179.

Spicer, C. W., E. G. Chapman, B. J. Finlayson-Pitts, R. A. Plastridge, J. M. Hubbe, J. D. Fast, and C. M. Berkowitz (1998), Unexpectedly high concentrations of molecular chlorine in coastal air, *Nature*, *394*(6691), 353-356, doi:10.1038/28584.

Stauffer, R. M., A. M. Thompson, D. K. Martins, R. D. Clark, D. L. Goldberg, C. P. Loughner, R. Delgado, R. R. Dickerson, J. W. Stehr, and M. A. Tzortziou (2015), Bay breeze influence on surface ozone at Edgewood, MD during July 2011, *J Atmos Chem*, *72*(3-4), 335-353, doi:10.1007/s10874-012-9241-6.

Stehr, J. W., R. R. Dickerson, K. A. Hallock-Waters, B. G. Doddridge, and D. Kirk (2000), Observations of NOy, CO, and SO2and the origin of reactive nitrogen in the eastern United States, *Journal of Geophysical Research: Atmospheres*, *105*(D3), 3553-3563, doi:10.1029/1999jd900998.

Stein, A. F., R. R. Draxler, G. D. Rolph, B. J. B. Stunder, M. D. Cohen, and F. Ngan (2015), NOAA's HYSPLIT Atmospheric Transport and Dispersion Modeling System, *Bulletin of the American Meteorological Society*, *96*(12), 2059-2077, doi:10.1175/bams-d-14-00110.1.

Strahan, S. E., B. N. Duncan, and P. Hoor (2007), Observationally Derived Transport Diagnostics for the Lowermost Stratosphere and their Application to the GMI Chemistry and Transport Model, *Atmospheric Chemistry and Physics*, *7*, 2435-2445.

Tanaka, P. L., S. Oldfield, J. D. Neece, C. B. Mullins, and D. T. Allen (2000), Anthropogenic Sources of Chlorine and Ozone Formation in Urban Atmospheres, *Environmental Science & Technology*, *34*(21), 4470-4473, doi:10.1021/es991380v.

Taubman, B. F., J. C. Hains, A. M. Thompson, L. T. Marufu, B. G. Doddridge, J. W. Stehr, C. A. Piety, and R. R. Dickerson (2006), Aircraft vertical profiles of trace gas and aerosol pollution over the mid-Atlantic United States: Statistics and meteorological cluster analysis, *Journal of Geophysical Research: Atmospheres*, *111*(D10), doi:10.1029/2005jd006196.

Taubman, B. F., L. T. Marufu, C. A. Piety, B. G. Doddridge, J. W. Stehr, and R. R. Dickerson (2004), Airborn Characterization of the Chemical, Optical, and Meteorological Properties and Origins of a Combined Ozone-Haze Episode over the Eastern United States, *Journal of Atmospheric Sciences*, *61*, 1781-1793.

Thompson, T. M., R. K. Saari, and N. E. Selin (2014), Air quality resolution for health impact assessment: influence of regional characteristics, *Atmospheric Chemistry and Physics*, *14*(2), 969-978, doi:10.5194/acp-14-969-2014.

Thornton, J. A., et al. (2010), A large atomic chlorine source inferred from mid-continental reactive nitrogen chemistry, *Nature*, *464*(7286), 271-274, doi:10.1038/nature08905.

Tong, D. Q., L. N. Lamsal, L. Pan, C. Ding, H. Kim, P. Lee, T. Chai, K. E. Pickering, and I. Stajner (2015), Long-Term NOx Trends Over Large Cities in the United States during the Great Recession: Comparison of Satellite Retrievals, Ground Observations, and Emissions Inventories, *Atmospheric Environment*, *107*, 70-84, doi:10.1016/j.atmosenv.2015.01.035.

Tong, D. Q., L. Pan, W. Chen, L. N. Lamsal, P. Lee, Y. Tang, H. Kim, S. Kondragunta, and I. Stajner (2016), Impact of the 2008 Gobal Recession on Air Quality Over the United States: Implications for Surface Ozone Levels from Changes in NOx Emissions, *Geophysical Research Letters*, *43*(17), 9280-9288, doi:10.1002/2016GL069885.

Trail, M., A. P. Tsimpidi, P. Liu, K. Tsigaridis, J. Rudokas, P. Miller, A. Nenes, Y. Hu, and A. G. Russell (2014), Sensitivity of air quality to potential future climate

change and emissions in the United States and major cities, *Atmospheric Environment*, *94*, 552-563, doi:10.1016/j.atmosenv.2014.05.079.

Travis, K. R., et al. (2016), Why do models overestimate surface ozone in the Southeast United States?, *Atmospheric Chemistry and Physics*, *16*(21), 13561-13577, doi:10.5194/acp-16-13561-2016.

UN (2015), Review of Maritime Transport, paper presented at United Nations Conference on Trade and Development, United Nations, New York and Geneva.

UN (2017), Factsheet: People and Oceans, paper presented at The Ocean Conference, United Nations, New York, June 5-9, 2017.

van Geffen, J. H. G. M., H. J. Eskes, K. F. Boersma, J. D. Maasakkers, and J. P. Veefkind (2018), TROPOMI ATBD of the Total and Tropospheric NO2 Data Products, *Royal Netherlands Meteorological Institute S5P-KNMI-L2-0005-RP* (1.3.0).

Veefkind, J. P., et al. (2012), TROPOMI on the ESA Sentinel-5 Precursor: A GMES mission for global observations of the atmospheric composition for climate, air quality and ozone layer applications, *Remote Sensing of Environment*, *120*, 70-83, doi:10.1016/j.rse.2011.09.027.

Vinciguerra, T., E. Bull, T. Canty, H. He, E. Zalewsky, M. Woodman, G. Aburn, S. Ehrman, and R. R. Dickerson (2017), Expected ozone benefits of reducing nitrogen oxide (NOx) emissions from coal-fired electricity generating units in the eastern United States, *J Air Waste Manag Assoc*, *67*(3), 279-291, doi:10.1080/10962247.2016.1230564.

Vinken, G. C. M. (2010), Accounting for non-linear chemistry of shipping plumes in a Global Chemistry Transport Model, *M.Sc.-Thesis*, *Eindhoven University of Technology*(R-1772-A).

Vinken, G. C. M., K. F. Boersma, D. J. Jacob, and E. W. Meijer (2011), Accounting for non-linear chemistry of ship plumes in the GEOS-Chem global chemistry transport model, *Atmospheric Chemistry and Physics*, *11*(22), 11707-11722, doi:10.5194/acp-11-11707-2011.

Vinken, G. C. M., K. F. Boersma, A. van Donkelaar, and L. Zhang (2014), Constraints on ship NOx emissions in Europe using GEOS-Chem and OMI satellite NO2 observations, *Atmospheric Chemistry and Physics*, *14*(3), 1353-1369, doi:10.5194/acp-14-1353-2014.

von Glasow, R., M. G. Lawrence, R. Sander, and P. J. Crutzen (2003), Modeling the chemical effects of ship exhaust in the cloud-free marine boundary layer, *Atmospheric Chemistry and Physics*, *3*(1), 233-250, doi:10.5194/acp-3-233-2003.

Vukovich, F. M. (1994), Boundary layer ozone variations in the eastern United States and their association with meteorological variations: Long-term variations, *Journal of Geophysical Research*, *99*(D8), doi:10.1029/93jd02554.

Walker, T. W., et al. (2010), Trans-Pacific transport of reactive nitrogen and ozone to Canada during spring, *Atmospheric Chemistry and Physics*, *10*(17), 8353-8372, doi:10.5194/acp-10-8353-2010.

Wang, C., J. J. Corbett, and J. Firestone (2008), Improving spatial representation of global ship emissions inventories, *Environ Sci Technol*, *42*(1), 193-199, doi:10.1021/es0700799.

Watts, N., et al. (2015), Health and Climate Change: Policy response to Protect Public Health, *The Lancet*, *386*, 1861-1914, doi:10.1016/S0140-6736(15)60854-6.

Wayland, R. (2014), Draft modeling guidance for demonstrating attainment of air quality goals for ozone, PM2.5, and regional haze, *http://www3.epa.gov/scram001/guidance/guide/Draft_O3-PM-RH_Modeling_Guidance-2014.pdf*.

Wells, P. G. (2017), The Iconic Torrey Canyon Oil Spill of 1967 - Marking its Legacy, *Marine Pollution Bulletin*, *115*(1-2), 1-2.

Williams, E. J., B. M. Lerner, P. C. Murphy, S. C. Herndon, and M. S. Zahniser (2009), Emissions of NOx, SO2, CO, and HCHO from commercial marine shipping during Texas Air Quality Study (TexAQS) 2006, *Journal of Geophysical Research-Atmospheres*, *114*(D21), doi:Artn D21306 10.1029/2009jd012094.

Williams, J. E., K. F. Boersma, P. Le Sager, and W. W. Verstraeten (2017), The high-resolution version of TM5-MP for optimized satellite retrievals: description and validation, *Geoscientific Model Development*, *10*(2), 721-750, doi:10.5194/gmd-10-721-2017.

Wolff, G. T., P. J. Lioy, G. D. Wight, R. E. Meyers, and R. T. Cederwall (1977), An Investigation of Long-Range Transport of Ozone Across the Midwestern and Eastern United States, *Atmospheric Environment*, *11*, 797-802.

Wong, G. T. F., and X.-H. Cheng (2008), Dissolved inorganic and organic iodine in the Chesapeake Bay and adjacent Atlantic waters: Speciation changes through an estuarine system, *Marine Chemistry*, *111*(3-4), 221-232, doi:10.1016/j.marchem.2008.05.006.

Yarwood, G., S. Rao, M. Yocke, and G. Z. Whitten (2005), Updates to the Carbon Bond Chemical Mechanism: CB05, *http://www.camx.com/publ/pdfs/CB05_Final_Report_120805.pdf*.

Yarwood, G., T. Sakulyanontvittaya, O. Nopmongcol, and B. Koo (2014), Ozone Depletion by Bromine and Iodine over the Gulf of Mexico, *https://www.tceq.texas.gov/assets/public/implementation/air/am/contracts/reports/pm/5821110365FY1412-20141109-environ-bromine.pdf*.

Yarwood, G., G. Z. Whitten, J. Jung, G. Heo, and D. Allen (2010), Development, Evaluation and Testing of Version 6 of the Carbon Bond Chemical Mechanism (CB6), *https://www.tceq.texas.gov/assets/public/implementation/air/am/contracts/reports/pm/5820784005FY1026-20100922-environ-cb6.pdf*.

Yu, S., R. Mathur, D. Kang, K. Schere, B. Eder, and J. Pleim (2006), Performance and diagnostic evaluation of ozone predictions by the Eta-Community Multiscale Air Quality Forecast System during the 2002 New England Air Quality Study, *J Air Waste Manag Assoc*, *56*(10), 1459-1471, doi:10.1080/10473289.2006.10464554.

Zaveri, R. A., C. M. Berkowitz, L. I. Kleinman, S. R. Springston, P. V. Doskey, W. A. Lonneman, and C. W. Spicer (2003), Ozone production efficiency and NOx depletion in an urban plume: Interpretation of field observations and implications for evaluating O3-NOx-VOC sensitivity, *Journal of Geophysical Research*, *108*(D14), doi:10.1029/2002jd003144.

Zhang, L., D. J. Jacob, N. V. Downey, D. A. Wood, D. Blewitt, C. C. Carouge, A. van Donkelaar, D. B. A. Jones, L. T. Murray, and Y. Wang (2011), Improved Estimate of the Policy-Relevant Background Ozone in the United States using the GEOS-Chem Global Model with 1/2 deg x 2/3 deg Horizongal Resolution over North America, *Atmospheric Environment*, *45*(37), 6769-6776, doi:10.1016/j.atmosenv.2011.07.054.

Zhao, K., Y. Bao, J. Huang, Y. Wu, F. Moshary, M. Arend, Y. Wang, and X. Lee (2019), A High-Resolution Modeling Study of a Heat Wave-Driven Ozone Exceedance Event in New York City and Surrounding Regions, *Atmospheric Environment*, *199*, 368-379, doi:10.1016/j.atmosenv.2018.10.059.